UNIVERSITÀ DEGLI STUDI DI PAVIA

FACOLTÀ DI SCIENZE MATEMATICHE, FISICHE, NATURALI
DIPARTIMENTO DI FISICA "A. VOLTA"
DOTTORATO DI RICERCA IN FISICA - XII CICLO

Quantum tomography:
methods and applications

Tutor:
Prof. Giacomo Mauro D'Ariano

Coordinator:
Prof. Sergio Ratti

Ph.D. Thesis of
Lorenzo Maccone

Thank you

My gratitude goes to everyone that helped me out in these years of scientific growth. In particular, I would like to thank my tutor Prof. G. M. D'Ariano and my research group, Chiara Macchiavello, Marco Paini, Matteo Paris, and Massimiliano Sacchi. The discussions with them, in the baffling and misleading field of Quantum Mechanics, have always been illuminating. Moreover, I have to acknowledge that the encouragements and the correctness of Prof. D'Ariano have had a big part in keeping me at the job.

Of course, I also need to thank my family and all my friends that put up with me in these years. :–)

List of publications

This thesis is based on the following list of publications.

1. G. M. D'Ariano, C. Macchiavello, L. Maccone, "Noise, errors and information in quantum amplification", Int. J. Mod. Phys. B **11**, 3385 (1997)

2. G. M. D'Ariano and L. Maccone, "Quantum Tomography of Optical Devices", in *5th International Conference on Squeezed States and Uncertainty Relations*, ed. by J. Janszky, Y. S. Kim, and V. I. Man'ko, p. 529 (1997).

3. G. M. D'Ariano, L. Maccone, "Measuring Quantum Opitcal Hamiltonians.", Phys. Rev. Lett. **80**, 5465 (1998).

4. G. M. D'Ariano and L. Maccone, "Quantum characterization of optical devices", Fortschr. Phys. **46**, 6 (1998).

5. G. M. D'Ariano, C. Macchiavello, and L. Maccone, "Quantum tomography of mesoscopic superpositions of radiation states", Phys. Rev. A **59** 1816 (1999).

6. G. M. D'Ariano, P. Kumar, C. Macchiavello, L. Maccone, and N. Sterpi, "Proposal for a Test of State Reduction and Quantum Correlations", Phys. Rev. Lett **83**, 2490 (1999).

7. G. M. D'Ariano, C. Macchiavello, and L. Maccone, "Optical quantum gates", Fortsch. der Physik (1999), in press.

8. G. M. D'Ariano, A. Garuccio, L. Maccone, and M. F. Sacchi, "Tomographic test of Bell's inequality", J. Opt. B, **1**, 576 (1999).

9. G. M. D'Ariano, L. Maccone, M. F. Sacchi and A. Garuccio: "Homodyning Bell's inequality", in '4th Int. Conf. on Quantum Communication, Measurement, and Computing, Plenum, 1998, in press.

10. G. M. D'Ariano, F. De Martini, G. Di Giuseppe, C. Macchiavello, and L. Maccone, "Quantum tomography of Fock states", unpublished.

11. G. M. D'Ariano, L. Maccone, and M. Paini, "Spin tomography", in progress.
12. G. M. D'Ariano, L. Maccone, M. G. A. Paris and M. F. Sacchi: "State preparation by photon filtering", Fortsch. der Physik, (1999), in press.
13. G. M. D'Ariano, L. Maccone, M. G. A. Paris and M. F. Sacchi, "Generation and measurement of nonclassical states by quantum Fock filter", Acta Phys. Slov. **49**, 659 (1999).
14. G. M. D'Ariano, L. Maccone, M. G. A. Paris, and M. F. Sacchi, "Optical Fock-state synthetizer" (1999), submitted to Phys. Rev. Lett.
15. G. M. D'Ariano, L. Maccone, M. G. A. Paris and M. F. Sacchi: "State measurement by photon filtering in a chain of Kerr ring cavities", 1999, submitted to Phys. Lett. A.

Contents

Introduction

The action and the properties of each physical system are determined in physics by its state. The state of the system is the mathematical description (usually a state vector or a density operator), that, when introduced in the physical formulas, allows to acquire informations on the system future and past history. The knowledge of the state is, by definition, the most complete possible knowledge that can be gained on the system, and, in general, it cannot be desumed with a single measurement operation. In classical physics it is always possible, at least in principle, to devise a procedure consisting of multiple measurements that fully recovers the physical state of each system. In Quantum Mechanics, on the contrary, there are fundamental limitations connected to the Heisenberg uncertainty principle and to the no-cloning theorem. In fact, one cannot perform an arbitrary sequence of measurements on a single system without inducing on it a back-action of some sort, while the no-cloning theorem states that one cannot create a perfect copy of a physical system without already knowing in advance its state. Thus, there is no way, not even in principle, by which a quantum state of a single system may be desumed without having some prior knowledge on it. In fact, if one wants to estimate the quantum state of a system, the only possibility is to provide a measuring procedure that employs numerous identical (although unknown) copies of the system, so that different measurements may be performed on each of the copies.

This thesis is devoted to the “quantum tomography” theory that, as many clues lead to think, may include the description of all possible quantum state estimation procedures. It has been introduced by generalizing the homodyne tomography procedure. Numerous practical applications will also be presented in the form of proposals of experiments, in which we can see the tomography method at work. The experiments are mainly in the optical domain, where radiation field modes are measured. In addition, a couple of spin state reconstruction experiments are proposed and described.

What is quantum tomography in practice? It is a state reconstruction technique that allows one to recover the state of arbitrary systems starting from a set of measurements performed on multiple copies of the system. Since, as we remarked, it is not possible to create copies of a system with unknown quantum state, we have to assume that these copies are available. This is the case, for example, of systems that are the output of a repeatable experimental procedure. On the other hand, if the single components we are analyzing through tomography are not all in the same state, then one would recover the state of the system ensemble, *i.e.* the global state of the collection of systems. In this case, the resulting ensemble state will be a so–called mixture. The state is perfectly recovered in the limit of infinite number of measurements, while in the practical finite-measurements case, one can always estimate the purely statistical error (the method is devoid of any systematic error) that is introduced in the reconstruction. Moreover, since quantum tomography provides complete information on the system, its output can be an estimation of the expectation value of any arbitrary physical quantity, in addition to the system state estimation. The abstract general tomographic procedure finds applications to various quantum systems. In particular, in this thesis we will analyze two systems, *i.e.* on one side the modes of a quantized radiation field, analyzed through homodyne and Kerr tomography, and on the other side the spin of one or more particles, analyzed through spin tomography. The homodyne is an experimental setup for measuring very weak electromagnetic fields through a laser, a beam splitter and two high efficiency photodiodes. The nonlinear Kerr effect is a property that some materials display when they are crossed by light, and which can be employed to couple two light beams.

The practical applications of tomography are numerous in the field of advanced quantum experimental research, and span from the characterization of devices to the test of state preparation techniques, to the test of fundamental aspects of Quantum Mechanics, *etc.* The theoretical quantum optics research group in Pavia, of which I am member, has a strong tradition and a high international reputation in this field, to which it has given essential contributions.

A short overview of the thesis follows. It is divided into three chapters: the first contains the theory and the methods that are necessary to implement any tomography experiment, the second contains the tomography theory for electromagnetic field and spin state reconstruction, and the third contains some proposals for optical experiments based on tomographic reconstructions.

Chapter 1. The chapter starts by giving the reader a brief historical perspective on quantum tomography. It is a very young method as the first proposals are dated 1989. Initially introduced as the extension to the quantum domain of the conventional tomographic imaging procedures, it was later greatly improved in order to remove the systematic errors intrinsic in the first method. All these first applications refer to the system of quantized radiation modes, and make use of homodyne measurements for the reconstruction procedure. Recently a major breakthrough was achieved as it was noticed that by using group theory, the homodyne tomographic formulas could be extended to arbitrary quantum systems. The outcome is the more general "quantum tomography" theory, proposed by D'Ariano, Paini and later generalized by D'Ariano. The presentation and the formalization of the quantum tomography (endeavored in this thesis for the first time) is the core of this chapter. The theory is presented as rigorous as possible for a theory that is still in a developing stage. Subsequently, the algorithmic procedures and the mathematical-statistical techniques that are necessary for any tomographic experiment are presented. The chapter is concluded by a section in which some developments of the theory are presented. It is often possible, for example, to use the noise deconvolution technique to correct the effects of experimental noise by data processing. Thus one obtains good reconstructions even when using data coming from inefficient detectors or lossy apparatuses. Another remarkable development of the theory is the adaptive tomography technique, which exploits some mathematical equivalence classes in the tomographic reconstruction formulas to reduce the statistical fluctuations of the output data and obtains better reconstructions using little input data.

Chapter 2. In this chapter three different state reconstruction methods are described, *i.e.* homodyne tomography, spin tomography and Kerr tomography. Both the homodyne tomography and the spin tomography are derived from the general theory presented in the first chapter. Homodyne tomography, which was historically the first tomographic method, is here re-derived on the basis of the general formalism. We will not go into too deep details on this method, since there is a quantity of literature on the subject. On the other hand, spin tomography, which also will be derived on the basis of the general formalism, is a very young subject and, in the form presented here (developed by D'Ariano, Maccone, Paini), has not yet been published. We will thus indeed go into details on the experimental setups needed for the tomographic reconstruction of the single spin state or of the multi-particle spin state. Moreover, some numerical simulations of simple tomographic measurements will be given, along with feasibility analyses. The Kerr tomography is another approach to the state reconstruction of radiation modes states, and was proposed by D'Ariano, Maccone, Paris, Sacchi. Its derivation from the general theory will not be given here, however the experimental setup will be described thoroughly and Monte Carlo computer simulations of its working will be presented. It proves to be particularly efficient for the measurement of the photon number distributions of radiation states, and it can also be employed for the production of optical Fock states and coherent superpositions of Fock states.

Chapter 3. In this chapter some experiments, which I contributed to propose, are presented. Each proposal is based on homodyne tomography and is supported by rigorous feasibility studies, that always include Monte Carlo numerical simulations of the experiment so that the reader can get a feeling of the actual data analysis. In fact, in the computer programs, one would only have to substitute the data simulation routines with data acquisition routines, and actual analysis of real experimental data can be performed.

The Hamiltonian operator that can be assigned to each quantum system controls its time evolution. In practical cases, it is not trivial to assign such an operator to a real physical system. We will describe a method for the experimental measurement of the Hamiltonian operator of optical devices. The measurement procedure essentially consists in feeding the device with a complete set of quantum states and determining the corresponding output states through homodyne tomography. The Hamiltonian, which is univocally determined once the input–output relations are known, is obtained in the Fock–basis representation through some non–trivial data analysis.

One of the most intriguing consequence of quantum physics is the possibility of obtaining quantum superpositions in macroscopic systems, *i.e.* the famous Schrödinger cat states. We have studied such states in the optical field and we present a modification of an experiment proposal to generate and detect optical Schrödinger cat states. In the original proposal no actual feasibility study was performed, and our simulations show that using customary non-perfect detectors (*i.e.* detectors with non-unit quantum efficiency) the original experiment would not be able to obtain quantum signatures for the measured cat, which would resemble a classical mixed state. In our proposal, by using a new deconvolution technique and the noise defeating mechanisms of tomography (*i.e.* the noise deconvolution that was described in Chap. 1), the cat is fully recovered.

Among the postulates of Quantum Mechanics, the state reduction rule is maybe the most controversial issue. Thus, an experiment that can put it to test is of fundamental importance. The possibility of introducing a number of independent different measurement schemes (*i.e.* direct detection, homodyne detection, heterodyne detection) makes the quantum optics domain perfectly suited to such a test. We present an experiment based on homodyne tomography which is here employed to measure a “reduced state” and to compare it to the theoretical one we would expect from the reduction postulate.

Another fundamental issue of Quantum Mechanics, that we propose to investigate using quantum tomography, is the problem of “locality *vs.* completeness” in quantum theory, issue raised by the EPR paradox. We suggest to test Bell’s inequality through homodyne tomography. Various experimental tests of Bell’s inequalities have up to now been performed, however the main handicap of such tests is the so called detection loophole: it has been objected that if the efficiency of the detectors is not superior to a threshold value, the experiment cannot be considered conclusive. By using the homodyne technique, one can circumvent the detector loophole, since very high efficiency detectors can be employed.

We conclude the chapter presenting a feasibility study for a homodyne experiment that is being carried out presently by De Martini's group in Roma.

Chapter 4. We give the conclusive remarks and indicate the possible developments of the presented theory and methods.

Notation: The following mathematical symbols will be used in the course of the thesis. We use $\overset{\text{def}}{=}$ and $\overset{\text{def}}{\iff}$ to define mathematical quantities and properties respectively. The complex conjugate of $\alpha \in \mathbb{C}$ will be indicated as α^*. A theorem or property demonstration is started with "Proof:" and concluded with the symbol ▾. The identity operator acting on the vector space $\mathcal{H}$ is indicated by $\mathbb{1}_{\mathcal{H}}$, where the subscript will be dropped if the context determines univocally the vector space.

Chapter 1

General tomographic method

In this chapter the general tomographic method is introduced and derived. The general mechanism can be deduced using group theory and all known tomographic schemes can be made to derive from the general formulas.

In the first section a brief history of tomography is presented. Optical homodyne tomography [1, 2], based on the seminal idea of Vogel and Risken [3] is the best known experimental procedure for the measurement of arbitrary quantum state of radiation modes. Homodyne tomography can also be used as a universal detector [4], since mean values of arbitrary electromagnetic field observables can be obtained from the homodyne data. Recently the tomographic theoretical framework has been extended and a general theory was achieved for obtaining tomographic reconstructions in arbitrary quantum systems [5, 6, 7, 8]. This theory is presented in the second section and its possible, numerous applications are sketched. Some of these applications (namely optical tomography and spin tomography) will be extensively analyzed in this thesis. In the following Sect. 1.3 some extensions of the basic tomographic method are shown. First, the deconvolution of noise inserted by the detectors and/or the experimental apparatus is analyzed. Noise can be, to a great extent, eliminated under the hypothesis that the CP-map describing its effects is invertible [2, 9]. Also, as will be analyzed in the following, the statistical random noise (resulting from the Monte Carlo average of the tomographic reconstruction with finite data) can be reduced. This is the aim of the adaptive tomography technique [10]. This technique can be pushed to a limit in which tomographic estimators, which would otherwise be non-bounded, can be brought to converge. This is obtained through the renormalized tomography procedure [8], analyzed next.

In summary, after a brief historical introduction, in this chapter the tomography technique is introduced and the group based general theory is derived. Its specification to some cases in which the theory is applied will be given in the next chapter.

1.1 Brief history of Quantum Tomography

In this section a brief historical perspective (see also [11, 12]) on quantum tomography is presented.

Already in 1957 Fano [13] stated the problem of quantum state measurement and gave an outline for the solution by demonstrating that a "complete"[1] set of observables would be necessary. Rather extensive theoretical work was later performed (see references cited in [14, 15]), but it was only with the proposal by Vogel and Risken [3] that quantum tomography was born. The first experiments, which already showed reconstructions of coherent and squeezed states were performed in Michael Raymer's group at the University of Oregon [16]. The main idea that is the basis of this and of subsequent work, is that it is possible to extend to the quantum domain the algorithms that are conventionally used in medical imaging to recover two dimensional distributions (say of mass) from unidimensional projections in different directions. However, the first tomographic method is unreliable for the measurement of unknown quantum states, since some arbitrary smoothing parameters have to be introduced. The unbiased tomographic procedure was proposed by D'Ariano, Macchiavello, Paris [1] and successively continuously improved. In fact, recently a general theoretical framework from which to derive all known tomographic formulas was proposed. Numerous experiments have been proposed using the unbiased tomographic method. Experiments (some of which are outlined in Chap. 3 for the optical domain and in Sect. 2.2 for the angular momentum domain) have also been proposed by the quantum optics research group in Pavia.

1.1.1 Conventional tomographic imaging

In conventional medical tomography, one collects data in the form of marginal distributions of the mass function $m(x, y)$. In the complex plane the marginal $r(x, \varphi)$ is a projection of a complex function ($m(x, y)$ in this case) on the direction indicated by the angle $\varphi \in [0, \pi]$. It is defined as

$$r(x, \varphi) \stackrel{\text{def}}{=} \int_{-\infty}^{+\infty} \frac{dy}{\pi} m\left((x+iy)e^{i\varphi}, (x-iy)e^{-i\varphi}\right). \tag{1.1}$$

The collection of all r for different φ is called "Radon transform". The tomography process essentially consists in the inversion of the Radon transform (1.1) in order to recover the mass function $m(x, y)$ from the marginals $r(x, \varphi)$.

A sketch of such process is now given from [11]. Start by writing $m(\alpha, \alpha^*) \equiv m(x, y)$, where $\alpha \stackrel{\text{def}}{=} (x+iy)$ and $\alpha^* \stackrel{\text{def}}{=} (x-iy)$ are considered as independent variables. Using the

---

[1] In the following we'll show that actually an irreducible set will be necessary.

complex Dirac delta function $\delta^{(2)}(\alpha) \overset{\text{def}}{=} (1/\pi^2) \int d^2\gamma \; exp[\gamma\alpha^* - \gamma^*\alpha]$ (where $d^2\gamma = dx\; dy$ for $\gamma = x + iy$) one has the obvious identity

$$m(\alpha, \alpha^*) = \int d^2\beta \; \delta^{(2)}(\alpha - \beta) \; m(\beta, \beta^*) \; . \tag{1.2}$$

By writing the delta function in complex coordinates, one has

$$\delta^{(2)}(\alpha) = \int_0^{+\infty} \frac{dk}{4} k \int_0^{2\pi} \frac{d\varphi}{\pi^2} e^{-ik\alpha_\varphi} = \int_{-\infty}^{+\infty} \frac{dk}{4} |k| \int_0^{\pi} \frac{d\varphi}{\pi^2} e^{-ik\alpha_\varphi}, \tag{1.3}$$

with $\alpha_\varphi \overset{\text{def}}{=} \mathrm{Re}(\alpha \; e^{-i\varphi}) = -\alpha_{\varphi+\pi}$, and finally, by taking $\beta = (x+iy)e^{i\varphi}$, it is immediate, from Eqs. (1.2) and (1.3), to obtain the inverse Radon transform which is the core of the whole tomographic process, *i.e.*

$$m(x, y) = \int_0^{\pi} \frac{d\varphi}{\pi} \int_{-\infty}^{+\infty} dx' \; r(x', \varphi) \int_{-\infty}^{+\infty} \frac{dk}{4} |k| \; e^{ik(x' - \alpha_\varphi)} \; . \tag{1.4}$$

Eq. (1.4) is conventionally written as

$$m(x, y) = \int_0^{\pi} \frac{d\varphi}{\pi} \int_{-\infty}^{+\infty} dx' \; r(x', \varphi) \; K(x' - \alpha_\varphi), \tag{1.5}$$

where K is the so called "Kernel function" given by

$$\begin{aligned} K(x) &\overset{\text{def}}{=} \int_{-\infty}^{+\infty} \frac{dk}{4} |k| e^{ikx} = \frac{1}{2} \mathrm{Re} \int_0^{+\infty} dk \; k e^{ikx} \\ &= \frac{1}{2} \lim_{\epsilon \to 0^+} 2\mathrm{Re} \int_0^{+\infty} dk \; k e^{ikx - k\epsilon} = -\frac{1}{2} \mathcal{P} \frac{1}{x^2}, \end{aligned} \tag{1.6}$$

where $\mathcal{P}$ indicates the Cauchy principal value. Integrating by parts Eq. (1.5) one obtains the tomographic formula that is usually found in medical imaging, *i.e.*

$$m(x, y) = \frac{1}{2\pi} \int_0^{\pi} d\varphi \;\; \mathcal{P} \int_{-\infty}^{+\infty} dx' \; \frac{1}{x' - \alpha_\varphi} \; \frac{\partial}{\partial x'} \; r(x', \varphi) \; , \tag{1.7}$$

which allows the reconstruction of the mass distribution $m(x, y)$ from its projections along different directions $r(x, \varphi)$.

1.1.2 Extension to the quantum domain

In the quantum imaging process one would like to reconstruct a quantum state (in the form of its Wigner function) starting from its marginal probability distributions. The Wigner function (introduced in the 1930s by Wigner) is a real normalized function in one to one correspondence with the state density operator ϱ. It is defined as

$$W(x, y) \overset{\text{def}}{=} \int_{-\infty}^{+\infty} \frac{dx'}{\pi} e^{-2ix'y} \langle x + x' | \varrho | x - x' \rangle \; . \tag{1.8}$$

Vogel and Risken [3] noticed that, for optical systems, the probability distributions of the quadrature operator defined as

$$x_\varphi \overset{\mathrm{def}}{=} \frac{1}{2}(a^\dagger e^{i\varphi} + a e^{-i\varphi}) \tag{1.9}$$

(a being the annihilation operator of an electromagnetic field mode) are the marginal probabilities of the Wigner function of the state of the field. Thus, by applying the same procedure outlined in the previous subsection, they managed to recover the Wigner function *via* an inverse Radon transform from the quadrature probability distributions $p(x,\varphi)$, *i.e.* Eq. (13) of [3]

$$W(x,y) = \int_0^\pi \frac{d\varphi}{\pi} \int_{-\infty}^{+\infty} dx' \, p(x',\varphi) \int_{-\infty}^{+\infty} \frac{dk}{4} \, |k| \, e^{ik(x'-x\cos\varphi - y\sin\varphi)} \; . \tag{1.10}$$

[Notice that, in the original paper [3], conventional tomographic imaging is never referred to.] The procedure to derive Eq. (1.10) with is identical to the one used in the previous subsection as one can see by comparing Eq. (1.10) with (1.4). The experimental data, namely the quadrature probability distributions, can be obtained by using the homodyne detector which, in the limit of strong local oscillator, measures the quadrature of the field [17]. For the thorough analysis of the homodyne detector (see Fig. 2.1) we address the reader to Sect. 2.1. The method proposed by Vogel and Risken, namely the inversion of the Radon transform, was the one which has been used in the first experiments [16].

Experiments have extended also beyond the optical domain and tomographic reconstruction was used *e.g.* to measure the quantum state of a vibrational mode of a molecule [18]. A modified tomographic scheme, similar to the procedure proposed by Opatrný and Welsch [19] in quantum optics (see Sect. 2.3), has been used by Leibfried *et al.* [20] to determine the vibrational state of a single atom in a Paul trap.

It should be noted, however, that this first method is unreliable for the reconstruction of unknown quantum states, since there is an intrinsic unavoidable systematic error. In fact, one can see that Eq. (1.7) contains a derivative of the quadrature probability in the direction indicated by φ and a principal–value integral. All this should be calculated with the parameter φ varying continuously in $[0,\pi]$ in order to compute the external integral in φ. In the experimental situation, where the data are just a sequence of values $\{(x_n,\varphi_n)\}$ of the quadrature in the directions $\{\varphi_n\}$, the inverse Radon transform method of Eq. (1.7) is obviously hopeless. The same holds also for Eq. (1.10), where one must keep in mind that the integral on k is unbounded. In order to use the inverse Radon transform procedure, one would need the analytical form of the marginal distribution of the quadrature $p(x,\varphi)$. This can be obtained by collecting the experimental data into histograms and splining these histograms. This is not an unbiased procedure since the degree of splining, the width of the histogram bins and the number of different phases φ_n on which the experimental data should be collected are arbitrary parameters and inject the reconstruction with systematic errors whose effects cannot be easily controlled. For example, the effect of using high degrees of splining is the wash–out of the quantum features of the state, and, *vice-versa*, the effect of low degrees of splining (or no splining at all) is to create negative bias for the probabilities in the reconstruction —see [1].

1.1.3 Quantum homodyne tomography

A new approach to optical tomography was proposed by D'Ariano, Macchiavello and Paris [1] and later generalized and simplified by D'Ariano, Leonhardt, Paul [2]. This approach, that will be referred to as 'quantum homodyne tomography', allows to recover the quantum state of the field ϱ (and also the mean values of system operators) directly from the data, abolishing all the sources of systematic errors. Only statistical errors (that can be reduced arbitrarily by collecting more experimental data) are left. The theory of homodyne tomography will be here only sketched very rapidly since its results will be derived from a much more general framework in Sect. 2.1.

By expressing position and momentum operators in terms of creation and annihilation operators as $\hat{X} \overset{\text{def}}{=} \frac{1}{2}(a + a^\dagger)$ and $\hat{P} \overset{\text{def}}{=} \frac{i}{2}(a^\dagger - a)$ and by defining the displacement operator as $\mathcal{D}(\alpha) \overset{\text{def}}{=} \exp(\alpha a^\dagger - \alpha^* a)$, it is easy to see that the Wigner function defined in (1.8) is equivalent to the complex Fourier transform of the characteristic function, *i.e.*

$$\begin{aligned} W(\alpha,\alpha^*) &= \int \frac{d^2\lambda}{\pi^2}\,\langle \mathcal{D}(\lambda)\rangle\; e^{\alpha\lambda^* - \alpha^*\lambda} \\ &\equiv \int \frac{d^2\lambda}{\pi^2}\,\mathrm{Tr}\left[\varrho\, e^{\lambda a^\dagger - \lambda^* a}\right]\; e^{\lambda^*\alpha - \lambda\alpha^*}\ , \end{aligned} \tag{1.11}$$

where $\langle \hat{O}\rangle$ denotes the expectation value of the operator $\hat{O}$. As will be shown in detail in Sect. 2.1, the same expression (1.11) can be obtained in operator form and yields

$$\varrho = \int \frac{d^2\lambda}{\pi}\,\mathrm{Tr}\left[\varrho\, e^{\lambda a^\dagger - \lambda^* a}\right]\; e^{\lambda^* a - \lambda a^\dagger}\ . \tag{1.12}$$

By writing Eq. (1.12) in polar coordinates with $\lambda \overset{\text{def}}{=} \frac{i}{2}k\, e^{i\varphi}$ one obtains

$$\begin{aligned} \varrho &= \int_0^{+\infty} \frac{dk}{4}\, k \int_0^{2\pi} \frac{d\varphi}{\pi}\,\mathrm{Tr}\left[\varrho\, e^{ikx_\varphi}\right]\; e^{-ikx_\varphi} \\ &= \int_{-\infty}^{+\infty} \frac{dk}{4}|k| \int_0^{\pi} \frac{d\varphi}{\pi}\,\mathrm{Tr}\left[\varrho\, e^{ikx_\varphi}\right]\; e^{-ikx_\varphi}\ , \end{aligned} \tag{1.13}$$

where the property $x_{\varphi+\pi} = -x_\varphi$ was used. The evaluation of the trace in (1.13) with the complete set of operators $\{|x_\varphi\rangle\}$ eigenvectors of the quadrature x_φ gives

$$\varrho = \int_0^{\pi} \frac{d\varphi}{\pi} \int_{-\infty}^{+\infty} dx\ \langle x_\varphi|\varrho|x_\varphi\rangle \int_{-\infty}^{+\infty} \frac{dk}{4}|k|\; e^{-ik(x_\varphi - x)}\ . \tag{1.14}$$

Eq. (1.14), in terms of the quadrature probability $p(x,\varphi) = \langle x_\varphi|\varrho|x_\varphi\rangle$, can be written as

$$\varrho = \int_0^\pi \frac{d\varphi}{\pi} \int_{-\infty}^{+\infty} dx\; p(x,\varphi)\; K(x - x_\varphi), \tag{1.15}$$

where $K(x_\varphi)$ is an unbounded operator, defined as in (1.6). Eq. (1.15) is the basis of the quantum homodyne tomographic procedure. In fact it is possible to use it to sample any matrix element $\langle\psi|\varrho|\phi\rangle$ such that $\langle\psi|K(x - x_\varphi)|\phi\rangle$ is bounded. Moreover, by calculating the integrals of (1.15) with the Monte Carlo method, it is possible to sample the matrix element $\langle\psi|\varrho|\phi\rangle$ directly from the homodyne experimental values. In fact, for bounded $\langle\psi|K_\eta(x - a_\varphi)|\phi\rangle$, the central limit theorem guarantees that

$$\begin{aligned}\langle\psi|\varrho|\phi\rangle &= \int_0^\pi \frac{d\varphi}{\pi} \int_{-\infty}^{+\infty} dx\; p(x,\phi)\;\; \langle\psi|K(x - x_\varphi)|\phi\rangle \\ &= \lim_{N\to\infty} \frac{1}{N} \sum_{n=0}^{N} \langle\psi|K(x_n - x_{\varphi_n}))|\phi\rangle\;,\end{aligned} \tag{1.16}$$

where x_n is the homodyne outcome measured at phase φ_n and is distributed with probability $p(x,\varphi)$. We can define "Kernel function" $K_\varphi(x)$ for the evaluation of the matrix element $\langle\psi|\varrho|\phi\rangle$ the function

$$K_\varphi[|\phi\rangle\langle\psi|](x) \overset{\text{def}}{=} \langle\psi|K(x - x_\varphi)|\phi\rangle\;. \tag{1.17}$$

Eq. (1.16) represents the actual reconstruction procedure that must be used to sample the density matrix ϱ from the homodyne data. Notice, that in order to eliminate all possible sources of systematic errors, each phase φ_n at which the measurement is to be performed must be randomly chosen with uniform probability in $[0,\pi]$. For finite number of measurements N, the estimate (1.16) of the integral is a Gaussian distributed around the true value, with statistical error decreasing as $N^{-1/2}$. For more details on the statistical procedures used in tomography, refer to Sect. 1.2.4. Notice that the measurability of the density operator matrix element depends only on the boundedness of the matrix element of the Kernel function, and that no adjustable parameters are needed in the procedure, which thus is indeed unbiased.

The tomographic formulas that were derived so far will be now generalized in order to obtain the reconstruction of the correct matrix elements starting from data collected from imperfect homodyne detectors (*i.e.* with quantum efficiency $\eta < 100\%$). From the Mandel, Kelley, and Kleiner formula describing the photon count distribution for inefficient photodetectors, one can show that a detector with quantum efficiency η is equivalent to a perfect detector (which exactly measures the number of photons and is described by the POM $\Pi = |n\rangle\langle n|$) preceded by a beam splitter with transmissivity η. As will be shown in Sect. 2.1, the effect of the efficiency in homodyne detectors is a

Gaussian convolution of the homodyne probability $p(x,\varphi)$, as

$$p_\eta(x,\varphi)=\sqrt{\frac{8\eta}{\pi(1-\eta)}}\int_{-\infty}^{+\infty}dk\; e^{-\frac{2\eta}{1-\eta}(k-x)^2}p(k,\varphi)\;. \tag{1.18}$$

The tomographic reconstruction procedure can be now derived in the same way as previously, taking care to substitute $p(x,\varphi)$ with $p_\eta(x,\varphi)$ in Eq. (1.15). In such way we obtain

$$\varrho=\int_0^\pi\frac{d\varphi}{\pi}\int_{-\infty}^{+\infty}dx\; p_\eta(x,\varphi)\;K_\eta(x-x_\varphi), \tag{1.19}$$

where now the Kernel function is defined as

$$K_\eta(x)=\frac{1}{2}\mathrm{Re}\int_0^{+\infty}k\;dk\; e^{\frac{1-\eta}{8\eta}k^2+ikx}\;. \tag{1.20}$$

In fact, by taking the Fourier transform of both members of Eq. (1.18), one can easily check that

$$\varrho=\int_0^\pi\frac{d\varphi}{\pi}\int_{-\infty}^{+\infty}dx\; p_\eta(x,\varphi)\;K_\eta(x-x_\varphi)=\int_0^\pi\frac{d\varphi}{\pi}\int_{-\infty}^{+\infty}dx\; p(x,\varphi)\;K(x-x_\varphi). \tag{1.21}$$

Notice that the anti-Gaussian in Eq. (1.20) causes a much slower convergence of the Monte Carlo integral (1.19): the statistical fluctuation will increase exponentially for decreasing detector efficiency η. In order to achieve good reconstructions with non-ideal detectors, one needs to collect a greater number of data. On the other hand, the "plain" tomographic formula (1.15) can be used also for $\eta<100\%$. In this case, the reconstructed state will be the "dressed state" we would have with ideal photodetection, preceded by a transmissivity η beam splitter, *i.e.* in general its quantum features will have been washed out to a certain extent (see *e.g.* [21]).

It is clear, from the theory we have presented, that the measurability of the density matrix depends only on the particular representation that was chosen and on the quantum efficiency of the detectors. For example, there is a bound $\eta>50\%$ for the reconstruction of the density matrix in the Fock basis: detectors with lower efficiency output data which is too spoiled to be of any use. In fact, one can see that in this case the matrix elements of the Kernel K_η in the Fock basis $\langle m|K_\eta|n\rangle$ are unbounded, and thus Eq. (1.19) is of no use. Notice that actual homodyne detectors have efficiency ranging between 70% and 90% [21, 22]. The relationship between representation and quantum efficiency will be better analyzed in Sect. 2.1.

After the method was proposed, many experiments have been performed and it is not possible to make a comprehensive list. We'll cite some: the highly squeezed state reconstruction by Breitenbach, Schiller and Mlynek [21]; the tomography schemes of Kumar [22] and his self-homodyne schemes [23]; the photon number distribution of ultrafast laser by Munroe, Boggavarapu, Anderson, and Raymer [24]; the tomographic measurement of joint photon statistics in the twin beam quantum state by Choi, D'Ariano, Kumar, and Vasilyev [25]; *etc.*

1.1.4 General tomography

Recently a general theoretical framework for state reconstruction was derived as the result of the work of D'Ariano, Maccone, Paini [5, 6, 7, 8]. It allows to recover all the formulas of homodyne tomography that were presented in the previous subsection as a special case of a much more general theory. From the general theory, new tomographical state reconstruction methods arise, such as the spin tomography (see Sect. 2.2). A new formalism has also been developed and the derivation of the tomographic formulas has been greatly simplified. Here, we will not go into any more detail on the general tomography, as it will be thoroughly analyzed in the following sections.

The quantum tomography theory that is presented in this thesis can now be considered conclusive? It is difficult to make previsions in such a delicate field as the possible extensions to a new theory, but the generality that this theory has by now reached encourages to think that a standing point has after all been achieved. This does not however mean that there is no space left for research in this field, as possible new applications of the theory can still be found, and the extension to the tomographic reconstruction of a relativistic particle is still lacking [26].

1.2 Tomography of arbitrary systems: general theory

In this section the general theory of quantum tomography [5, 6, 7, 8] will be given. We derive the formulas on which all schemes of state reconstruction that we'll present are based. The whole framework of the mathematical demonstration we will need is based on group theory formalism.

The section is divided into subsections. In the first one we will (try to) give the reader an intuitive-explanatory version of the rigorous mathematical demonstrations which are given in the following mathematical subsection. The mathematical subsection is the core of the present chapter and contains the definitions, the properties and the formulas (with their proofs) for the tomographic methods. Since in most cases (as all the ones analyzed in this thesis) one is interested in using tomography for the evaluation of ensemble values of trace–class operators, in the next subsection we derive essentially the same results but with the restriction of using trace-class operators only. The resulting theorems, though less general, are easier to derive. Historically, this was the first group tomographic method that was introduced. In the last subsection we give the basics of Monte Carlo integral theory which are needed to implement the tomographic algorithms in actual experiments (and also in numerical simulations of experiments).

1.2.1 Excursus on the method

In this subsection we'll try to get the reader familiar with the concepts that will be used more rigorously in the following. The more mathematical–oriented reader can directly skip to the following subsection. In the following we will review the general theory of [7, 8], analyzing the mathematical proofs in detail and giving some additional useful theorems.

The aim of the general tomography is to estimate, in arbitrary quantum systems, the mean value $\langle A\rangle$ of an arbitrary system operator A using only the results of the measurements on an irreducible set of observables (*i.e.* Hermitian operators) $\{Q_\lambda,\ \lambda\in\Lambda\}$, called "quorum". The procedure by which this can be obtained needs the so called "Kernel function" $K_\lambda[A](x_\lambda)$ which is a function of the quorum operators eigenvalues x_λ. The Kernel K is defined so that by integrating it with the probability $p_\lambda(x)$ of having outcome x when measuring Q_λ, it gives the mean value of A, *i.e.*

$$\langle A\rangle=\int_\Lambda d\lambda\int_{-\infty}^{+\infty}dx_\lambda\ p_\lambda(x_\lambda)\ K_\lambda[A](x_\lambda)\ , \tag{1.22}$$

where the first integral is performed on the values of λ that designate all quorum observables, and the second on all possible eigenvalues of that quorum observable Q_λ determined by the λ integration variable of the outer integral. Both (or one of the) integrals in (1.22) may actually be a sum.

The algorithmic tomographic procedure to be used in order to estimate $\langle A\rangle$ with Eq. (1.22) is the following. One chooses a quorum operator Q_λ by choosing λ with uniform probability in Λ and performs a measurement, obtaining the result x_i. By repeating the procedure N times, one collects the set of experimental data $\{(\lambda_i,x_i)$, with $i=1,\cdots,N\}$, where λ_i identifies the quorum observable used for the ith measurement, and x_i its result. From the same set of data the mean value of any operator A may be obtained. In fact one derives the Kernel function for the operator A and the quorum Q_λ, and then samples the double integral of (1.22) using the limit

$$\langle A\rangle=\lim_{N\to\infty}\frac{1}{N}\sum_{i=1}^{N}K_{\lambda_i}[A](x_i)\ . \tag{1.23}$$

Eq. (1.23) for finite N is a Monte Carlo estimate of the integrals in (1.22). As will be shown, the statistical errors of the estimate may be evaluated.

How is the Kernel function obtained, given the operator A and the quorum Q_λ? The whole framework is based on group theory theorems, such as the Schur Lemmas, and we will make extensive use of the concept of unitary irreducible representation (UIR). Thus, it is convenient to introduce the concept of tomographic group T, which essentially is a group that induces a UIR on the Hilbert space of the system $\mathcal{H}$ we are studying. We will also show that when T is a Lie group, the quorum lives in its Lie algebra. The Kernel for an arbitrary A can be obtained starting from the intertwining operator E defined through the UIR of the tomographic group T, as

$$E \stackrel{\text{def}}{=} \int_T dg\, \mathcal{R}^\dagger(g) \otimes \mathcal{R}(g)\ , \tag{1.24}$$

where the unitary operators $\mathcal{R}(g)$ form the UIR of T, and the integral is performed on all the group T elements g. We will show that for any two operators A and B, one has

$$E\, A \otimes B = B \otimes A\, E\ . \tag{1.25}$$

Using this property, one can show that

$$A = \mathrm{Tr}_1[E\, A \otimes \mathbb{1}]\ , \tag{1.26}$$

where Tr_1 indicates partial trace on the first space of $\mathcal{H} \otimes \mathcal{H}$. Eq. (1.26) should be interpreted as follows. Thanks to the intertwining operator E, A is taken from the operator space to a space where it is traced away with the UIR operators. Its place in the operator space is taken by the UIR operators that are functions of the quorum and thus may be easily calculated on the outcomes of the experiments. In fact, any element of the group UIR is a unitary operator and thus can be obtained by exponentiating a suitable hermitian operator H_g, *i.e.* $g = \exp[iH_g]$, for any g in T. If T is a Lie group, H_g is a linear combination of a basis $\vec{U} \stackrel{\text{def}}{=} \{U_k\}$ of the Lie algebra of the group, which thus contains the whole quorum: we obtained a discrete set of operators $\vec{U}$ that are a basis for the vector space of quorum observables[2]. Thus for any group element g in T, one can write

$$g = g(\psi, \vec{n}) = \exp[i\psi\vec{n} \cdot \vec{U}]\ , \tag{1.27}$$

where, since the measurement procedure for the operator O or for the same operator multiplied by a constant kO are coincident, we have taken (in the vector space of quorum observables) the polar coordinates $(\psi, \vec{n})$ by introducing the unit vector $\vec{n}$.

Using the polar parametrization of the UIR group elements, Eq. (1.26) now rewrites,

$$A = \mathrm{Tr}_1 \left[\int d\vec{n} \int d\psi\ J\ e^{-i\psi\vec{n}\cdot\vec{U}} A \otimes e^{i\psi\vec{n}\cdot\vec{U}} \right]\ , \tag{1.28}$$

where J is the Jacobian of the coordinate transformation, such that $dg = d\vec{n}\ d\psi\ J(\vec{n}, \psi)$. By taking the expectation value of both members (if the system state is described by the density matrix ϱ), Eq. (1.28) becomes

$$\langle A \rangle = \mathrm{Tr}[A\varrho] = \int d\vec{n} \int dx_{\vec{n}}\ p_{\vec{n}}(x_{\vec{n}})\ \mathrm{Tr} \left[\int d\psi J\ e^{-i\psi(\vec{n}\cdot\vec{U} - x_{\vec{n}})}\ A \right]\ , \tag{1.29}$$

---

[2] As we'll see in the next section, more generally one should also introduce an equivalence class that contains all operators acting on a Hilbert subspace of the Hilbert space, so that the tomographic reconstruction can be performed separately in each subspace.

where the trace has been evaluated on the eigenvectors $|x_{\vec{n}}\rangle$ of the quorum observable $\vec{n}\cdot\vec{U}$, and $p_{\vec{n}}(x_{\vec{n}}) \overset{\mathrm{def}}{=} \langle x_{\vec{n}}|\varrho|x_{\vec{n}}\rangle$ is the probability of obtaining the eigenvalue $x_{\vec{n}}$ when measuring $\vec{n}\cdot\vec{U}$. By comparing (1.29) and (1.22), it is immediate to obtain the following definition for the Kernel function, determined only by the quorum $Q_{\lambda(\vec{n})} = \vec{n}\cdot\vec{U}$ and by the operator A,

$$K_{\vec{n}}[A](x) \overset{\mathrm{def}}{=} \mathrm{Tr}\left[\int d\psi J\, e^{-i\psi(\vec{n}\cdot\vec{U}-x)}\, A\right] . \tag{1.30}$$

We refer the reader to the next section for the demonstration of the statements given here and for a more thorough analysis of the possible cases. Here we introduced a skeletal description of the tomography theory, and we showed how one can practically sample the mean value of any observable A starting from the outcomes of the quorum observables only.

1.2.2 Mathematical backbone

Here the rigorous mathematical demonstrations needed for the tomography theory as in [7, 8] are given through group theory [27].

We start with some definitions. Let $\mathcal{H}$ be the Hilbert space of the studied system, $\mathcal{L}(\mathcal{H})$ the set of all operators acting on $\mathcal{H}$ and ϱ the density operator of the system quantum state. Unless otherwise stated, all vectors $|\psi\rangle$ in $\mathcal{H}$ we will refer to are to be intended as normalized ($\langle\psi|\psi\rangle = 1$).

The aim of quantum tomography is to obtain the ensemble average $\langle A\rangle = \mathrm{Tr}[A\varrho]$ of some operator A acting on the Hilbert space of the system, by averaging the results of the measurements of a fixed set of observables Q_λ.

Quorum definition. *The set $\mathcal{Q} = \{Q_\lambda\}$ of observables $Q_\lambda \in \mathcal{L}(\mathcal{H})$, with $\lambda \in \Lambda$ is a quorum $\overset{\mathrm{def}}{\Longleftrightarrow}$ it is possible to determine the ensemble average $\langle A\rangle,\ \forall\ A \in \mathcal{L}(\mathcal{H})$, using outcomes of measurements of Q_λ operators only.*

Unbiased estimator definition. *The operator $\mathcal{E}_\lambda[A](Q_\lambda)$ is an unbiased estimator for the operator $A \in \mathcal{L}(\mathcal{H})$ with the quorum $\mathcal{Q} = \{Q_\lambda,\ \lambda \in \Lambda\} \overset{\mathrm{def}}{\Longleftrightarrow} \forall\varrho$ one can obtain the ensemble average of A as*

$$\langle A\rangle = \int_\Lambda d\mu(\lambda)\ \langle \mathcal{E}_\lambda[A](Q_\lambda)\rangle\ , \tag{1.31}$$

where $d\mu$ is a probability measure over the set Λ. In the case of discrete set $\Lambda = \{\lambda_1, \cdots, \lambda_N\}$, the integral will be replaced by a sum as in

$$\langle A\rangle = \sum_{i=1}^{N} \mu_i\ \langle \mathcal{E}_{\lambda_i}[A](Q_{\lambda_i})\rangle\ . \tag{1.32}$$

Notice that the two preceding definitions of quorum and unbiased estimator are not independent, since the quorum definition implies the existence of at least one unbiased estimator. Since Eqs. (1.31) and (1.32) must be true for any state ϱ, it follows necessarily that:
Any operator A in $\mathcal{L}(\mathcal{H})$ must be a function (at least in some distributional sense) of some operators contained in $\mathcal{Q}$, i.e.

$$A = \int_\Lambda d\mu(\lambda)\ \mathcal{E}_\lambda[A](Q_\lambda)\ , \tag{1.33}$$

(where the integral converges at least by taking expectation values of both members) or, for discrete quorum,

$$A = \sum_{i=1}^{N} \mu_i\ \mathcal{E}_{\lambda_i}[A](Q_{\lambda_i}) \tag{1.34}$$

(which for $N = +\infty$ converges at least by taking expectation values of both members).

Quorum irreducibility theorem. *$\{Q_\lambda\}$ is a quorum $\Rightarrow$ $\{Q_\lambda\}$ is an irreducible set of operators in $\mathcal{H}$.*
Definition: *A set $\{Q_\lambda,\ \lambda \in \Lambda\}$ is called irreducible in $\mathcal{H}$ $\overset{\text{def}}{\Longleftrightarrow}$ there are no proper invariant subspaces of $\mathcal{H}$ for the application of the set Q_λ.*

Proof: If, by *reductio ad absurdum*, it weren't so, there would be invariant subspaces in $\mathcal{H}$. One could, then, diagonalize all operators Q_λ on such subspaces, and hence all Q_λ would commute among them. Take an operator O that does not commute with any of the Q_λ, this cannot be written as a function of Q_λ ($\lambda \in \Lambda$), hence Q_λ cannot be a quorum.▼

Tomographic group definition. *The group T is a tomographic group for the Hilbert space $\mathcal{H}$ $\overset{\text{def}}{\Longleftrightarrow}$ it is a connected*[3] *Lie group with invariant*[4] *measure dg and a unitary irreducible ray representation $\mathcal{R}(g)$ of operators acting on the Hilbert space $\mathcal{H}$.*
Definition: *dg is an invariant measure for the Lie group T $\overset{\text{def}}{\Longleftrightarrow}$ dg is a volume element around g in T such that $\forall\ h, j \in T$ one has $d(h \cdot g) = d(g \cdot j) = dg$.*
Definition: *A set $\mathcal{R}(g)$ ($g \in T$) is a unitary irreducible ray representation* (UIR) *on $\mathcal{H}$ $\overset{\text{def}}{\Longleftrightarrow}$ it is a homomorphism of the group T into a set of unitary operators acting on a space $\mathcal{H}$, such that*

$$\forall\ g_1, g_2, g_3 \in T \text{ with } g_1 \cdot g_2 = g_3\ \Rightarrow\ \mathcal{R}(g_1)\mathcal{R}(g_2) = e^{i\xi(g_1,g_2)}\mathcal{R}(g_3),\ \ \xi \in \mathbb{R}, \tag{1.35}$$

---

[3] It is not necessary for the group T to be connected. If it is not, one only has to take the identity connected subgroup of the group unitary irreducible representation. Since this is a useless complication, we'll require the group to be connected.

[4] Here we are not interested in this kind of extension, but the hypothesis of invariance of the group measure can be relaxed. Some of the properties that we'll demonstrate require only left (or right) invariance.

and such that the action of the $\mathcal{R}(g)$ for $\forall\, g \in T$ on the vectors of $\mathcal{H}$ does not define invariant subspaces.

Notice that from the definition of tomographic group, it is not a restriction to consider as tomographic groups only the ones that have a faithful UIR (*i.e.* T and its UIR are isomorphic). In the following we will do so and we will use the symbol T both for the group and for its UIR group of operators $\{\mathcal{R}(g)\ g \in T\}$.

Discrete tomographic group definition. *In this thesis we will restrict our attention only to the case in which the discrete tomographic group is a subgroup of a Lie group. In this case it is still possible to use the Lie algebra of the Lie group also to generate the discrete subgroup. The extension to a generic discrete group is still lacking, but is not needed for the systems that will be analyzed in this thesis.*
For an example of applications of discrete tomographic groups refer to the discrete spin tomography, analyzed in Sect. 2.2.3.

In order to devise a tomographic scheme starting from a given quorum or in order to test if a set of observables is a quorum, we need to build an unbiased estimator for that set. Obviously, if this task is proved impossible, then the set cannot be a quorum. In order to build the unbiased estimator, we need to introduce the intertwining operator E.

Intertwining operator definition. *The intertwining operator E for a tomographic group T with* UIR $\{\mathcal{R}(g),\ g \in T\}$ *is*

$$E \overset{\text{def}}{=} \int_T dg\ \mathcal{R}^\dagger(g) \otimes \mathcal{R}(g), \tag{1.36}$$

or

$$E \overset{\text{def}}{=} \sum_{g_i} \mathcal{R}^\dagger(g_i) \otimes \mathcal{R}(g_i) \tag{1.37}$$

for discrete groups.

The reason for which E is called intertwining operator will be evident from Property 1 below. In the following, we will consider only the continuous case, since the formulas for the discrete case can be easily obtained by substituting the integral with a sum.

The operator E acts on $\mathcal{H}\otimes\mathcal{H}$ and it is self-adjoint. This last property follows from the unitarity of the representation $\mathcal{R}(g)$ and the properties[5] of the invariant measure. In fact, one has

$$\begin{aligned} E^\dagger = \int_T dg\ \mathcal{R}(g) \otimes \mathcal{R}^\dagger(g) &= \int_T dg\ \mathcal{R}^\dagger(g^{-1}) \otimes \mathcal{R}(g^{-1}) \\ &= \int_T dg'\ \mathcal{R}^\dagger(g') \otimes \mathcal{R}(g') = E\ . \end{aligned} \tag{1.38}$$

---

[5] Namely $dg = dg^{-1}$, see [28].

The tomography theorem follows from the following three properties.

Definition: A set of operators $\mathcal{R}(g)$ acting on $\mathcal{H}$ and depending on a continuous parameter g is square integrable $\overset{\text{def}}{\iff} \int dg |\langle u|\mathcal{R}(g)|v\rangle|^2 < \infty$ for $\forall\ |u\rangle,\ |v\rangle \in \mathcal{H}$.

Definition: A set of operators $\mathcal{R}(g)$ acting on $\mathcal{H}$ and depending on a discrete parameter g is square summable $\overset{\text{def}}{\iff} \sum_g^\infty |\langle u|\mathcal{R}(g)|v\rangle|^2 < \infty$ for $\forall\ |u\rangle,\ |v\rangle \in \mathcal{H}$.

Property 1. *Given two arbitrary operators $A,\ B \in \mathcal{L}(\mathcal{H})$, using E defined by Eq. (1.36) or (1.37) with square integrable (or summable) UIR $\mathcal{R}(g)$, one has*

$$\boxed{E\ A \otimes B = B \otimes A\ E\ .} \tag{1.39}$$

Proof: For an arbitrary $h \in T$ one has

$$E\ \mathbb{1} \otimes \mathcal{R}(h) = \int_T dg\ \mathcal{R}^\dagger(g) \otimes \mathcal{R}(gh) = \int_T dg'\ \mathcal{R}^\dagger(g'h^{-1}) \otimes \mathcal{R}(g') = \mathcal{R}(h) \otimes \mathbb{1}\ E, \tag{1.40}$$

where $g' \overset{\text{def}}{=} gh$ and $\mathbb{1}$ is the identity operator in $\mathcal{H}$. In (1.40) the homomorphism property [27] of group representation [*i.e.* $\mathcal{R}(g)\mathcal{R}(h) = \mathcal{R}(gh)$] and the (right) invariance of the measure have been used. Analogously, (by using the left invariance of the measure) $\forall h \in T$ one has

$$E\ \mathcal{R}(h) \otimes \mathbb{1} = \mathbb{1} \otimes \mathcal{R}(h)\ E\ . \tag{1.41}$$

In the rest of the demonstration we proceed analogously as in the demonstration of Schur's second lemma.

Consider S an intertwining operator defined by $S\ A \otimes B = B \otimes A\ S$ for $\forall A, B \in \mathcal{L}(\mathcal{H})$. From (1.40) we see that

$$ES\ \mathcal{R}(g) \otimes \mathbb{1} = E\ \mathbb{1} \otimes \mathcal{R}(g)\ S = \mathcal{R}(g) \otimes \mathbb{1}\ ES\ , \tag{1.42}$$

hence the operator ES acts as the identity on the first Hilbert space of $\mathcal{H} \otimes \mathcal{H}$. In fact, in the first Hilbert space it commutes with a UIR and Schur's second lemma may be applied, with the conclusion that ES is a multiple of the identity in the first space. Analogously from (1.41) we have

$$ES\ \mathbb{1} \otimes \mathcal{R}(g) = \mathbb{1} \otimes \mathcal{R}(g)\ ES \tag{1.43}$$

and hence ES is a multiple of the identity also on the second Hilbert space. Thus, normalizing[6] E appropriately, $ES = \mathbb{1}_\mathcal{H} \otimes \mathbb{1}_\mathcal{H} = \mathbb{1}_{\mathcal{H}\otimes\mathcal{H}}$, which implies that $E = S^{-1}$ on the whole domain $\mathcal{H} \otimes \mathcal{H}$, *i.e.* E is an intertwining operator and acts as S on the operators. ▼

---

[6] Notice that this requires the UIR which defines E through Eq. (1.36) or (1.37) to be square integrable (or summable). For non–square integrable UIR, Eq. (1.39) may still be retained, by considering it as an algebraic identity.

Property 2. *Consider a square integrable UIR $\mathcal{R}$ of the tomographic group T and impose $\int dg|\langle u|\mathcal{R}(g)|v\rangle|^2 = 1$ for some $|u\rangle,\ |v\rangle \in \mathcal{H} \Rightarrow$ one has*

$$Tr_1(E) = Tr_2(E) = \mathbb{1}\ , \tag{1.44}$$

where Tr_i indicates the partial trace over the ith space in $\mathcal{H}\otimes\mathcal{H}$, and $\mathbb{1}$ the identity on $\mathcal{H}$. Moreover, the integral $\int dg|\langle u|\mathcal{R}(g)|v\rangle|^2$ is independent on the choice of the vectors $|u\rangle$ and $|v\rangle$.

Proof: We start by showing that $\int dg|\langle u|\mathcal{R}(g)|v\rangle|^2$ is independent on $|u\rangle$ and $|v\rangle$. By using the properties of the invariant measure of T, one has

$$\begin{aligned}&\int dg\ \mathcal{R}(g)|v\rangle\langle v|\mathcal{R}^\dagger(g)\mathcal{R}(h) = \int dg'\ \mathcal{R}(hg')|v\rangle\langle v|\mathcal{R}^\dagger(g') \\ &= \mathcal{R}(h)\int dg'\ \mathcal{R}(g')|v\rangle\langle v|\mathcal{R}^\dagger(g')\ ,\end{aligned} \tag{1.45}$$

where the invariance of the group measure has been used in $dg = dg'$, with $g' = h^{-1}g$. Eq. (1.45), through Schur's second lemma, guarantees that

$$\int dg\ \mathcal{R}(g)|v\rangle\langle v|\mathcal{R}^\dagger(g) = \tau_v \mathbb{1}_{\mathcal{H}}\ ,\ \ \tau_v \in \mathbb{C}\ . \tag{1.46}$$

Hence, if one considers the quantity

$$\int dg\ |\langle u|\mathcal{R}(g)|v\rangle|^2 = \tau_v\ , \tag{1.47}$$

from Eq. (1.46) it is trivial to see that τ_v is independent on $|u\rangle$. One can check that it is also independent on $|v\rangle$ by noticing that, given an arbitrary vector $|a\rangle$

$$\begin{aligned}\tau_v &= \int dg\ \mathcal{R}(g)|v\rangle\langle v|\mathcal{R}^\dagger(g) = \langle a|\int dg\ \mathcal{R}(g)|v\rangle\langle v|\mathcal{R}^\dagger(g)|a\rangle \\ &= \int dg'\ \langle a|\mathcal{R}(g'^{-1})|v\rangle\langle v|\mathcal{R}^\dagger(g'^{-1})|a\rangle = \langle v|\int dg'\ \mathcal{R}(g')|a\rangle\langle a|\mathcal{R}^\dagger(g')|v\rangle \\ &= \tau_a\ .\end{aligned} \tag{1.48}$$

Notice that the hypothesis of square–integrability of the representation guarantees the convergence of the integral in (1.47). Thus, the natural choice for the normalization of the group's measure is to take $\tau_v = 1$.

We now prove Eq. (1.44). For any $|u\rangle$ in $\mathcal{H}$, one has, using Property 1, *i.e.* Eq. (1.39),

$$\begin{aligned}&{}_2\langle u|\mathrm{Tr}_1 E|u\rangle_2 = {}_2\langle u|\mathrm{Tr}_1 E|u\rangle_2\ {}_2\langle v|v\rangle_2 = {}_2\langle u|\mathrm{Tr}_1\Big[E\ \mathbb{1}\otimes|u\rangle_2\ {}_2\langle v|\Big]|v\rangle_2 \\ &= {}_2\langle u|\mathrm{Tr}_1\Big[|u\rangle_1\ {}_1\langle v|\otimes\mathbb{1}\ E\Big]|v\rangle_2 = \mathrm{Tr}_1|u\rangle_1\ {}_1\langle v|\int dg\ \mathcal{R}^\dagger(g)\ {}_2\langle u|\mathcal{R}(g)|v\rangle_2 \\ &= \int dg|\langle u|\mathcal{R}(g)|v\rangle|^2 = 1\ ,\end{aligned} \tag{1.49}$$

where the subscripts on the bras and kets indicate which of the spaces $\mathcal{H}\otimes\mathcal{H}$ contains the vector. The chain of equations (1.49) is true for any $|u\rangle\in\mathcal{H} \Leftrightarrow \mathrm{Tr}_1 E = \mathbb{1}_2$. The same reasoning can obviously be applied to $\mathrm{Tr}_2 E$.▾

It is now convenient to introduce the Lie algebra of the representation group $\mathcal{R}(g),\ g\in T$. Define $\vec{a}$ as the vector of coordinates for the Lie group T. Any connected Lie group T can be generated by the ("infinitesimal") elements of the 'group germ' U, *i.e.* the arbitrarily small volume element around the group identity defined as $U \overset{\mathrm{def}}{=} \{g(\vec{a})\in T \text{ such that } \forall i\ |a_i|<\epsilon,\ \epsilon>0\}$, such that if $g\in U \Rightarrow g^{-1}\in U$. The group U can be chosen such that each element of U is in a one parameter subgroup U_k, where $U_k \overset{\mathrm{def}}{=} \{g(\vec{a})\in T \text{ such that } |a_k|<\epsilon,\ a_j=0 \text{ for } k\neq j\ \epsilon>0\}$. The $\{U_k\}$ form a basis[7] for the Lie algebra of the group T. Through the exponentiation procedure, any element of the group T can be generated (in a one parameter subgroup) starting from the group germ U as $g(a_k)=e^{ia_kU_k}$, and hence, in general,

$$g(\vec{a}) = e^{i\vec{a}\cdot\vec{U}} \quad \forall g\in T\ , \tag{1.50}$$

with the obvious notation $\vec{a}\cdot\vec{U} \overset{\mathrm{def}}{=} \sum_k a_kU_k$, and where we have factorized the imaginary unit i (which will be useful in analyzing groups of unitary operators as we will require the operators U_k to be hermitian).

In general, the Lie algebra of a group of operators may be a direct sum of subalgebras, *i.e.* any vector in the Lie algebra can be decomposed into a direct sum of operators that act onto different Hilbert subspaces of the global system Hilbert space. Thus, it is useful to introduce in the Lie algebra of the group the equivalence classes defined as "*Two operators U_k, U_j are equivalent $\overset{\mathrm{def}}{\Longleftrightarrow}$ $U_k, U_j\in\mathcal{L}(\mathcal{H}_l)$, with $\mathcal{H}=\otimes_l\,\mathcal{H}_l$.*", which definitely introduces an equivalence relation[8] into the Lie algebra. Now the Lie coordinates $\vec{a}$ of the group element can be written in terms of the equivalence classes as

$$\vec{a}\cdot\vec{U} = \sum_{i=1}^{L}\vec{a}_i\cdot\vec{U}\ , \tag{1.51}$$

where the sum is actually a direct sum of operators and L is the number of equivalence classes, *i.e.* the number of subspaces in which the global Hilbert space of the system can be decomposed. For $i\neq j$, $\vec{a}_i\cdot\vec{U}$ and $\vec{a}_j\cdot\vec{U}$ act on different spaces and thus commute[9], $[\vec{a}_i\cdot\vec{U}\ ,\ \vec{a}_j\cdot\vec{U}]=0$. For example, if one considers a particle living in the xy plane with spin, the Lie algebra is generated by the basis vectors $\vec{U} \overset{\mathrm{def}}{=} \{r_x,p_x,r_y,p_y,S_x,S_y,S_z\}$ (r and p being the position and momentum operators and $\vec{S}$ being the spin operators)

---

[7] From the above reasoning, the set $\{U_k\}$ is always a discrete finite set for Lie groups.

[8] If A operates on the same space of B, then B does the same with A. If A operates on the same space as B and C, then B and C operate on the same space.

[9] Each operator is proportional to the identity on the space on which the other operator acts.

and there are 3 equivalence classes, namely those generated by $\{r_x, p_x\}$, $\{r_y, p_y\}$, and $\{S_x, S_y, S_z\}$. The usefulness of the separation of the Lie algebra into equivalent classes is evident from the fact that a measurement of a global operator of the system is carried out by taking measurements separately on each of the system components, described in different Hilbert subspaces of the system.

For our scopes, it is useful to introduce in each Lie subalgebra the *polar parametrization* of the group T, by writing $\vec{a}_i \stackrel{\text{def}}{=} \psi_i \vec{n}_i$, with $\vec{n}_i$ unit (or fixed–length) vector[10] and $\psi_i = |\vec{a}_i|$. The domain of $\vec{n}_i$ and ψ_i depends on the domain of the Lie coordinates for the subgroup[11] T_i generated by the ith equivalence class in the algebra. For the sake of clarity here we will consider $\vec{n}_i$ varying in s_i and ψ_i in Ψ_i. For example in homodyne tomography we'll see (Sect. 2.1) that it is convenient to consider $\vec{n}_i$ varying in a hemisphere of the unit sphere and $\psi_i \in (-\infty, +\infty)$, while for spin tomography (Sect. 2.2) we have $\vec{n}_i$ in the unit sphere and $\psi_i \in [0, 2\pi]$, since $T_i = SU(2)$. The usefulness of the polar parametrization arises from the fact that for any observable A and for any $k \in \mathbb{R}$, the observable kA requires the same measuring procedures as A. Naturally, in order to specify the group coordinate $\vec{a}$, one needs all the $\vec{n}_i$, ψ_i on all classes, *i.e.* $\vec{a} = (\vec{n}_1, \psi_1; \cdots; \vec{n}_L, \psi_L)$.

In summary, taken a basis $\{U_k\}$ of the Lie algebra, and dividing it into L separate equivalence classes, any element $r = \mathcal{R}(g)$ of the representation group of T can be written in function of the equivalence class coordinates as

$$r(\vec{a}) = r(\vec{n}_1, \psi_1; \cdots; \vec{n}_L, \psi_L) = \exp\left[i \sum_{i=1}^{L} \psi_i \vec{n}_i \cdot \vec{U} \right] = \prod_{i=1}^{L} \exp[i \psi_i \vec{n}_i \cdot \vec{U}] \ , \qquad (1.52)$$

where we remember that the sum is a direct sum and hence all the summed operators commute.

Property 3. *Take a basis $\vec{U} \stackrel{\text{def}}{=} \{U_k\}$ ($k = 1, \cdots, N$) of the Lie algebra of the tomographic group T representation $\{\mathcal{R}(g),\ g \in T\}$, and divide the basis operators $\vec{U}$ into L equivalence classes of operators acting on same Hilbert subspaces. $\Rightarrow$ The intertwining operator E can be written as*

$$E = \prod_{i=1}^{L} \int_{s_i} d\vec{n}_i \int_{\Psi_i} d\psi_i \ \ J_i(\vec{n}_i, \psi_i) \ e^{-i\psi_i \vec{n}_i \cdot \vec{U}} \otimes e^{i\psi_i \vec{n}_i \cdot \vec{U}} \ , \qquad (1.53)$$

where J_i is the Jacobian of the transformation $dg(\vec{a}_i) = d\psi_i \ d\vec{n}_i \ J_i(\vec{n}_i, \psi_i)$ of the Lie coordinates of each of the Lie subalgebras which are in direct sum.
Eq. (1.53) can be written equivalently, in a more compact manner, as

$$E = \prod_{i=1}^{L} \int_{s_i} d\vec{n}_i \int_{\Psi_i} d\psi_i J_i(\vec{n}_i, \psi_i) e^{-i\psi_i \vec{n}_i \cdot \Delta\vec{U}} \ , \qquad (1.54)$$

---

[10] As will be clarified later, $\vec{n}_i$ (for all i) plays the role of the λ that labels the operators in the quorum $\mathcal{Q} = \{Q_\lambda\}$.

[11] The group T_i is obviously a subgroup of the tomographic group T.

with $\Delta\vec{U} \overset{\text{def}}{=} \vec{U}\otimes\mathbb{1} - \mathbb{1}\otimes\vec{U}$.

Proof: The demonstration is easily sketched, since, using the Lie algebra elements as generators (the group is connected), one has $\mathcal{R}(g(\vec{a})) = \exp(i\vec{a}\cdot\vec{U})$, where $\vec{a} = (\vec{n}_1, \psi_1; \cdots; \vec{n}_L, \psi_L)$ is the vector of Lie coordinates of the representation group. Thus, one only has to change integration variables in the integral in the definition of E, (1.36), as

$$\int dg = \int d\vec{a} = \prod_i \int_{s_i} d\vec{n}_i \int_{\Psi_i} d\psi_i \; J_i(\vec{n}_i, \psi_i) \;.\blacktriangledown \tag{1.55}$$

It is now possible to illustrate the tomography theorem, which shows how to build the unbiased estimator, starting from the set of quorum operators Q_λ.

Tomography theorem. *Take the quorum* $\mathcal{Q} \overset{\text{def}}{=} \{Q_\lambda\}$, *an arbitrary operator* $A \in \mathcal{L}(\mathcal{H})$ *and a basis* $\{U_k\}$ *of the Lie algebra of the* UIR *of a tomographic group* T. *Define the vector of Lie coordinates as* $\vec{a}_i = \vec{a}_i(\vec{n}_i, \psi_i)$, *where* i *is the index that characterizes the subalgebras of the Lie algebra of* T. *If the* UIR *is square integrable* $\Longrightarrow$ *the unbiased estimator for* $\mathcal{Q}$ *is given by the set*

$$\boxed{\mathcal{E}_{\vec{n}_i}[A](\vec{n}_i\cdot\vec{U}) = Tr_1\Big[A\otimes\mathbb{1}\;\widetilde{E}_{\vec{n}_i}(\vec{n}_i\cdot\vec{U})\Big]\;,} \tag{1.56}$$

where the operator $\widetilde{E}$ *on* $\mathcal{H}\otimes\mathcal{H}$ *is written in terms of the* UIR *of* T *as*

$$\widetilde{E}_{\vec{n}_i}(\vec{n}_i\cdot\vec{U}) \overset{\text{def}}{=} \int_{\Psi_i} d\psi_i \; J_i(\psi_i, \vec{n}_i) \; \exp\Big[-i\psi_i\vec{n}_i\cdot(\vec{U}\otimes\mathbb{1} - \mathbb{1}\otimes\vec{U})\Big] \;, \tag{1.57}$$

where J_i *is defined by the transformation* $dg \overset{\text{def}}{=} \prod_i d\psi_i\; d\vec{n}_i\; J_i(\psi_i, \vec{n}_i)$, *which transforms the group invariant measure into the coordinates* $(\psi_i, \vec{n}_i)$. *The quorum operators* $\{Q_\lambda\}$ *live in the Lie algebra of the representation group and are defined as* $Q_\lambda \overset{\text{def}}{=} \vec{n}_i\cdot\vec{U}$ *with* $\lambda = \lambda(i; \vec{n}_i)$.
Notice that the intertwining operator E, *previously introduced, is given by*

$$E = \prod_i \int_{s_i} d\vec{n}_i \; \widetilde{E}_{\vec{n}_i}(\vec{n}_i\cdot\vec{U}) \;. \tag{1.58}$$

Proof: In order to show that (1.56) is an unbiased estimator, we must verify (1.33), namely that the operator A can be written as an integral over λ of the function $\mathcal{E}$ of the quorum observables $\{Q_\lambda\}$. Using Property 3, we see immediately that $E = \prod_i \int_{s_i} d\vec{n}_i\; \widetilde{E}_{\vec{n}_i}(\vec{n}_i\cdot\vec{U})$. Thus, one has

$$\prod_i \int_{s_i} d\vec{n}_i \; \mathcal{E}_{\vec{n}_i}[A](\vec{n}_i\cdot\vec{U}) = \prod_i \int_{s_i} d\vec{n}_i \; \mathrm{Tr}_1\Big[A\otimes\mathbb{1}\;\widetilde{E}_{\vec{n}_i}(\vec{n}_i\cdot\vec{U})\Big] = \mathrm{Tr}_1\Big[A\otimes\mathbb{1}\;E\Big]. \tag{1.59}$$

Now we use Property 1 and Property 2 respectively and obtain that

$$\mathrm{Tr}_1\Big[A\otimes \mathbb{1}\ E\Big] = \mathrm{Tr}_1\Big[E\ \mathbb{1}\otimes A\Big] = \mathrm{Tr}_1[E]A = A\ . \tag{1.60}$$

Thus we may conclude that $\mathcal{E}_{\vec{n}_i}$ is an unbiased estimator for the subgroup T_i, and that the quorum $\{Q_\lambda\}$ is the set of operators $\vec{n}_i\cdot\vec{U}$, where $\vec{n}_i$ plays the role of λ.▼

As an immediate consequence of the previous theorem, the following theorem holds.

Quorum relation with tomographic group. *Given $\{U_k\}$ a basis for the Lie algebra of T, define Q_λ as the set that contains all the hermitian operators of fixed*[12] *"length" k in the algebra, i.e. all hermitian operators of the form $\vec{n}_i\cdot\vec{U}$, with $\sum_k(\vec{n}_i)_k^2 = k^2$, for any $i \implies$ the set $\mathcal{Q}=\{Q_\lambda\}$ is a quorum for the tomographic group T.*

Proof: We have seen in the tomography theorem that an unbiased tomographic estimator exists which is function only of operators of the form $\vec{n}_i\cdot\vec{U}$. This, thanks to Eq. (1.33) ensures that the set $\vec{n}_i\cdot\vec{U}$ for $\forall\ \vec{n}_i\in s_i$ and for all i is a quorum. Moreover, since in the definition of $\vec{U}$ —see Eq. (1.50)— we have factorized the imaginary unit i and since $\vec{n}_i$ are a real vectors, we can be confident that the operators $\vec{n}_i\cdot\vec{U}$ in the Lie algebra are hermitian operators. In fact, since we are working with the group of UIR of the tomographic group T, every element

$$\mathcal{R}(g(\vec{n}_1,\psi_1;\cdots;\vec{n}_L,\psi_L)) = \prod_i \exp[i\psi_i\vec{n}_i\cdot\vec{U}] \tag{1.61}$$

of the UIR group is a unitary operator only if $\psi_i\vec{n}_i\cdot\vec{U}$ are hermitian operators.▼

In order to simplify the notation, in the following we will consider only one equivalence class in the group algebra ($L=1$). The general case follows from the fact that for Hilbert spaces of composed systems, the reconstruction can be made separately on each of the subspaces, by using the tomography theorem (1.56) on each of the equivalence classes i in the Lie algebra.

It is possible to obtain a tomographic formula of the type (1.15), by defining an appropriate Kernel. From the tomography theorem, one has

$$\begin{aligned}\langle A\rangle &= \int_s d\vec{n}\ \Big\langle \mathcal{E}_{\vec{n}}[A](\vec{n}\cdot\vec{U})\Big\rangle \qquad (1.62)\\ &= \int_s d\vec{n}\ \left\langle \mathrm{Tr}_1\left[A\otimes\mathbb{1}\int_\Psi d\psi\ J\ e^{-i\psi\vec{n}\cdot\Delta\vec{U}}\right]\right\rangle = \int_s d\vec{n}\ \mathrm{Tr}\left[A\otimes\varrho\int_\Psi d\psi\ J\ e^{-i\psi\vec{n}\cdot\Delta\vec{U}}\right]\end{aligned}$$

---

[12] In the tomography theorem, we considered vectors of unit length, but, as far as the length is fixed, any constant will do. As we have seen, this is a consequence of the fact that measuring an observable O or the same observable multiplied by a constant kO requires identical procedures.

$$= \int_s d\vec{n}$$
$$\times \mathrm{Tr}\left[\int_\Psi d\psi \; J \; \left(A \, e^{-i\psi\vec{n}\cdot\vec{U}} \otimes \mathbb{1}\right)\left(\mathbb{1} \otimes \int_{X_{\vec{n}}} dx_{\vec{n}} \int_{X_{\vec{n}}} dx'_{\vec{n}} \; \varrho_{x,x'} |x\rangle_{\vec{n}} \; {}_{\vec{n}}\langle x'| \; e^{i\psi x_{\vec{n}}}\right)\right] ,$$

where the density matrix ϱ was written in terms of the eigenfunctions of the quorum operator $\vec{n}\cdot\vec{U}$, *i.e.*

$$\varrho \overset{\text{def}}{=} \int_{X_{\vec{n}}} dx_{\vec{n}} \int_{X_{\vec{n}}} dx'_{\vec{n}} \; \varrho_{x,x'} |x\rangle_{\vec{n}} \; {}_{\vec{n}}\langle x'| \; , \tag{1.63}$$

with $(\vec{n}\cdot\vec{U})|x\rangle_{\vec{n}} = x_{\vec{n}} \, |x\rangle_{\vec{n}}$, $x_{\vec{n}} \in X_{\vec{n}}$. By separating the trace in Eq. (1.63) as $\mathrm{Tr}[O_1 \otimes O_2] = \mathrm{Tr}_1[O_1] \; \mathrm{Tr}_2[O_2]$, we find

$$\langle A\rangle = \int_s d\vec{n} \int_{X_{\vec{n}}} dx_{\vec{n}} \; p_{\vec{n}}(x_{\vec{n}}) \; \mathrm{Tr}\left[\int_\Psi d\psi \; J \; A \; e^{-i\psi(\vec{n}\cdot\vec{U} - x_{\vec{n}})}\right] \; , \tag{1.64}$$

where $p_{\vec{n}}(x_{\vec{n}}) \overset{\text{def}}{=} \varrho_{x,x}$ is the probability of obtaining $x_{\vec{n}}$ as the outcome of the measurement of the quorum observable $\vec{n}\cdot\vec{U}$.

Kernel function definition. *Define Kernel function $K_{\vec{n}}[A](x)$ for the evaluation of the observable A with the quorum $\mathcal{Q} = \{\vec{n}\cdot\vec{U}, \text{ with } |\vec{n}| = 1\}$ the function*

$$K_{\vec{n}}[A](x) \overset{\text{def}}{=} \mathrm{Tr}\left[\int_\Psi d\psi \; J(\psi,\vec{n}) \; A \; e^{-i\psi(\vec{n}\cdot\vec{U} - x)}\right] \; . \tag{1.65}$$

[Notice that, in the case of conventional homodyne tomography, this definition corresponds to the one (1.17) given previously.]

Tomographic method. *Using the tomography theorems just shown, it is possible to establish an algorithmic estimation procedure for $\langle A\rangle$. In fact, from the definition of Kernel function, one obtains*

$$\langle A\rangle = \int_s d\vec{n} \int_{X_{\vec{n}}} dx \; p_{\vec{n}}(x) \; K_{\vec{n}}[A](x) \; , \tag{1.66}$$

which allows the measurement of the mean value of operator A starting from the quorum observables $\mathcal{Q} = \{\vec{n}\cdot\vec{U} \text{ with } \vec{n} \in s\}$, with the following procedure:

- *One first chooses a quorum observable $Q_{\lambda(\vec{n})}$ in $\mathcal{Q}$ randomly with uniform*[13] *probability.*
- *One then measures the chosen $Q_{\lambda(\vec{n})} \equiv \vec{n}\cdot\vec{U}$ and evaluates the Kernel function $K_{\vec{n}}[A](x)$ on the result x of the measurement.*

---

[13] The method can be extended also to the case where each quorum observable has different probability of being chosen, as for the active adaptive tomography (see Sect. 1.3.2).

- *The procedure must be repeated averaging the results, i.e. calculating the integral (1.66) with Monte Carlo procedures. The central limit theorem (see Subsect. 1.2.4) guarantees that the result will converge to $\langle A \rangle$ for bounded $\mathcal{E}$. Moreover, since the estimator is in fact unbiased, the convergence is affected only by statistical errors that can be made arbitrarily small by increasing the data. For the evaluation of such statistical errors, and for the possible statistical checks to be performed on the data, refer to Sect. 1.2.4.*

Notice that any *operator $A \in \mathcal{L}(\mathcal{H})$ can be estimated from the same set of measurements.*

Tomography theorem for trace–class operators. *In the same hypotheses of the tomography theorem, but requiring A to be a trace–class operator, one has*

$$\boxed{\mathcal{E}_{\vec{n}}[A](\vec{n}\cdot\vec{U}) = \int_{\Psi} d\psi\ J(\psi,\vec{n})\ Tr\left[A\ e^{-i\psi\vec{n}\cdot\vec{U}}\right]\ e^{i\psi\vec{n}\cdot\vec{U}}.} \tag{1.67}$$

Proof: For the case, if A is trace–class, it is possible to exchange the integral on $d\psi$ in Eq. (1.57) with the trace of Eq. (1.56). In fact, for any unitary operator O, we have that if A is trace–class $\Rightarrow$ OA is trace–class.▼

Null estimators definition. *Notice that, even once the quorum has been fixed, the unbiased estimator for an operator A will not in general be unique, since there could exist functions (or operators) $\mathcal{N}(Q_\lambda)$ that satisfies*

$$\int d\mu(\lambda)\mathcal{N}(Q_\lambda) = 0\ , \tag{1.68}$$

that are called 'null estimators'.

From the property that defines the estimator, namely (1.31), it follows immediately that two unbiased estimators that differ by a null estimator yield the same results when estimating the operator mean value:

$$\langle A \rangle = \int_{\Lambda} d\mu(\lambda)\ \langle \mathcal{E}_\lambda[A](Q_\lambda)\rangle = \int_{\Lambda} d\mu(\lambda)\ \langle \mathcal{E}'_\lambda[A](Q_\lambda)\rangle, \tag{1.69}$$

if $\mathcal{E}'_\lambda[A](Q_\lambda) \overset{\text{def}}{=} \mathcal{E}_\lambda[A](Q_\lambda) + \mathcal{N}(Q_\lambda)$.

We will see in the following how the null estimators can be used to reduce the statistical noise. This will be the aim of adaptive tomography, which will be described in Sect. 1.3.2. Moreover, one can try to use the null functions to obtain the convergence of estimators that would otherwise be unbounded. This is the aim of the renormalized tomography, which will be described in Sect. 1.3.3.

In concluding, it should be stressed that group theory is a useful instrument for theorem demonstration, but, as many clues lead to think, it may be a too restrictive scheme on which to base the theory. In fact, consider the case of the Poincaré group [26], where the theory such as it is stated will not be applicable, and other cases, such as Weigert's state reconstruction method [29], where the representation theory will fail. In many general situations, though, group theory works and permits a fine demonstration of the needed formulas.

In this subsection the mathematical core of the generalized tomographic procedure has been derived by using group theory. The tomographic algorithm has been described for the generic estimation. From the formulas that have been shown here, all tomographic procedures analyzed in this thesis follow.

1.2.3 Tomography theory for trace–class operators

In this subsection we will re-derive the tomography theorem for trace–class operators [5, 6], *i.e.* Eq. (1.67). This was the first proposal for a group based tomographic derivation. This derivation does not give any new results and has been inserted for completeness, as it shows another possible and simpler derivation of tomographic theory independent from the one given previously.

Trace formula. *Let A be an arbitrary trace–class operator on the Hilbert space $\mathcal{H}$ of the system and $\mathcal{R}$ a unitary irreducible square integrable representation on $\mathcal{H}$ of the tomographic group T. Then*

$$\mathit{Tr}A = \int dg\ \mathcal{R}(g) A \mathcal{R}^\dagger(g), \tag{1.70}$$

where dg is an invariant measure for the group T, normalized as

$$\int dg\ |\langle u|\mathcal{R}(g)|v\rangle|^2 = 1 \tag{1.71}$$

which is independent on the choice of the vectors $|u\rangle,\ |v\rangle \in \mathcal{H}$.

Proof: The independence of the integral in (1.71) on the choice of $|u\rangle$ and $|v\rangle$ in $\mathcal{H}$ has already been shown in the demonstration of Property 2 above. Define $\tau_{u,v}$ as

$$\int dg\ \mathcal{R}(g)|u\rangle\langle v|\mathcal{R}^\dagger(g) = \tau_{u,v} \mathbb{1}_{\mathcal{H}}, \tag{1.72}$$

where the proportionality to the identity can be demonstrated through the second Schur lemma. In fact, the integral in (1.72) commutes with all the elements of a UIR, since, for any $h \in T$,

$$\int dg\ \mathcal{R}(g)|u\rangle\langle v|\mathcal{R}^\dagger(g)\mathcal{R}(h) = \int dg'\ \mathcal{R}(hg')|u\rangle\langle v|\mathcal{R}^\dagger(g') \tag{1.73}$$
$$= \mathcal{R}(h) \int dg'\ \mathcal{R}(g')|u\rangle\langle v|\mathcal{R}^\dagger(g')\ .$$

The constant $\tau_{u,v}$ can be evaluated if the vectors $|u\rangle$ and $|v\rangle$ are not orthogonal, by noticing that upon taking $h \overset{\text{def}}{=} g^{-1}$ one has for $\forall\ |a\rangle,\ |b\rangle \in \mathcal{H}$

$$\begin{aligned} 1 &= \int dg\ \langle b|\mathcal{R}(g)|a\rangle\langle a|\mathcal{R}^\dagger(g)|b\rangle = \int dg\ \frac{\langle v|\mathcal{R}(g)|a\rangle\langle a|\mathcal{R}^\dagger(g)|u\rangle}{\langle v|u\rangle} \\ &= \int dh\ \frac{\langle a|\mathcal{R}(h)|u\rangle\langle v|\mathcal{R}^\dagger(h)|a\rangle}{\langle v|u\rangle} = \frac{\tau_{u,v}}{\langle v|u\rangle}\ , \end{aligned} \tag{1.74}$$

since $dg = dh$ —see [28]. If, on the contrary, $|u\rangle$ and $|v\rangle$ are orthogonal, analogously as for Eq. (1.74), one finds

$$\tau_{u,v} = \langle a|\int dg\mathcal{R}(g)|u\rangle\langle v|\mathcal{R}^\dagger(g)|a\rangle = \int dh\langle u|\mathcal{R}(h)|a\rangle\langle a|\mathcal{R}^\dagger(h)|v\rangle = \tau_{a,a}\langle u|v\rangle = 0. \tag{1.75}$$

The trace formula is now easily found by using the Schmidt decomposition of the operator A as $A = \sum_i \alpha_i|u_i\rangle\langle v_i|$:

$$\begin{aligned} \int dg\ \mathcal{R}(g)A\mathcal{R}^\dagger(g) &= \sum_i \alpha_i \int dg\ \mathcal{R}(g)|u_i\rangle\langle v_i|\mathcal{R}^\dagger(g) = \sum_i \alpha_i\ \tau_{u_i,v_i} \\ &= \sum_i \alpha_i\langle v_i|u_i\rangle = \mathrm{Tr}A\ .\blacktriangledown \end{aligned} \tag{1.76}$$

Tomography theorem for trace–class operators. *Let A be an arbitrary trace–class operator on the Hilbert space $\mathcal{H}$ of the system and $\mathcal{R}$ an irreducible unitary square integrable representation on $\mathcal{H}$ of the tomographic group T. Then*

$$A = \int dg\ \mathrm{Tr}[A\mathcal{R}^\dagger(g)]\mathcal{R}(g)\ . \tag{1.77}$$

[Notice that this result was already obtained as (1.67) in the previous subsection.]

Proof: Let O be an invertible trace–class operator, it follows that $\mathcal{R}(g)O$ is trace–class for any $g \in T$. Hence it is possible to obtain, by applying the trace formula (1.70) twice

$$\int dg\ \mathrm{Tr}[A\mathcal{R}^\dagger(g)]O\mathcal{R}(g) = \int dg'\ \mathrm{Tr}[\mathcal{R}(g')O]\mathcal{R}^\dagger(g')A\ . \tag{1.78}$$

Take a basis $\{|k\rangle\}$ in $\mathcal{H}$, one can obtain, using again the trace formula (1.70),

$$\begin{aligned} \int dg\ \mathrm{Tr}[\mathcal{R}(g)O]\langle i|\mathcal{R}^\dagger(g)A|j\rangle &= \int dg\ \sum_k\langle k|\mathcal{R}(g)O|k\rangle\langle i|\mathcal{R}^\dagger(g)A|j\rangle \\ &= \sum_k\langle k|O\mathrm{Tr}\left[|k\rangle\langle i|\right]A|j\rangle = \langle i|OA|j\rangle\ . \end{aligned} \tag{1.79}$$

From Eqs. (1.78) and (1.79) it follows immediately that

$$\int dg\ \mathrm{Tr}[A\mathcal{R}^\dagger(g)]O\mathcal{R}(g) = OA\ , \tag{1.80}$$

which yields the thesis (1.77) by multiplying to the left both members by O^{-1}.▾

It is trivial to extend theorem (1.77) to the case of projective representations, *i.e.* group representations for which, given g_1, g_2, $g_3 \in T$ such that $g_1 \cdot g_2 = g_3$, one has

$$\mathcal{R}(g_1)\mathcal{R}(g_2) = e^{i\zeta(g_1,g_2)}\mathcal{R}(g_3)\ , \tag{1.81}$$

$\zeta \in \mathbb{R}$ being a phase factor depending on g_1 and g_2.

Analogously as in the previous section, we can use Eq. (1.77) to obtain an algorithmic estimation procedure. In fact, consider the usual parametrization of the UIR group $\mathcal{R}(g) = e^{i\psi\vec{n}\cdot\vec{U}}$ with $\vec{U}$ basis vector of the Lie algebra of T and $\vec{n}$ and ψ varying in s and Ψ respectively. Take the expectation values of both members of (1.77) and calculate the trace on the quantum state ϱ of the system using the eigenvectors of the observables $\vec{n}\cdot\vec{U}$. By introducing the Jacobian J for the coordinate transformation $dg = d\vec{n}\ d\psi\ J(\vec{n},\psi)$ and the probability $p_{\vec{n}}(x)$ of obtaining the result x for the measurement of $\vec{n}\cdot\vec{U}$, you would obtain

$$\begin{aligned}\langle A\rangle &= \int dg\ \langle \mathrm{Tr}[A\mathcal{R}^\dagger(g)]\mathcal{R}(g)\rangle = \int_s d\vec{n}\int_\Psi d\psi\ J(\vec{n},\psi)\ \mathrm{Tr}[A\ e^{-i\psi\vec{n}\cdot\vec{U}}]\ \mathrm{Tr}[\varrho\ e^{i\psi\vec{n}\cdot\vec{U}}]\\ &= \int_s d\vec{n}\int_\Psi d\psi\ J(\vec{n},\psi)\int_{X_{\vec{n}}} dx\ p_{\vec{n}}(x)\ \mathrm{Tr}[A\ e^{-i\psi(\vec{n}\cdot\vec{U}-x)}]\ ,\end{aligned} \tag{1.82}$$

which yields Eq. (1.66) by defining the "Kernel function for the trace–class operator" A as

$$K_{\vec{n}}[A](x) \overset{\mathrm{def}}{=} \int_\Psi d\psi\ J(\vec{n},\psi)\ \mathrm{Tr}[A\ e^{-i\psi(\vec{n}\cdot\vec{U}-x)}]\ . \tag{1.83}$$

Thus the same algorithmic tomographic method described in page 31 applies here.

From result (1.77), with an appropriate choice for the tomographic group and the irreducible representation, it is possible to prove the formula for spin tomography (2.22) –derived in Sect. 2.2– and for optical homodyne tomography (1.15) –see Sect. 2.1. Notice that the unimodularity hypothesis given in the definition of tomographic group T can be relaxed without losing most of the results we gave in this section.

In conclusion, in this section we re-derived the formulas and the procedures we showed in the previous one, here for the case of trace–class operators. Though less general, the formulas we have obtained here are much easier to derive.

1.2.4 Monte Carlo methods for tomography

In this subsection we will very briefly review the basics of the Monte Carlo integration techniques that are needed for the tomographic algorithmic implementation. We explain how it is possible to evaluate the statistical error bars of the tomographically estimated quantities. Finally, we give tests for checking the experimental or simulated data statistics (such as the χ^2 test). In the course of this thesis various other Monte Carlo techniques have been exploited for simulating the experiments (such as quantum jump, cumulative distribution technique or metropolis algorithms). These will be analyzed along with the simulations, while here we give only the techniques which are basic for *any* tomographic experiment (real or simulated).

The tomographic method for the evaluation of arbitrary expectation values (see Sect. 1.2.2), is based on the integral (1.66) on the experimental data. It is of the form

$$F = \int_{-\infty}^{+\infty} dx\, p(x)\, f(x) \ , \tag{1.84}$$

where $p(x)$ is a probability, *i.e.* $p(x) \geqslant 0 \ \forall x$ and $\int dx\ p(x) = 1$. Since we have experimental outcomes $\{x_n, \ n = 1, \cdots N\}$ distributed according to the probability $p(x)$, we would like to sample the integral (1.84) using the limit

$$\int_{-\infty}^{+\infty} dx\, p(x)\, f(x) = \lim_{N\to\infty} \frac{1}{N} \sum_{n=1}^{N} f(x_n) \ . \tag{1.85}$$

Obviously in any practical case it is not possible to estimate the limit (1.85), but one has to approximate the integral with a finite sum of N elements

$$F_N = \frac{1}{N} \sum_{n=1}^{N} f(x_n) \ . \tag{1.86}$$

To estimate the error one makes in the approximation, and to see if and how this error decreases increasing the number N of data, one needs the central limit theorem [30].

Central limit theorem. *Consider N statistically uncorrelated random variables $\{z_n, n = 1, \cdots, N\}$, with mean values $\mu(z_n)$, variances $\sigma^2(z_n)$ and bounded third order moments. If the variances $\sigma^2(z_n)$ are all of the same order $\Longrightarrow$ the statistical variable "sum" y, defined as*

$$y \overset{\text{def}}{=} \sum_{n=1}^{N} z_n \ , \quad \textit{has mean} \ \ \mu(y) = \sum_{n=1}^{N} \mu(z_n) \ \ \textit{and variance} \ \ \sigma^2(y) = \sum_{n=1}^{N} \sigma^2(z_n) \ . \tag{1.87}$$

The distribution of y approaches asymptotically a Gaussian for $N \to \infty$.

In practical cases, the distribution of y can be considered Gaussian already for as low as $N \sim 10$. For our needs the hypotheses are met if the kernel function $f(x)$ has limited moments up to the third moment, since all the x_n come from the same probability density $p(x)$, and hence all the $z_n \overset{\text{def}}{=} \frac{1}{N} f(x_n)$ have all the same variances (and means).

Using the central limit theorem, we can conclude that $y = F_N$ is a statistical variable distributed as a Gaussian (for $N \gtrsim 10$) with mean value

$$\mu_y = \sum_{n=1}^{N} \frac{F}{N} = F \tag{1.88}$$

and variance

$$\sigma^2(y) = \frac{1}{N^2} \sum_{n=1}^{N} \lim_{M\to\infty} \frac{1}{M} \sum_{j=1}^{M} [f(x_j)]^2 - F^2 = \frac{\sigma^2(F)}{N} \ , \tag{1.89}$$

since we have $\mu(z_n) = \frac{1}{N} \lim_M \sum_{j=1}^{M} \frac{f(x_j)}{M} = \frac{F}{N}$ and $\sigma^2(z_n) = \frac{1}{N^2} \lim_M \frac{1}{M} \sum_{j=1}^{M} [f(x_j)]^2 - F^2 = \frac{\sigma^2(F)}{N^2}$ for any n. We see also the tomographic estimated quantities converge with statistical errors that decrease as $\propto \frac{1}{\sqrt{N}}$.

Since the statistical variable F_N converges to F and is distributed as a Gaussian (at least for $N \gtrsim 10$) we can also evaluate the statistical error bars associated with the tomographic reconstruction. In fact divide the experimental (or simulated) data $\{x_n\}$ into N statistical blocks of equal dimension M. Then evaluate the tomographic integrals of the form (1.84) on each block, using the finite estimation formula (1.86). The set F_n $(n = 1, \cdots, N)$, which we showed Gaussian distributed, is obtained. It is possible to estimate the Gaussian mean value and variance, as

$$m(F_n) = \frac{1}{N} \sum_{n=1}^{N} F_n \tag{1.90}$$

and

$$s^2(F_n) = \frac{1}{N-1} \sum_{n=1}^{N} (F_n - m)^2 \ . \tag{1.91}$$

[Remember that the factor $N-1$ in the variance denominator arises from the fact that we are using the "experimental" estimated mean value m in place of the "real" one μ.] Eq. (1.91) gives the estimation of the variance of the data. The variance of the statistical variable 'mean m' is given by [30]

$$\sigma^2(m) \equiv \sigma^2 \left(\frac{1}{N} \sum_{n=1}^{N} F_N \right) = \frac{1}{N^2} \sum_{n=1}^{N} \sigma^2(F_N) = \frac{1}{N} \sigma^2(F_N) \ , \tag{1.92}$$

and thus the 'error bar' on the mean m estimated from the data is given by

$$\epsilon = \frac{1}{\sqrt{N}} \, s(F_N) = \sqrt{\sum_{n=1}^{N} \frac{(F_n - m)^2}{N(N-1)}} \tag{1.93}$$

From the Gaussian integral one recovers the usual statistical interpretation to the obtained results: the "real" value F is to be found in the interval $[m - \epsilon, m + \epsilon]$ with

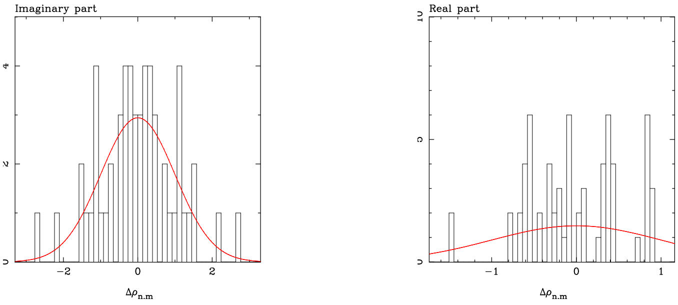

Figure 1.1: Example of the statistical checks that can be performed for checking the tomographic reconstruction. Left: the data estimated on the blocks is distributed as a Gaussian. This assures that no systematic errors are present in the experimental (here simulated) data. Right: a “bad” check. There is evidently some error in the statistics. These are checks taken from actual data analysis batches for the simulation of the reconstruction of the Schrödinger cat density matrix as described in Sect. 3.3. The data, in particular, refers to the evaluation of the (imaginary part of) matrix elements in the Fock basis.

$\sim$ 68% probability, in the interval $[m-2\epsilon, m+2\epsilon]$ with $\sim$ 95% probability and in $[m-3\epsilon, m+3\epsilon]$ with $\sim$ unit probability.

In order to test that the confidence intervals are estimated correctly and that errors in the data analysis or systematic errors in the experimental data do not undermine the final data, one may check the F_n distribution, to see if it actually is a Gaussian distribution. This may be done by simply plotting a histogram of the block final data and comparing it “by eye” to a Gaussian, as exemplified in Fig. 1.1, or by using the χ^2 test, which proceeds as follows. Starting from the histogram of the F_n distribution, consider the quantity

$$\chi^2 \overset{\text{def}}{=} \sum_{n=1}^{N} \frac{(p_n-\mu_n)^2}{\mu_n} \;, \tag{1.94}$$

where N is the number of bins in the histogram, p_n is the number of data in the nth histogram bin, and μ_n is the number of points we would find in the same bin if we considered a Gaussian of mean m and variance Δs^2. It can be shown [30] that the statistical variable χ^2 defined in (1.94) is actually distributed as a χ^2 distribution with $\nu = N-1$ degrees of freedom, *i.e.* as the distribution

$$D(x,\nu) \overset{\text{def}}{=} \frac{1}{2^{\nu/2}\Gamma(\nu/2)} x^{\frac{\nu-2}{2}} e^{-\frac{x^2}{2}} \;. \tag{1.95}$$

Thus, the confidence level of the estimated Gaussian, *i.e.* the probability that we have estimated through m and Δs^2 the correct Gaussian from the obtained data, is

$$P = \int_{\chi^2}^{+\infty} dx\ D(x, N-1)\ . \tag{1.96}$$

If we obtain a low confidence level P, then the error bars are not correctly estimated, as the data is not Gaussian.

Notice that the procedure for the estimation of the error bars described here must be modified when we have very low statistics. This may happen when the block mean values converge too slowly. This, for example is the case of the tomographic test of Bell's inequalities, which is described in Sect. 3.5. In such cases it is not possible to divide the whole set of data in N equal sized sets, where we remind that N must at least be of the order of 10. In such cases one must consider only one block, on which the mean value m is calculated. Then, one builds a histogram of the experimental data x_j and estimates the statistical distribution of these values. Using a computer simulation, one must extract another N data sets of variables x_j from the estimated distribution and use these sets to calculate the $F_n,\ n = 1, \cdots, N$. These F_n are to be used through (1.91) *only* to estimate the statistical error bar, and *not* for the tomographic reconstruction of m, which would otherwise be biased. This is the method commonly used by particle physicists [31], which often deal with low statistics events.

In this subsection we have assumed that the tomographic integral takes the form (1.84). Actually, the tomographic evaluation integral (1.66) is a double integral, on the variables $\vec{n}$ and $x_{\vec{n}}$. This poses no problem, since one can show that a relation of the type (1.84) holds also for double integrals, namely

$$\int_{-\infty}^{+\infty} dx \int_{-\infty}^{+\infty} dy\ p(x,y)\ F(x,y) = \lim_{N\to\infty} \frac{1}{N} \sum_{n=1}^{N} F(x_n, y_n)\ , \tag{1.97}$$

with the couples $\{(x_n, y_n)\}$ distributed with probability $p(x,y)$.

In this subsection the practical methods for obtaining the tomographic estimates and the associated error bars has been illustrated, and the necessary Monte Carlo techniques have been introduced.

1.3 Further developments of the theory

Here the general tomographic theory that was studied in the previous sections is developed in detail. In particular here we will analyze: 1) the noise deconvolution scheme [7, 8], which allows to eliminate (at the data analysis stage) the experimental noise that arises from imperfect detection, lossy devices, *etc.*; 2) the adaptive tomography technique [10], which allows to tune the unbiased tomographic estimators to the experimental data one obtains, in order to reduce the statistical noise; and 3) the renormalized tomography technique [7], which seeks the removal of divergencies in tomographic reconstructions by using the Null estimators.

1.3.1 Noise deconvolution

In this subsection we see under which conditions and for which detection schemes it is possible to devise noise eliminating mechanisms at the tomographic data analysis stage for state reconstruction. Essentially it is possible to eliminate detection noise when it is possible to invert the noise CP-map.

We start by introducing a definition of the noise process. These can always be described by a unit preserving CP-map, an application $\Gamma : \mathcal{L}(\mathcal{H}) \rightarrow \mathcal{L}(\mathcal{H})$, that maps system operators into system operators. The noise can actually be deconvolved at the data analysis if

- the inverse of Γ exists, namely $\Gamma^{-1} : \mathcal{L}(\mathcal{H}) \rightarrow \mathcal{L}(\mathcal{H})$, with $\Gamma^{-1}\left[\Gamma\left[A\right]\right] = A$, for $\forall A \in \mathcal{L}(\mathcal{H})$.
- the estimator $\mathcal{E}_\lambda[A](Q_\lambda)$ is in the domain of Γ^{-1}
- the map $\Gamma^{-1}\left[\mathcal{E}_\lambda[A](Q_\lambda)\right]$ is a function of Q_λ.

This is the case, for example, of the noise arising from the limited quantum efficiency η of the homodyne detectors [9]. If the above conditions are met, we can recover the "ideal" expectation value $\langle A\rangle$ that we would get without noise. This is achieved by using, in place of the estimator (1.56) obtained from the tomography theorem, the following 'deconvolved estimator',

$$\Gamma^{-1}\left[\mathcal{E}_{\vec{n}}[A](\vec{n}\cdot\vec{U})\right] = \mathrm{Tr}_1\left[A\otimes \mathbb{1}\,\Gamma^{-1}\left[\widetilde{E}_{\vec{n}}(\vec{n}\cdot\vec{U})\right]\right] \quad . \tag{1.98}$$

As an example for the noise deconvolution described here, in Sect. 2.1.3 we will analyze the case of homodyne tomography, where the limited quantum efficiency $\eta <$ 100% of homodyne detectors has the effect of a Gaussian convolution of the quadrature probabilities and its effects can be beaten with the technique described here.

1.3.2 Adaptive tomography

In this section we will analyze the adaptive tomography technique [10]. The essential idea is that the tomographic Null estimators (NE), introduced in Sect. 1.2.2, may be used to reduce the statistical noise arising from the fact that in an actual experiment (or numerically simulated experiment) the experimental data is always finite.

The addition of a NE in the ideal case of infinite statistics does not change the measured quantities, as shown in Eq. (1.69), since the NE mean value is zero. In the realistic case of finite statistics, the mean values that are output by the tomographic process are statistical variables. As shown in Sect. 1.2.4, by taking partial tomographic averages of the data by dividing it into statistical blocks, one finds that the obtained mean values are gaussian distributed (provided, as should always be, that the Kernel function K satisfies the hypotheses of the central limit theorem). Thus, one may look for a procedure capable of reducing the variance of the tomographically estimated mean values. In fact, consider the class of equivalent estimators (estimators differing only by NEs), *i.e.*

$$\mathcal{E}'_\lambda[A](Q_\lambda) \stackrel{\text{def}}{=} \mathcal{E}_\lambda[A](Q_\lambda) + \sum_{i=1}^{M} \nu_i \mathcal{N}_i(Q_\lambda) \, , \tag{1.99}$$

where $\mathcal{E}_\lambda[A](Q_\lambda)$ is the tomographic estimator for the operator A whose mean value we are measuring. Each estimator in the class $\mathcal{E}'$ will be identified by the coefficient vector $\vec{\nu}$. The variance of the tomographic quantities can be estimated as (dropping the dependence on λ and Q_λ)

$$\overline{\Delta^2 \mathcal{E}'[A]} = \overline{\Delta^2 \mathcal{E}[A]} + 2 \sum_{i=1}^{M} \nu_i \overline{\mathcal{N}_i \mathcal{E}[A]} \; + \sum_{i,j=1}^{M} \nu_i \nu_j \overline{\mathcal{N}_i \mathcal{N}_j} \, , \tag{1.100}$$

where $\overline{F(Q_\lambda)} \stackrel{\text{def}}{=} \langle \int d\mu(\lambda) \; F(Q_\lambda) \rangle$, and obviously

$$\overline{\Delta^2 \mathcal{E}[A]} \stackrel{\text{def}}{=} \left\langle \int d\mu(\lambda) \mathcal{E}^2_\lambda[A](Q_\lambda) - \left(\int d\mu(\lambda') \mathcal{E}_{\lambda'}[A](Q_{\lambda'}) \right)^2 \right\rangle \, . \tag{1.101}$$

In Eq. (1.100), we used the defining property of the NE, namely

$$\left\langle \int d\mu(\lambda) \mathcal{E}_\lambda[A](Q_\lambda) \right\rangle = \left\langle \int d\mu(\lambda) \mathcal{E}_\lambda[A](Q_\lambda) + \sum_{i=1}^{M} \nu_i \mathcal{N}_i(Q_\lambda) \right\rangle \quad \text{for any } \vec{\nu} \, . \tag{1.102}$$

Now the estimated "modified variance" $\overline{\Delta^2 \mathcal{E}'[A]}$ are minimized with respect to the coefficients ν_i, and we obtain

$$\sum_{j=1}^{M} \nu_j \overline{\mathcal{N}_i \mathcal{N}_j} = -\overline{\mathcal{E}[A] \mathcal{N}_i} \, , \tag{1.103}$$

which can be solved starting from the tomographically estimated mean values, with the vector $\vec{\nu}$ as unknown. Notice that the obtained vector $\vec{\nu}$ will depend on the experimental data, and has to be calculated with the above procedure for any new set of data.

Actually the adaptive tomographic algorithm consists in the following steps:

- Find all the null estimators $\mathcal{N}_i(Q_\lambda)$ $(i = 1, \cdots, M)$ for the quorum $\mathcal{Q}$ which is being used in the experiment.

- Execute (or numerically simulate) the experiment and collect the input data.

- Calculate, using the obtained data, the mean values $\overline{\mathcal{N}_i \mathcal{N}_j}$ and $\overline{\mathcal{E}[A] \mathcal{N}_i}$, and solve the linear system (1.103), to obtain $\vec{\nu}$.

- Use the vector $\vec{\nu}$ obtained in the previous step to build the 'optimized estimator' $\mathcal{E}'[A] = \mathcal{E}[A] + \sum_i \nu_i \mathcal{N}_i$. The mean values one want to measure must now be evaluated (using the data collected in the first step) with the usual tomographic formula, but employing 'optimized estimator', *i.e.*

$$\langle A \rangle = \int_\Lambda d\mu(\lambda)\ \langle {\mathcal{E}'}_\lambda[A](Q_\lambda) \rangle\ , \tag{1.104}$$

- For each new set of data the whole procedure must be repeated, as $\vec{\nu}$ is dependent on the data.

Notice that also the mean values are changed in the adaptive tomographic process: remember that null estimators do not change mean values only in the limiting case of infinite statistics. In fact the estimated mean values are changed in such a way as to reduce the dispersion of the estimated data. Refer to [10] for striking examples of simulations of such a procedure, which does efficiently reduce statistical noise of tomographic reconstructions.

The procedure described in this subsection may be labeled 'passive' adaptive tomography, as it only deals with the data analysis stage. A further evolution of the scheme is the so called 'active adaptive tomography' where also the observables in the quorum on which the experimental data is obtained are tuned according to the partial set of data already collected with a sort of feed-forward mechanism. We will not go into any more detail on this new technique, since it is currently still under development.

A new iterative adaptive tomography technique is now proposed. In fact, for trace-class operators one can use Eq. (1.67) for $\langle A \rangle$ estimation, and thus (introducing the null estimators) it is possible to obtain

$$\begin{aligned}\langle A \rangle &= \int_s d\vec{n} \int_\Psi d\psi J \int dx\ \mathrm{Tr}[A\ e^{-i\psi\vec{n}\cdot\vec{U}}]\mathrm{Tr}[\varrho\ e^{i\psi\vec{n}\cdot\vec{U}}] + \mathrm{Tr}[\varrho\,\mathcal{N}(\vec{n}\cdot\vec{U})] \\ &= \int_s d\vec{n} \int_\Psi d\psi J \int dx\ \mathrm{Tr}\left[A\ e^{-i\psi\vec{n}\cdot\vec{U}} + \frac{\varrho\mathcal{N}(\vec{n}\cdot\vec{U})}{\mathrm{Tr}[\varrho e^{i\psi\vec{n}\cdot\vec{U}}]}\right] \mathrm{Tr}\left[\varrho\ e^{i\psi\vec{n}\cdot\vec{U}}\right]\ .\end{aligned} \tag{1.105}$$

One can see that in Eq. (1.105) the Kernel depends not only on the operator A to estimate and on the null operators $\mathcal{N}$, but also on the state ϱ itself. One should then use Eq. (1.105) to improve iteratively the tomographically estimated ϱ.

1.3.3 Renormalized tomography

This technique [7, 32] seeks the removal of divergencies that affect some tomographic reconstructions, as for example the homodyne tomography with low efficiency photodetection ($\eta < 50\%$). The main idea, which basically still has not found any practical application, is to use the Null estimators $\mathcal{N}(Q_\lambda)$ introduced in Sect. 1.2.2 to force the convergence of otherwise unbounded Kernel functions.

In fact, from Sect. 1.2.4, we know that one can be confident when estimating an expectation value $\langle A\rangle$ with the tomographical procedure (1.66) if the Kernel function $K_{\vec{n}}[A](x)$ defined in (1.65) is bounded. In this case the central limit theorem ensures that the integral (1.66) calculated with Monte Carlo techniques converges for any *a priori* unknown probability distribution $p_{\vec{n}}(x)$. However, nothing guarantees that the Kernel function is bounded, and actually there are cases when it is not. In these cases, one may try to find in the class of equivalent unbiased estimators (*i.e.* estimators differing by a null estimator) one that yields a bounded Kernel function. For estimators of the kind

$$\mathcal{E}'_{\vec{n}}[A](\vec{n}\cdot\vec{U}) = \mathcal{E}_{\vec{n}}[A](\vec{n}\cdot\vec{U}) + \mathcal{N}(\vec{n}\cdot\vec{U}), \tag{1.106}$$

one finds the Kernel functions

$$K'_{\vec{n}}[A](x_{\vec{n}}) = K_{\vec{n}}[A](x_{\vec{n}}) + {}_{\vec{n}}\langle x|\mathcal{N}(\vec{n}\cdot\vec{U})|x\rangle_{\vec{n}} = K_{\vec{n}}[A](x_{\vec{n}}) + \mathcal{N}(x_{\vec{n}})\ , \tag{1.107}$$

with $\mathcal{N}$ having the only constraint

$$\int d\vec{n}\,\mathcal{N}(x_{\vec{n}}) = 0\ . \tag{1.108}$$

Thus, by varying $\mathcal{N}$ in the class of functions that satisfy (1.108), one has to find a bounded K', using an unbounded null function to remove the unbounded part of the Kernel.

Hopefully the renormalization technique may lead to mitigate the exponential divergency of the homodyne tomography Kernel function when the quantum efficiency goes to 50%. This would also enhance the reconstructions for higher η, as one would obtain cleaner (*i.e.* less statistical noise) low-number of data reconstructions. Presently, as already remarked, such a goal has not been achieved.

Chapter 2

State reconstruction techniques.

In this chapter the general theory analyzed previously is exploited by specializing it to obtain the optical homodyne tomography and the spin state tomography. Optical homodyne tomography is historically the first tomographic method and will be easily re-derived from the general formulas, while recent spin tomography [5, 6] is devoted to the reconstruction of unknown spin states of a single –or of more– particles. Homodyne tomography is analyzed in Sect. 2.1 and spin tomography in Sect. 2.2. The Kerr tomography technique (see [33, 34, 35, 36]), a completely different optical state reconstruction method, is examined in Sect. 2.3. Such a technique, based on "photon filtering", allows a reconstruction of the photon number distribution with very little number of data. The apparatus which the technique is based on can also be used for the reconstruction of a truncated radiation density matrix or alternatively, with minor changes in the setup, for the generation of Fock states and of selected superpositions of Fock states. The apparatus relies on a ring cavity coupled to a signal mode through a high Kerr medium. Our Monte Carlo simulations show that the experiment might be feasible with current frontier nonlinear technology.

2.1 Homodyne tomography

In this section we will derive the optical homodyne tomography, which estimates arbitrary operator expectation values on radiation states starting from data collected through homodyne detectors. This is historically the first tomographic method that was proposed and has already been rapidly described in the history section 1.1. Here it will be analyzed starting from the general theory described in Sect. 1. In particular we will see how the noise deriving from imperfect homodyne detection can be beaten applying the noise deconvolution described in Subsect. 1.3.1. Before analyzing the data tomographic technique, we must describe and analyze the homodyne detector.

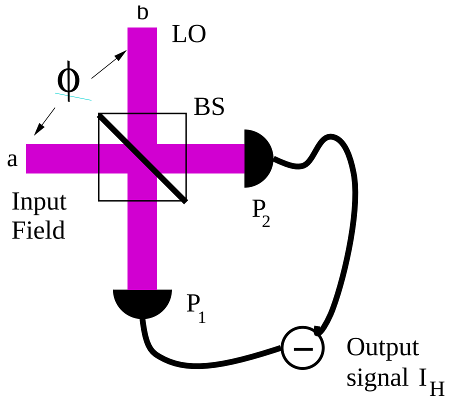

Figure 2.1: Homodyne detector. The input signal (in mode a) is mixed by a 50–50 beam splitter (BS) with a strong pump (LO), which is coherent with the input field and is itself in a coherent state. The relative phase ϕ between the signal and the pump must be known and should be varied randomly in $[0, \pi]$ with uniform probability. Two identical high efficiency linear photodetectors P_1 and P_2 measure the field. The photocurrents are then accurately subtracted electronically and the output data I_H is obtained.

2.1.1 Homodyne Detection

The balanced homodyne detector (see for example in [37]) measures the quadrature observable of the field, defined as in (1.9), *i.e.*

$$x_\phi \overset{\text{def}}{=} \frac{1}{2}(a^\dagger e^{i\phi} + a e^{-i\phi}) \ , \qquad (2.1)$$

where a and $a^\dagger$ are the annihilation and creation operators for the electromagnetic field. The experimental setup is shown in Fig. 2.1. Its components are: a 50-50 beam splitter (BS); two high efficiency linear non–single photon resolving detectors; a circuit for exactly subtracting the photocurrents output by the two detectors; and a strong coherent pump field, called local oscillator (LO) that must be coherent with the input field to be measured, and whose phase ϕ relative to the input field must be varied (and the value of ϕ must be known). Obviously various (optical and–or electronic) filters may be added at the various stages. The experimentally critical and challenging issue comes from the fact that the whole setup must be perfectly balanced, *i.e.* the components must be perfectly symmetrical. In fact one uses the excited coherent pump to amplify the weak quantum signals of the input so that one can use high efficiency detectors that that work fine only with strong signals. However, in order to recover the quantum features, one must remove (by subtracting the two photocurrents at the electronics stage) the strong current coming from the LO detection, leaving only the weak signals.

We now give an intuitive description of the working of the homodyne detector. The input–output transformations of the modes a and b that impinge into a beam splitter with τ transmissivity are

$$c = a\,\sqrt{\tau} + b\,\sqrt{1-\tau}, \quad d = a\,\sqrt{\tau} - b\,\sqrt{1-\tau}\;, \tag{2.2}$$

where c and d are the two beam–splitter output modes, each of which impinge into a different photodetector. In this case we need a 50–50 beam splitter, hence $\tau = \frac{1}{2}$. The difference of the two photocurrents is the homodyne detector's output, and thus it is proportional to

$$c^\dagger c - d^\dagger d = a^\dagger b + b^\dagger a\;, \tag{2.3}$$

where the transformations (2.2) were used with $\tau = \frac{1}{2}$. In the strong local oscillator limit, with mode b in an excited coherent state $|\beta\rangle$ ($\beta \gg 1$), the expectation value of the output is $\langle a^\dagger\rangle\beta + \langle a\rangle\beta^*$. By rescaling the output difference photocurrent with two times the LO amplitude $|\beta|$, since the pump is coherent with mode a and dephased by a phase ϕ, one obtains the output of the homodyne as

$$O = \lim_{|\beta|\to\infty} \frac{|\beta|\left(a\,e^{-i\phi} + a^\dagger\,e^{i\phi}\right)}{2|\beta|} = a_\phi. \tag{2.4}$$

Let us now analyze the detector noise coming from non-unit quantum efficiency η at the detection. As was shown by Mandel, Kelley, and Kleiner [38], an inefficient detector is equivalent to a perfect $\eta = 100\%$ detector, preceded by a beam splitter with transmissivity η. Thus, the action of inefficient photodetection on the overall performance of the detector is obtained by inserting two beam splitters in front of the two photodiodes of the homodyne scheme. Thus, using the relations (2.2), modes c and d become

$$c' = \sqrt{\eta}\,c + \sqrt{1-\eta}\,u \;\text{ and }\; d' = \sqrt{\eta}\,d + \sqrt{1-\eta}\,v\;, \tag{2.5}$$

where u and v are vacuum modes. The homodyne output, proportional to $c'^\dagger c' - d'^\dagger d'$, should now be rescaled also by η and is proportional to

$$\begin{aligned} L &= \eta\,(a^\dagger b + b^\dagger a) + (1-\eta)(u^\dagger u + v^\dagger v) \\ &+\sqrt{\frac{(1-\eta)\eta}{2}}[a(u^\dagger + v^\dagger) + b(u^\dagger - v^\dagger) + a^\dagger(u+v) + b^\dagger(u-v)]\;. \end{aligned} \tag{2.6}$$

As was done above, we take the limit of strong pump b as in (2.4) and rescale the output difference photocurrent by $2|\beta|\eta$. We obtain

$$O = \lim_{|\beta|\to\infty} \frac{L}{2|\beta|\eta} = a_\phi + \sqrt{\frac{1-\eta}{2\eta}}(u_\phi - v_\phi)\;, \tag{2.7}$$

where modes u and v are in the vacuum state.

2.1.2 Quantum homodyne tomography

Here we specify [5, 7, 8] the general group tomography theory of Sect. 1.2 to the case of homodyne tomography [1, 2, 11, 4].

The tomographic group T is the Heisenberg–Weyl group of the displacement operators, and its UIR is given by the unitary operators

$$\mathcal{R}(\alpha) = e^{\alpha a^\dagger - \alpha^* a} \;, \tag{2.8}$$

where a is the annihilation operator of the field mode. If we look at only one mode of the radiation field, then there is only an equivalence class in the Lie algebra. In fact, a basis for its Lie algebra is composed of the operators a and $a^\dagger$, with $[a, a^\dagger] = 1$, and hence the quorum[1] is composed by the quadrature operators a_ϕ, with $\phi \in [0, 2\pi]$. Since the Lie algebra is here two dimensional, its fixed–length vectors are univocally determined by the only parameter ϕ, which here plays the role of $\vec{n}$ introduced in Sect. 1.2. The invariant group measure is given by $d^2\alpha = dx\, dy$, for $\alpha = x + iy$, which, in polar coordinates becomes $d^2\alpha = d\phi\, \frac{dk\, k}{4}$ for $\alpha = \frac{k}{2} e^{i\phi}$, chosen so that $\alpha a^\dagger - \alpha^* a = k\, a_\phi$, and the unbiased homodyne tomographic estimator is

$$\mathcal{E}_\phi[A](a_\phi) = \mathrm{Tr}_1 \left[A \otimes \mathbb{1} \int_0^{+\infty} \frac{dk\; k}{4}\; e^{-ik(a_\phi \otimes \mathbb{1} - \mathbb{1} \otimes a_\phi)} \right] . \tag{2.9}$$

However, since $a_\phi = -a_{\phi+\pi}$, we can restrict the quorum to a_ϕ with $\phi \in [0, \pi]$. Thus, the estimator becomes,

$$\mathcal{E}_\phi[A](a_\phi) = \mathrm{Tr}_1 \left[A \otimes \mathbb{1} \int_{-\infty}^{+\infty} \frac{dk\; |k|}{4}\; e^{-ik(a_\phi \otimes \mathbb{1} - \mathbb{1} \otimes a_\phi)} \right] , \tag{2.10}$$

or, for trace–class operators,

$$\mathcal{E}_\phi[A](a_\phi) = \int_{-\infty}^{+\infty} \frac{dk\; |k|}{4}\; \mathrm{Tr}_1 \left[A\; e^{-ika_\phi} \right]\; e^{+ika_\phi} \; . \tag{2.11}$$

It is now immediate to obtain the formulas of the conventional homodyne tomography, such as Eq. (1.15). In fact, for A trace–class operator one has

$$A = \int_0^\pi \frac{d\phi}{\pi} \int_{-\infty}^{+\infty} \frac{dk|k|}{4}\; \mathrm{Tr}[A\; e^{-ika_\phi}]\; e^{+ika_\phi} \;, \tag{2.12}$$

which is obtained by writing explicitly for the case of homodyne tomography Eq. (1.33). Now the homodyne tomography formula, Eq. (1.15), is obtained by substituting the density matrix ϱ in place of A and by calculating the trace using the complete set of vectors $\{|x_\phi\rangle\}$, eigenvectors of the quadrature a_ϕ.

---

[1] We consider the Hermitian operators that are vectors of *fixed* length $k = \frac{1}{2}$ in the Lie algebra.

2.1.3 Noise deconvolution

In this subsection we apply the noise deconvolution technique, which was presented in Subsect. 1.3.1, to the case of homodyne tomography. In the case of inefficient $\eta < 100\%$ detection, the output of the homodyne is given by Eq. (2.7), where modes u and v are in the vacuum state. In this case the effect Γ of the quantum efficiency on the estimator is given by noticing that

$$\Gamma[\exp(ika_\phi)] = {}_u\langle 0|\, {}_v\langle 0| \exp\left[ik\left(a_\phi + \sqrt{\frac{1-\eta}{2\eta}}(u_\phi - v_\phi)\right)\right] |0\rangle_v |0\rangle_u \tag{2.13}$$

where Eq. (2.7) was used and where the vacuum modes u and v were traced out. Since one has

$$\langle 0|e^{i\lambda u_\phi}|0\rangle = \langle 0|\exp\left[\frac{i\lambda}{2}a\, e^{-i\phi}\right]\exp\left[\frac{i\lambda}{2}a^\dagger\, e^{i\phi}\right] e^{\frac{1}{8}\lambda^2}|0\rangle = e^{-\lambda^2/8}\ , \tag{2.14}$$

we can conclude that

$$\Gamma[\exp(ika_\phi)] = \exp\left(ika_\phi - \frac{1}{8}k^2\Delta^2\right)\ , \tag{2.15}$$

with $\Delta \overset{\mathrm{def}}{=} \sqrt{\frac{1-\eta}{2\eta}}$. Obviously,

$$\Gamma^{-1}[\exp(ika_\phi)] = \exp\left(ika_\phi + \frac{1}{8}k^2\Delta^2\right)\ . \tag{2.16}$$

To obtain the deconvolved estimator (1.98), we need to calculate $\Gamma^{-1}[\widetilde{E}_{\vec{n}}(\vec{n}\cdot\vec{U})]$, that in this case writes

$$\begin{aligned}\Gamma^{-1}\left[\widetilde{E}_\phi(a_\phi)\right] &= \Gamma^{-1}\left[\int_{-\infty}^{+\infty}\frac{dk\ |k|}{4}\ (e^{-ik\ a_\phi}\otimes \mathbb{1})(\mathbb{1}\otimes e^{ik\ a_\phi})\right] \\ &= \int_{-\infty}^{+\infty}\frac{dk\ |k|}{4}\ e^{\frac{1}{4}k^2\Delta^2}\ (e^{-ik\ a_\phi}\otimes \mathbb{1})(\mathbb{1}\otimes e^{ik\ a_\phi})\ .\end{aligned} \tag{2.17}$$

From this equation it is immediate to obtain the Kernel operator of the homodyne tomography for non-unit quantum efficiency that was introduced in Sect. 1.1.3, *i.e.* Eq. (1.20).

For examples of kernels for various operators A, we refer the reader to [4] and [11] that contain the complete theory of conventional homodyne tomography.

In conclusion in this section we derived the principal formulas of conventional quantum homodyne tomography, starting from the general theory of Sect. 1.2. These formulas will be extensively used in Chap. 3, where various applications of homodyne tomography will be proposed and thoroughly studied.

2.2 Particle domain: Spin tomography

In this section we will derive the spin tomography [5, 6], which estimates arbitrary operator expectation values on angular momentum states starting from data collected through Stern–Gerlach devices. As for the case of homodyne tomography, also here the theory follows directly from the general group–formulation of Sect. 1.2. In the first subsection we analyze the case of a system composed of a single spin, using a continuous tomographic group. In the next subsection, the experimental apparatus and some simulations will be given for the reconstruction of the single spin state. In the third subsection an equivalent formulation of the spin tomography is given for the case of spin 1/2 and spin 1 particles in terms of finite tomographic groups, and a comparison to conventional $SU(2)$ group formulation is given. In the following subsection we extend the theory to the multi-particle case. For distinguishable particles the extension is rather trivial. For the indistinguishable particle case, in order to obtain the global density matrix, an analysis of the density operator of indistinguishable multi-particle states and the observability of such a system is needed. This will allow the state reconstruction for spin $\frac{1}{2}$ particles from the measurement of global quantities only. In the last subsection we show the feasibility of the proposed experimental reconstructions.

2.2.1 Single particle continuous spin tomography

Starting from the tomography theorem (1.56), we now specify the physical system as a single spin. In this case $\mathcal{H} = \mathbb{C}^{2s+1}$, s being the spin of the particle. For such a system, we can choose the group $SU(2)$ of 2×2 unitary matrices with unit determinant as tomographic group T. In fact it is a connected Lie group and it induces a unitary irreducible representation on $\mathbb{C}^{2s+1}$. As will be seen in the following, the choice of $SU(2)$ as tomographic group T is not unique. A basis for the Lie algebra of $SU(2)$ is given by the angular momentum operator components s_x, s_y and s_z and the group $SU(2)$ can be parametrized through the "rotation parameters" $(\vec{n}, \psi)$ —where $\vec{n} = (\cos\varphi \sin\vartheta, \sin\varphi \sin\vartheta, \cos\vartheta)$, $\vartheta \in [0, \pi]$, $\varphi \in [0, 2\pi]$, and $\psi \in [0, 2\pi]$. The group elements are obtained through exponentiation of the Lie algebra as

$$\mathcal{R}\left(g(\vec{n}, \psi)\right) = e^{i\psi\, \vec{n}\cdot\vec{s}} , \tag{2.18}$$

where $\vec{s}$ is the particle spin operator. The quorum is the set of operators $\mathcal{Q} = \{\vec{n} \cdot \vec{s}$, with $\vec{n}$ in the unit sphere$\}$, *i.e.* the measurement of the spin in all directions $\vec{n}$. The group invariant measure [27] for $SU(2)$ is, with the $(\vec{n}, \psi)$ parametrization,

$$dg(\vec{n}, \psi) = \frac{2s+1}{4\pi^2} \sin^2 \frac{\psi}{2} \sin\vartheta \; d\psi d\vartheta d\varphi \; . \tag{2.19}$$

The measure (2.19) normalization is such that

$$\int_T dg \; |\langle u|\mathcal{R}(g)|v\rangle|^2 = 1 \; , \tag{2.20}$$

for any two vectors $|u\rangle$ and $|v\rangle$ in $\mathbb{C}^{2s+1}$ as shown in Property 2, given in page 26. It is now easy to obtain the spin tomography starting from the tomography formulas for trace–class operators Eq. (1.67), from which it is possible to find

$$\varrho = \frac{(2s+1)}{4\pi^2}\int_0^{2\pi} d\psi \sin^2\frac{\psi}{2}\int_0^{\pi} d\vartheta \sin\vartheta \int_0^{2\pi} d\varphi \; \mathrm{Tr}\left[\varrho\, e^{-i\vec{s}\cdot\vec{n}\,\psi}\right]\; e^{i\vec{s}\cdot\vec{n}\,\psi}\;. \tag{2.21}$$

Evaluating the trace over the complete set of vectors $|\vec{n},m\rangle$ (which are the eigenstates of $\vec{s}\cdot\vec{n}$, relative to the eigenvalue m), we find

$$\varrho = \int \frac{d\vec{n}}{4\pi}\sum_{m=-s}^{s} p_{\vec{n}}(m)\; K_s(m-\vec{s}\cdot\vec{n})\;, \tag{2.22}$$

by defining the Kernel operator as

$$K_s(x) \overset{\text{def}}{=} \frac{(2s+1)}{\pi}\int_0^{2\pi} d\psi \sin^2\frac{\psi}{2}\; e^{-i\psi x}\;, \tag{2.23}$$

and by noticing that $\langle\vec{n},m|\varrho|\vec{n},m\rangle = p_{\vec{n}}(m)$ is the probability of obtaining the eigenvalue m when measuring the spin in the $\vec{n}$ direction. Notice the strong analogy of Eq. (2.22) to the homodyne tomography formula (1.15), analogy that is obviously due to the general group theory framework from which the two formulas can be made to derive.

How do we use formula (2.22)? In order to measure the matrix elements $\varrho_{il} = \langle a_i|\varrho|a_l\rangle$ for all i,l ($\{|a_i\rangle\}$ being a basis for $\mathcal{H}_s$), we only need to calculate $\langle a_i|K_s(m-\vec{s}\cdot\vec{n})|a_l\rangle$ and to measure $p_{\vec{n}}(m)$.

The most convenient choice for the basis $\{|a_i\rangle\}$ is the set $\{|m\rangle\}$ of eigenvectors of s_z ($m=-s,\ldots,s$). Thus, the calculation of the matrix elements of the kernel operator, by defining $\lambda_{l,m} \overset{\text{def}}{=} \langle l|\vec{n},m\rangle$, yields

$$\begin{aligned}\langle i|K_s(m-\vec{s}\cdot\vec{n})|l\rangle &= \frac{(2s+1)}{\pi}\int_0^{2\pi} d\psi \sin^2\frac{\psi}{2}\sum_{m'=-s}^{s} e^{-i\psi(m-m')}\lambda_{i,m'}\lambda^*_{l,m'}\\ &= (2s+1)\left(\lambda_{i,m}\lambda^*_{l,m} - \frac{\lambda_{i,m+1}\lambda^*_{l,m+1}+\lambda_{i,m-1}\lambda^*_{l,m-1}}{2}\right)\;.\end{aligned} \tag{2.24}$$

Observing that

$$|\vec{n},m\rangle = e^{-i\vartheta\vec{s}\cdot\vec{n}_\perp}|m\rangle\;, \tag{2.25}$$

with $\vec{n}_\perp \overset{\text{def}}{=} (-\sin\varphi,\cos\varphi,0)$, the evaluation of $\lambda_{l,m}$ is given by

$$\begin{aligned}\lambda_{l,m} &= \langle l|e^{i\vartheta(\sin\varphi s_x-\cos\varphi s_y)}|m\rangle = \langle l|e^{-i\varphi s_z}e^{-i\vartheta s_y}e^{i\varphi s_z}|m\rangle\\ &= e^{i\varphi(m-l)}\sqrt{(s+m)!(s-m)!(s+l)!(s-l)!}\\ &\quad\times\sum_\nu \frac{(-1)^\nu(\cos\frac{\vartheta}{2})^{2s+m-l-2\nu}(-\sin\frac{\vartheta}{2})^{l-m+2\nu}}{(s-l-\nu)!(s+m-\nu)!(\nu+l-m)!\nu!}\;,\end{aligned} \tag{2.26}$$

where the sum is performed over the values of ν for which the argument of the factorials is non-negative. In the last equality we used Wigner's formula [39].

2.2.2 Single particle spin tomography experiment

In this section we will present the method by which, starting from the formulas for tomographic spin derived in the previous subsection 2.2.1, the quantum state of a single spin state may be recovered experimentally through an apparatus derived from a conventional Stern–Gerlach scheme. The experimental setup must provide the measurement of the probability $p_{\vec{n}}(m)$ of formula (2.22). Since the integral of (2.22) is evaluated with Monte Carlo techniques (as shown in Sect. 1.2.4) no binning of the experimental results should be made, but the obtained results should be inserted directly in the sampling formula (1.86). The setup that will here be described, suitable for non charged particles, is depicted in Fig. 2.2. The beam of particles we want to measure the state of impinges onto a Fizeau filter, which selects one velocity (in the x direction) for the particles. This is needed in order to assure that each particle spends the same amount of time t in the subsequent magnetic field $\vec{B}_1$. The field $\vec{B}_1$, which is parallel to the xy plane, is chosen so that $\vec{B}_1 = B_1\vec{n}_\perp = B_1(-\sin\varphi, \cos\varphi, 0)$. In such way, its effect on the spin state ϱ results in the unitary transformation $U^\dagger \varrho\, U$, with

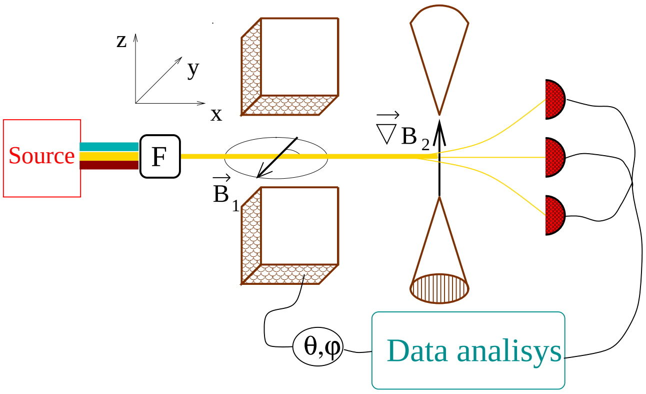

Figure 2.2: Experimental apparatus for spin tomography. The Fizeau filter (F in the figure) selects particles with the same velocity from an incoming beam. These are then injected into a magnetic field $\vec{B}_1$, which forms an angle φ with the y-axis and has intensity proportional to ϑ. For the tomographic reconstruction the phases ϑ and φ need to be varied during the experiment. The remaining part of the apparatus is a conventional Stern–Gerlach scheme (in the figure we show the case of spin $s = 1$ as an example). A computer finally correlates the experimental results with the parameters ϑ and φ, in order to reconstruct the density matrix, according to formula (2.21).

$$U = \exp\left[i\gamma B(\sin\varphi s_x - \cos\varphi s_y)t\right] \ . \tag{2.27}$$

Eq. (2.27) follows from the Hamiltonian $H = -\vec{\mu}\cdot\vec{B}$, with $\vec{\mu} \overset{\text{def}}{=} \gamma\hbar\vec{s}$ ($\vec{\mu}$ being the intrinsic magnetic moment of the particle, and γ its gyromagnetic factor). Successively, the particles cross a gradient of magnetic field $\vec{B}_2$, whose effect is to split the beam, giving a measure of s_z for the state $U^\dagger\varrho\, U$, as in a Stern–Gerlach experiment. In this way we obtain the probability $\langle m|U^\dagger\varrho\, U|m\rangle$, which is equal to $p_{\vec{n}}(m)$ by choosing $B_1 = -\vartheta/(\gamma t)$, and by using Eq. (2.25). Therefore, by controlling the field $\vec{B}_1$, we obtain $p_{\vec{n}}(m)$ for all $\vec{n}$. In fact the direction of $\vec{B}_1$ selects φ, while its intensity B_1 selects ϑ. Now, in order to reconstruct the density matrix, only data analysis is needed, *i.e.* the insertion of the measured $p_{\vec{n}}(m)$ into Eq. (2.22). In practice, a rather small number of data is required to obtain negligible errors, as we will show by numerically simulating the experiment.

We now present two examples of a numerically simulated tomographic reconstruction. We first simulate the case of a coherent spin state, *i.e.*

$$|\alpha\rangle_s \stackrel{\rm def}{=} e^{\alpha s_+ - \alpha^* s_-}\;|-s\rangle\;, \qquad \alpha\in\mathbb{C}\;, \tag{2.28}$$

where $s_\pm \stackrel{\rm def}{=} s_x \pm i s_y$. Notice the similarity with the customary optical coherent state, defined as $|\alpha\rangle \stackrel{\rm def}{=} e^{\alpha a^\dagger - \alpha^* a}|0\rangle$, where a is the annihilator operator for the optical mode and $|0\rangle$ is the vacuum state. In Figs. 2.3 and 2.4 we show the reconstructed density matrix $\varrho_{coh} = |\alpha\rangle_{s\,s}\langle\alpha|$ resulting from a Monte Carlo simulated experiment.

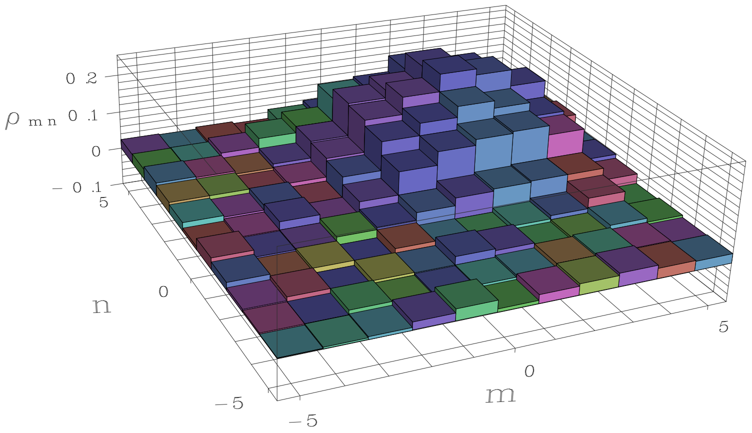

Figure 2.3: Simulation of the reconstruction of the density matrix for a coherent spin state ϱ_{coh}. The parameters for the state are $\alpha = 1$ and $s = 5$. The simulation is performed using 3000 spin measurements to generate the density matrix.

We now give a simulation of a thermal spin state, which is the mixture defined by

$$\varrho_{th} \stackrel{\rm def}{=} \frac{e^{-\epsilon s_z}}{\mathrm{T}r[e^{-\epsilon s_z}]}\;, \qquad \epsilon\in\mathbb{R}\;. \tag{2.29}$$

Physically this state describes a gas of non interacting spins in thermal equilibrium with a reservoir at a temperature T and in the presence of a magnetic field B_z parallel

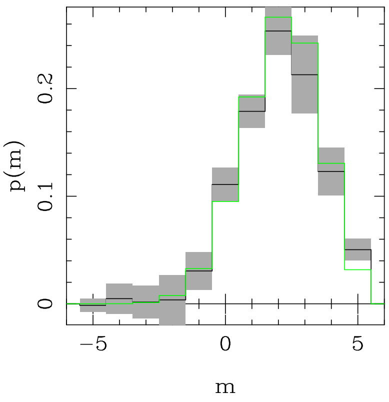

Figure 2.4: Diagonal elements of the matrix given in Fig. 2.3. The error bars are obtained, as described in Sect. 1.2.4, by dividing the measurements into 10 statistical blocks and using the procedure described in Sect. 1.2.4. The solid line indicates the theoretical value.

to the z-axis, *i.e.* $\epsilon = -\gamma\hbar B_z/(K_B T)$, where K_B is the Boltzmann constant. In Fig. 2.5 we show the simulated reconstruction of ϱ_{th}, and in Fig. 2.6 its diagonal.

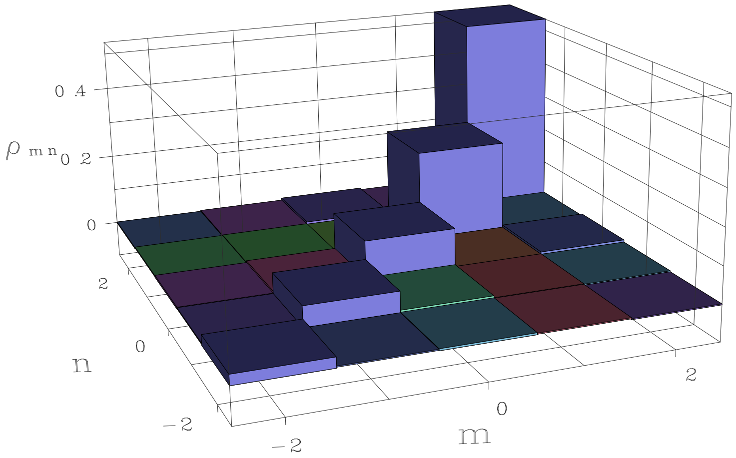

Figure 2.5: Density matrix for a thermal spin state ϱ_{th}. Here $\epsilon = .75$ and $s = 2$. A number of 60000 simulated measurements have been used in the reconstruction.

2.2.3 Discrete spin tomography

Up to now $SU(2)$ has been used as tomographic group T for the reconstruction of the spin density matrix. This choice for T is not unique. For example, in the case of spin

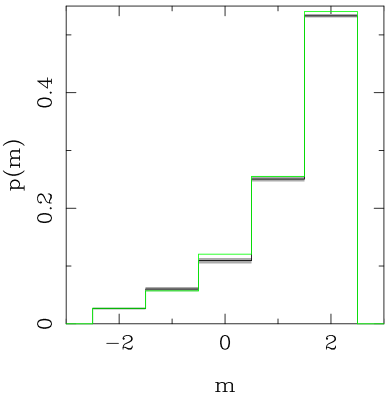

Figure 2.6: Main diagonal of the matrix given in Fig. 2.5. The error bars, which in this case are practically negligible, are obtained by dividing the measurements into 10 statistical blocks. The solid line indicates the theoretical value.

$s = \frac{1}{2}$, it is possible to use also the group defined as $T \overset{\mathrm{def}}{=} \{i\vec{\sigma}, -i\vec{\sigma}, \mathbb{1}, -\mathbb{1}\}$, where $\vec{\sigma}$ is the vector of Pauli matrices. The following irreducible unitary representation on $\mathbb{C}^2$ exists

$$\begin{aligned} &\mathcal{R}(i\sigma_\alpha) = \mathcal{R}(-i\sigma_\alpha) = \sigma_\alpha,\ \alpha = x,\ y,\ z \\ &\mathcal{R}(\mathbb{1}) = \mathcal{R}(-\mathbb{1}) = \mathbb{1}\ . \end{aligned} \tag{2.30}$$

Using this representation, from the tomography theorem (1.56), which can be used here as this finite group is a subgroup of the Lie group of the rotation matrices, we obtain

$$\varrho = \sum_{m=-1/2}^{1/2} \sum_{\alpha=x,y,z} p(\vec{n}_\alpha, m) m \sigma_\alpha + \frac{1}{2}\ . \tag{2.31}$$

Notice that, by using Eq. (2.31) it is sufficient to measure the spin in only three directions.

Analogously, for spin $s = 1$ it is possible to find a finite group in alternative to $SU(2)$. In fact, consider the 12 element tetrahedric group composed of the $\pm\frac{2}{3}\pi$ rotations around the versors $\{\vec{n}_1 = \frac{1}{\sqrt{3}}(1,1,1),\ \vec{n}_2 = \frac{1}{\sqrt{3}}(1,-1,-1),\ \vec{n}_3 = \frac{1}{\sqrt{3}}(-1,1,-1),\ \vec{n}_4 = \frac{1}{\sqrt{3}}(-1,-1,1)\}$, of the π rotations around $\{\vec{n}_5 = (1,0,0),\ \vec{n}_6 = (0,1,0),\ \vec{n}_7 = (0,0,1)\}$ and of the identity. It induces a unitary irreducible representation on the space $\mathbb{C}^3$, given by the 3×3 rotation matrices. Hence, Eq. (2.22) now becomes

$$\varrho = \frac{1}{4} \sum_{m=-1}^{1} \sum_{j=1}^{7} p(\vec{n}_j, m) \mathcal{K}_j(m - \vec{s} \cdot \vec{n}_j) + \frac{1}{4}\mathbb{1}\ , \tag{2.32}$$

with

$$\mathcal{K}_j(x) = \left\{ \begin{array}{cc} 2\cos(\frac{2}{3}\pi x) & j = 1, \cdots, 4 \\ e^{-i\pi x} & j = 5, 6, 7 \end{array} \right. . \tag{2.33}$$

Notice that this last procedure does not make use of a minimal set of measurements, since 14 experimental parameters must be determined in (2.32), whereas there are only 8 independent real parameters in the 3×3 density matrix. On the contrary, the case of spin $s = \frac{1}{2}$ outlined previously does use the minimal set of measurements for such a system. In Fig. 2.7 a comparison between the two procedures for spin tomography given by the continuous $SU(2)$ tomography of Eq. (2.22) and discrete tomography of Eqs. (2.31) and (2.32) is shown through a Monte Carlo simulation. Notice that there is no significant difference in the results, showing that there is no substantial need for a procedure which involves a minimal set of measurements. For spins $s > 1$ an analogous procedure holds: one needs to find a finite group such that it induces an irreducible unitary representation on $\mathcal{H} = \mathbb{C}^{\,2s+1}$.

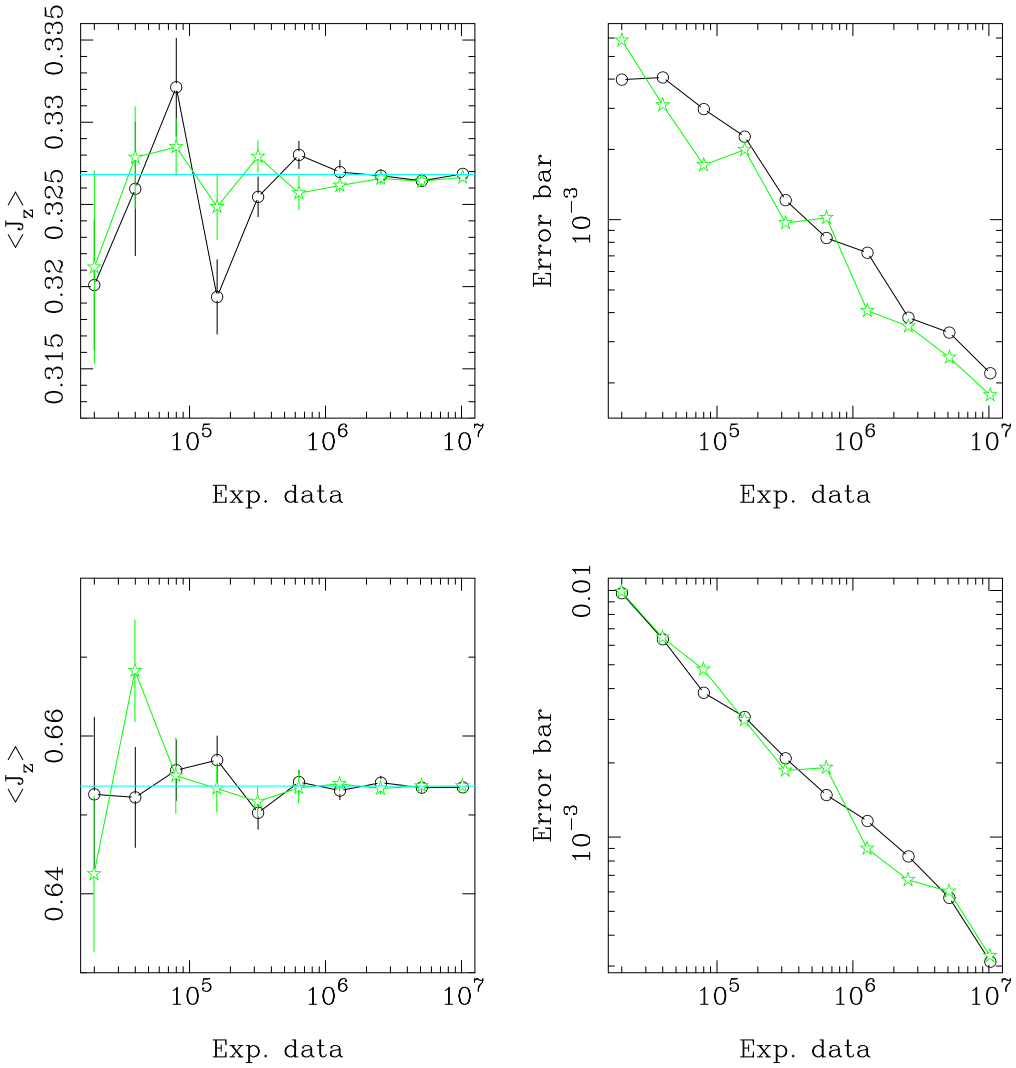

Figure 2.7: Monte Carlo comparison between continuous and discrete tomography. Continuous tomography uses $SU(2)$ as tomographic group and is based on Eq. (2.22), while discrete tomography uses $SU(2)$ finite subgroups and is based on the reconstruction procedures given in Eq. (2.31) for $s = \frac{1}{2}$ and Eq. (2.32) for $s = 1$. Left: Convergence of the mean value of $\langle s_z \rangle$ for a coherent $\alpha = 2$ spin state for increasing number of experimental data (the theoretical value is given by the horizontal lines). The circles refer to continuous, the stars to discrete tomography. The upper graph is for spin $s = \frac{1}{2}$, the lower is for $s = 1$. Right: Plots of the statistical error bars of the graphs on the left *vs.* experimental data. The error bars are obtained by dividing the experimental data into 20 statistical blocks. Notice that the two tomographic procedures are essentially equivalent and that the error scales as $\propto \frac{1}{\sqrt{N}}$ as shown in Sect. 1.2.4.

2.2.4 Many particle spin tomography

The mathematical extension of the method to the case of a system composed of many spins is trivial, yet, it predicts the necessity of performing measurements on single components and this may not always be possible. For this reason, we need to further develop the theory.

Distinguishable spins.

As tomographic group for a system of N spins we can simply use $SU(2)^N$. Since in the case of direct product of Lie groups, the Lie algebra of the product group is given by the direct sum of the single group algebras, the quorum is given by the direct sum of observables living in the single particle Hilbert space $\mathbb{C}^{\,2s+1}$. In this case, it is necessary to use the general notation introduced in Sect. 1.2.2, and to divide the Lie algebra into equivalence classes. As a consequence, the Lie coordinates vector $\vec{a}$ is written as $\vec{a} = (\vec{n}_1, \psi_1; \cdots; \vec{n}_L, \psi_L)$, where $(\vec{n}_i, \psi_i)$ are the Lie coordinates of the operators in the Lie algebra of the ith particle. As an immediate consequence of the tomography theorem (1.56), we obtain that

$$\langle A\rangle = \prod_{i=1}^{N} \int d\vec{n}_i \int d\psi_i \int dx\; p_{\vec{n}_i}(x)\; \mathrm{Tr}[A e^{-i\psi_i(\vec{n}_i\cdot\vec{U}-x)}]\;, \tag{2.34}$$

where each of the N triple integrals in the above product may be evaluated using the methods already analyzed in Sect. 2.2.2 for the tomographic reconstruction of the single particle. In fact, up to equivalences, the UIR of $SU(2)^N$ are given by the direct product of N operators (2.18) and the invariant measure is the product of N measures (2.19). Thus, we attain readily the following generalization of Eq. (2.21)

$$\begin{aligned} \varrho = \prod_{i=1}^{N} \frac{(2s_i+1)}{4\pi^2} \int_0^{2\pi} d\psi_i \sin^2\frac{\psi_i}{2} \int_0^{\pi} d\vartheta_i \sin\vartheta_i \\ \times \int_0^{2\pi} d\varphi_i\; \mathrm{Tr}\left[\varrho\; e^{-i\vec{s}_i\cdot\vec{n}_i\;\psi_i}\right]\; e^{i\vec{s}_i\cdot\vec{n}_i\;\psi_i}\;, \end{aligned} \tag{2.35}$$

where i is the particle index. Evaluating, as usual, the trace term in (2.35) on the eigenvectors of the quorum operators $\vec{n}_i\cdot\vec{s}_i$ we introduce the probability $p(\vec{n}_1, m_1; \cdots; \vec{n}_N, m_M)$ of obtaining m_i as result for the measurement of the ith spin $\vec{s}_i$ in the direction $\vec{n}_i$. This information is accessible only in the case of fully distinguishable spins. For the case of indistinguishable particles, some considerations are in order and we refer the reader to the following subsection.

Instead of using $SU(2)^N$ one may also use other groups for the single particle spaces, as seen in Sect. 2.2.3, and generalizations of formulas (2.31) and (2.32) follow immediately.

In Fig. 2.8 a simulated tomographic reconstruction of the value of $\langle S_z \rangle$ (S_z being the total spin component in the z-direction) is given for different multi-particle spin states. Notice how the number of the necessary experimental data increases exponentially with the number of spins, since the statistical error is exponential in the number of particles.

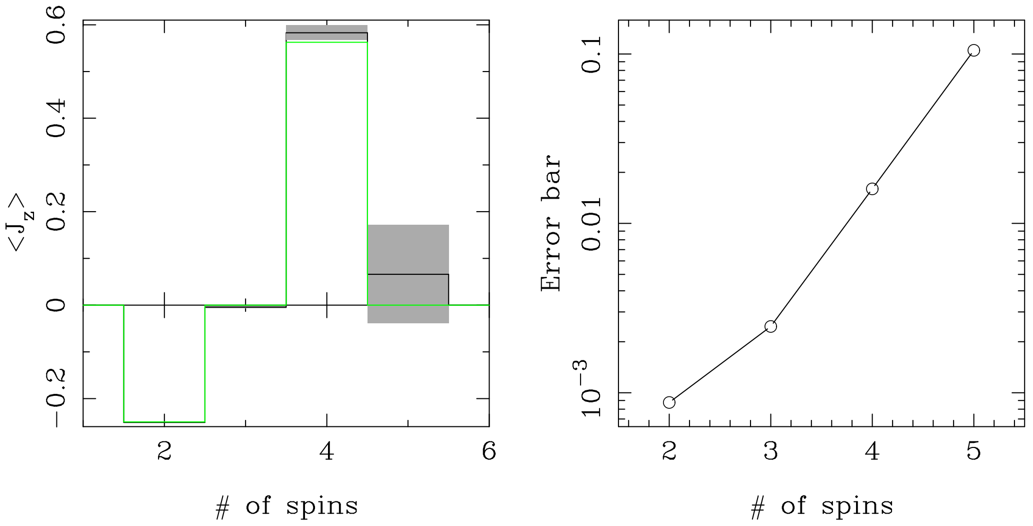

Figure 2.8: Left: Plot of $\langle S_z \rangle$ for different number of spins in a completely symmetrical state. A total of 10^6 measurements for each mean value was performed in this simulation. Right: Semi-log plot of the error bars *vs.* the number of spins. Notice the exponential increase in the statistical errors.

Indistinguishable spin $1/2$ particles.

In this subsection we will analyze the case of indistinguishable spins. The general theory for the reconstruction of the spin density matrix of such a system is lacking, whereas it can be obtained and will be here described for the case of spin $\frac{1}{2}$ [40].

Suppose we were given a system of N particles with the same spin. Such particles may be treated as identical by introducing a new dynamical variable, as in the case of the isospin. The spin density matrix (which is the partial trace over the orbital degrees of freedom of the global density matrix) is completely symmetrical, *i.e.*

$$P \varrho P^{-1} = \varrho \,, \tag{2.36}$$

for any particle permutation P, because of the complete symmetry of the global density matrix that describes both the spin and the orbital degrees of freedom.

It is also possible to see that the spin density matrix is block diagonal in the representation of vectors of definite symmetry, with the subspace corresponding to each block spanned by vectors belonging to the same symmetry. In fact, given $|\phi\rangle$ and $|\psi\rangle$ vectors of different symmetry type [41], then $\langle\phi|\psi\rangle = 0$. Hence, for any operator ϱ, satisfying (2.36), one has $\langle\phi|\varrho|\psi\rangle = 0$, as $\varrho|\psi\rangle$ belongs to the same symmetry type as $|\psi\rangle$.

Since the square of the total spin S^2 and its z component S_z both commute with all permutation operators P, the common eigenvectors of S^2 and S_z may be taken as a basis for each of the diagonal blocks of the spin matrix. Let us now restrict our attention to $s = 1/2$ spin particles. In this case, to each symmetry type there corresponds only one value of S, where $S(S+1)$ is the eigenvalue of S^2. In fact, given $[\lambda_1\lambda_2]$ the partition of N which defines the class of permutations P that indicate a symmetry type, we find $S = \frac{1}{2}(\lambda_1 - \lambda_2)$ [42].

Let $\mathcal{H}_{S,M}$ be the space of vectors with assigned S and M (M being the eigenvalue of S_z). The spin density matrix restricted to $\mathcal{H}_{S,M}$, which is given by $\varrho_{S,M}$, is again completely symmetrical, hence $[P, \varrho_{S,M}] = 0$. Moreover, $\mathcal{H}_{S,M}$ is associated with an irreducible representation of the permutations group [42]. By using Schur's lemma, we can thus conclude that $\varrho_{S,M} \propto \mathbb{1}$, $\mathbb{1}$ being the identity in $\mathcal{H}_{S,M}$. In $\mathcal{H}_{S,M}$ there may be vectors of different symmetry type i, yet $\langle i, S, M|\varrho_{S,M}|i, S, M\rangle$ does not depend on the index i, so that the probability for the measurement of S^2 and S_z does not depend on the symmetry type. The same conclusion holds for the measurement of S^2 and $\vec{S}\cdot m$ for any versor $\vec{m}$. Hence, from the arbitrariness of $\vec{m}$, we conclude that blocks with the same S (and different symmetry type) are coincident.

In conclusion, we have proved that in the $\{S^2\}$ representation ϱ is block diagonal, that each block corresponds to a value of S and that blocks with the same S are equal. Hence, once more we can make use of the general theory of Sect. 1.2.2. In fact, here the Lie algebra is a direct sum of spin operators $\vec{s}_i$, acting on $\mathbb{C}^{2i+1}$ with $i = a,\ a+1, \cdots, N/2$ ($a = \frac{1}{2}$ for N odd, and $a = 0$ for N even). Thus, from the tomography theorem, (1.56) and using the formula (2.22) we find that each block of the density matrix is of the form

$$\varrho_i = \frac{(2s_i+1)}{4\pi^2}\int_0^{2\pi} d\psi_i \sin^2\frac{\psi_i}{2}\int_0^{\pi} d\vartheta_i \sin\vartheta_i \int_0^{2\pi} d\varphi_i \ \mathrm{Tr}\left[\varrho\ e^{-i\vec{s}_i\cdot\vec{n}_i\ \psi_i}\right]\ e^{i\vec{s}_i\cdot\vec{n}_i\ \psi_i}, \tag{2.37}$$

and

$$\varrho = \bigotimes_i d_i\varrho_i\ , \tag{2.38}$$

where d_i is the number equal ϱ_i blocks contained in ϱ. In conclusion, applying Eq. (2.22) to each block, we can reconstruct ϱ measuring only the global quantities S^2 and $\vec{S}\cdot\vec{n}$.

Some examples will clarify both the theory and the needed experimental setup.

In the case of two spins 1/2, the spin density matrix will be of the form

$$\varrho = \begin{pmatrix} \sigma_{11} & \sigma_{12} & \sigma_{13} & 0 \\ \sigma_{21} & \sigma_{22} & \sigma_{23} & 0 \\ \sigma_{31} & \sigma_{32} & \sigma_{33} & 0 \\ 0 & 0 & 0 & \alpha \end{pmatrix} \overset{\text{def}}{=} \sigma \oplus \alpha \,, \tag{2.39}$$

where the σ block corresponds to the subspace spanned by the eigenstates of $S = 1$ (which are symmetrical with respect to particles permutations), while the α block to the subspace spanned by the only eigenvector of $S = 0$ (anti–symmetrical with respect to permutations). Applying (2.22) to each block one finds

$$\begin{aligned} \varrho &= \int \frac{d\vec{n}}{4\pi} \sum_{M=-1}^{1} p(S = 1, \vec{S}\cdot\vec{n} = M)\, K_1(M - \vec{S}\cdot\vec{n}) \\ &\oplus \; p(S = 0). \end{aligned} \tag{2.40}$$

According to (2.40), in order to measure ϱ, we only need the probability distributions $p(S, \vec{S}\cdot\vec{n})$, corresponding to the operators S^2 and $\vec{S}\cdot\vec{n}$, for all $\vec{n}$, which can be suitably recovered using the apparatus depicted in Fig. 2.9, which will be analyzed later.

Similarly, the spin density matrix of three spins 1/2 is

$$\varrho = \begin{pmatrix} \xi_{11} & \xi_{12} & \xi_{13} & \xi_{14} & 0 & 0 & 0 & 0 \\ \xi_{21} & \xi_{22} & \xi_{23} & \xi_{24} & 0 & 0 & 0 & 0 \\ \xi_{31} & \xi_{32} & \xi_{33} & \xi_{34} & 0 & 0 & 0 & 0 \\ \xi_{41} & \xi_{42} & \xi_{43} & \xi_{44} & 0 & 0 & 0 & 0 \\ 0 & 0 & 0 & 0 & \pi^1_{11} & \pi^1_{12} & 0 & 0 \\ 0 & 0 & 0 & 0 & \pi^1_{21} & \pi^1_{22} & 0 & 0 \\ 0 & 0 & 0 & 0 & 0 & 0 & \pi^2_{11} & \pi^2_{12} \\ 0 & 0 & 0 & 0 & 0 & 0 & \pi^2_{21} & \pi^2_{22} \end{pmatrix} . \tag{2.41}$$

The ξ block corresponds to $S = 3/2$, whereas the π blocks both correspond to $S = 1/2$, and are distinguished by their different symmetry properties. The argument presented previously proves that $\pi^1_{ij} = \pi^2_{ij}$, for all i, j, thus we can write $\varrho = \xi \oplus \pi \oplus \pi$, with $\pi \overset{\text{def}}{=} \pi^1 = \pi^2$. Again, applying (2.22) to each block leads to

$$\xi = \int \frac{d\vec{n}}{4\pi} \sum_{M=-\frac{3}{2}}^{\frac{3}{2}} p(S = \frac{3}{2}, \vec{S}\cdot\vec{n} = M)\, K_{\frac{3}{2}}(M - \vec{S}\cdot\vec{n}) \,, \tag{2.42}$$

$$\pi = \int \frac{d\vec{n}}{4\pi} \sum_{M=-\frac{1}{2}}^{\frac{1}{2}} \frac{1}{2}\, p(S = \frac{1}{2}, \vec{S}\cdot\vec{n} = M)\, K_{\frac{1}{2}}(M - \vec{S}\cdot\vec{n}) \,, \tag{2.43}$$

and the problem of determining ϱ is again reverted to the simultaneous measurement of S^2 and $\vec{S}\cdot\vec{n}$.

Both in the cases presented and in the general N spins case, the required experimental data are the distributions $p(S, \vec{S}\cdot\vec{n})$. The apparatus to produce such data are basically equivalent in the two cases, as evident in Figs. 2.9 and 2.10, hence we shall limit the analysis to the two spins case. Here, the Fizeau filter and the magnetic field $\vec{B}_1 = B_1\vec{n}_\perp = B_1(-\sin\varphi, \cos\varphi, 0)$ have the same purpose as in single particle tomography (Fig. 2.2).

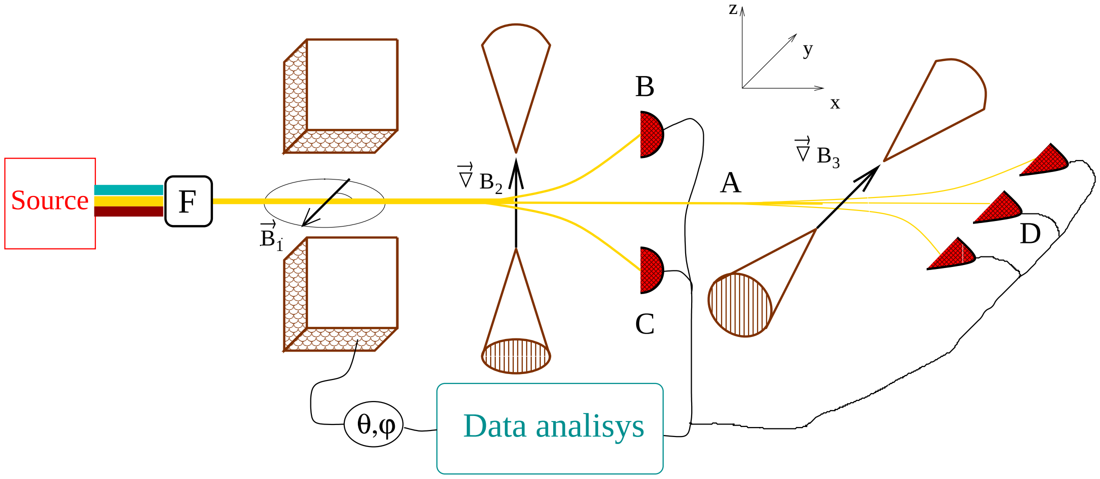

Figure 2.9: Experimental apparatus for the tomography of systems composed of two spins $\frac{1}{2}$.

Consider a beam of n non–interacting systems composed of two particles with spin 1/2. As the analysis can be immediately extended to a mixed case, for simplicity let us consider each system in the pure state

$$|\Psi_o\rangle = \gamma^s|0,0\rangle + \gamma^a_{-1}|1,-1\rangle + \gamma^a_0|1,0\rangle + \gamma^a_1|1,1\rangle\,, \tag{2.44}$$

with $|a,b\rangle$ standing for $|S = a, M = b\rangle$. The beam is split into three parts by the gradient $\vec{B}_2$, and the systems arrive in detector B with a probability $p(S = 1, M = 1) = |\gamma^a_1|^2$ and in detector C with a probability $p(S = 1, M = -1) = |\gamma^a_{-1}|^2$. The remaining particles reach position A with a probability

$$p_A = |\gamma^s|^2 + |\gamma^a_0|^2 \tag{2.45}$$

and are left in the state

$$|\Psi_A\rangle = \frac{1}{p_A}\xi\,(\gamma^s|0,0\rangle + \gamma^a_0|1,0\rangle). \tag{2.46}$$

As the subsequent gradient is directed along the y axis, Eq. (2.46) is conveniently written using the eigenstates of S_y, *i.e.* $|S,M\rangle_y$:

$$|\Psi_A\rangle = \frac{1}{p_A}\,[\gamma^s|0,0\rangle_y + \gamma^a_0\,\alpha_{-1}|1,-1\rangle_y + \gamma^a_0\,\alpha_0|1,0\rangle_y$$

$$+\gamma_0^a\,\alpha_1|1,1\rangle_y]\,, \tag{2.47}$$

where $\alpha_i \overset{\text{def}}{=} {}_y\langle 1,i|1,0\rangle$ $(i=-1,0,1)$. Hence, the probability for a system to arrive at detector D is

$$p_S = \frac{1}{p_A}\,\left[|\gamma^s|^2 + |\gamma_0^a|^2\,|\alpha_0|^2\right]. \tag{2.48}$$

By measuring p_A and p_S, the quantities $|\gamma^s|^2$ and $|\gamma_0^a|^2$ are obtained by inverting equations (2.45) and (2.48). The coefficients $|\gamma_0^a|^2$, $|\gamma^s|^2$, $|\gamma_1^a|^2$ and $|\gamma_{-1}^a|^2$ are the four probabilities $p(S,M)$ we need for the reconstruction given by Eq. (2.40).

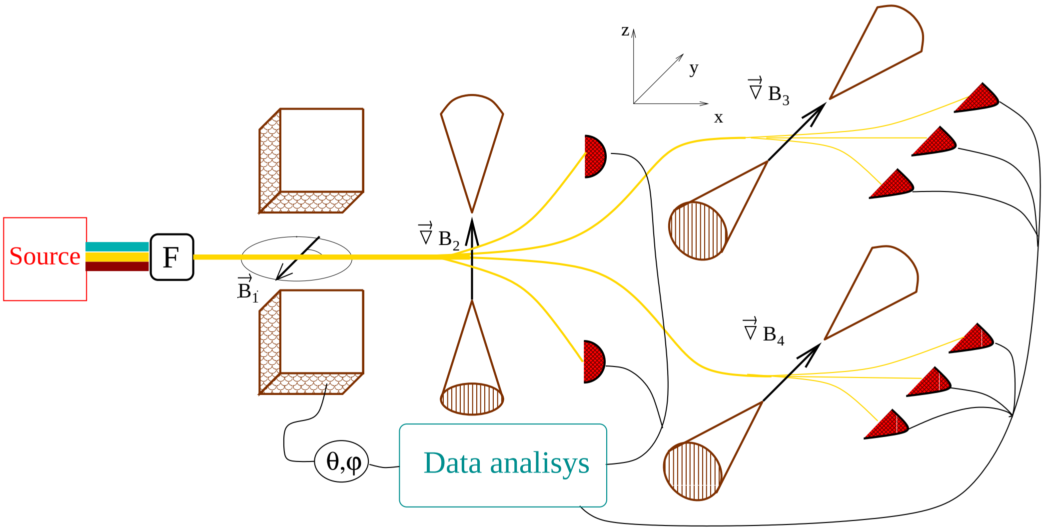

Figure 2.10: Experimental apparatus for the tomographic reconstruction of the spin states of systems composed of three spin $\frac{1}{2}$ states.

A similar argument shows that the equipment of Fig. 2.10 provides $p(S,M)$, for all S,M, for a system constituted of three spins 1/2.

2.2.5 Feasibility and conclusions

Notice that the orders of magnitude of the experimental parameters are such that the experiment is feasible with currently available technology. Only as an example, consider the following cases of spin measurements of electrons or nucleons. For the magnet which is responsible for the field $\vec{B}_1$ with length of the order of 1 cm, we can measure the state of a beam of electrons with speed $\sim 10^9$ cm/sec, by using a magnetic field $B_1 = \vartheta/\gamma t$ varying between 0 and ~ 30 $gauss$. On the other hand, in the nucleon case, choosing a speed of $\sim 10^7$ cm/sec, we need B_1 ranging between 0 to $\sim 10^2 \div 10^3$ $gauss$. Obviously, the parameters B_1 and t can be adjusted over a wide range, according to the experimental situation.

In conclusion, we have presented a tomographic experimental procedure for the measurement of the spin density matrix. The experimental scheme is a consequence of formula (2.21), which we proved from the general group theory tomographic formalism. Through some Monte Carlo simulations, we have shown that the reconstruction can be achieved with high precision using a limited number of measurements. Moreover, we have shown that the orders of magnitude for the experimental setup are such that it can be implemented with currently available technology.

2.3 Kerr tomography

In this section a completely different approach to optical quantum state reconstruction is described and is compared to optical homodyne. The reconstruction technique is based on an experimental setup, called 'Quantum Fock Filter' which was theoretically developed and analyzed by our group in Pavia [33, 34, 35, 36]. The Fock filter was conceived for the generation of optical Fock states, but can be used also to efficiently measure the photon distributions of unknown input states, and thus, by applying the procedure developed by Opatrný and Welsch [19] a truncated density matrix in the Fock basis may be obtained. The derivation of this state reconstruction method from the general theoretical framework of Sect. 1.2 can be derived, but will not be given here since on one hand this is not an unbiased state reconstruction procedure (there is a truncation parameter) and on the other hand this device is really efficient only for the measurement of the photon probability, and not for the state measurement. Thanks to its robustness to noise, this setup can be used as state measurement device (as opposed to conventional homodyne tomography) if the available photodetectors have low efficiency. The experimental scheme is based on coupling a signal field to a ring cavity through cross-Kerr phase modulation, and on conditional ON-OFF photodetection at the output cavity mode. Remarkably, the detector's quantum efficiency does not affect the reliability of the state synthesis, or of the distribution measurement (as we will see, it affects only the normalization).

As already anticipated, the same setup apart from measuring the photon distribution of unknown quantum states, can be also used to prepare the radiation field in a Fock state or in a selected superposition of Fock states or entangled two-mode states. An analysis of this operation is in order, since the Fock state generator is useful for many of the experimental setups that will be seen in this thesis. The generation of optical radiation number (Fock) states is of importance for a number of different applications, ranging from high resolution spectroscopy to fundamental tests of Quantum Mechanics. In quantum communication, Fock states achieve the optimal capacity of quantum channels [43], whereas in optical quantum computation superpositions of Fock states are needed as input states [44, 45]. Moreover, the synthesis of Fock states allows to experimentally characterize active optical devices [46]. The proposed setup can also be used to synthesize two-mode entangled states by using an additional Kerr medium, with possible applications in quantum information and quantum teleportation technology. In our proposal, a traveling wave mode is coupled to a ring cavity through cross-Kerr phase modulation. The cavity mode serves as a probe, and a successful photodetection at the cavity output reduces the signal mode to a predetermined output state. The scheme works with high-Q cavities, conventional ON-OFF photodetectors, and it needs relatively large nonlinearities. These should be available in the next-future technology, since recent theoretical [47] and experimental [48] developments indicate that huge Kerr phase shifts of the order of 0.1 radiant per photon can be obtained through electromagnetic induced transparency.

2.3.1 Experimental apparatus

The scheme, depicted in Fig. 2.11, is based on a ring cavity, coupled to the external radiation modes through two very low transmissivity τ beam splitters (BS) and a cross Kerr-medium. A tunable phase shifter, which shifts the field in the cavity by a phase ψ, is included in the device. One of the two cavity input modes (a_1) is pumped with a coherent source, while the other one (a_2) is left in the vacuum. Of the two output modes, one (b_2) is monitored with an ON-OFF photodetector D (which measures the presence or absence of the radiation field), the other one (b_1) is ignored. As will be shown in the following, whatever is the state of the input signal mode, a number state will be found at the output mode d_2 conditioned to a successful measurement at the detector D. By repeating the experiment, and measuring the relative frequency of successful photodetection, one recovers the amplitude of such a Fock component in the input state, and thus its photon number distribution. Upon fulfillment of certain conditions shown in the following, superpositions of number states can also be generated. In principle, the specific number state (or superposition) that will be created is controlled by tuning the phase ψ.

We now show how the device works by analyzing the dynamics of its components in the Heisenberg picture. In principle, it would be necessary to quantize the field in the cavity starting from its classical equations of motion, as for example in [49]. However, we show that the same results are more easily obtained with a simple one mode model of the cavity, by merely identifying the output mode c_2 at the beam splitter BS2 with the input mode c_3 at BS1 (see Fig. 2.11). Let $a_{1,2}$ denote the two input modes for the ring cavity, $b_{1,2}$ the two output modes, c_1 the cavity mode exiting BS1, c_2 the cavity mode exiting BS2, c_3 the cavity mode exiting the Kerr medium and the phase shifter, and d_1 and d_2 the input and output signal mode respectively. In the Heisenberg picture,

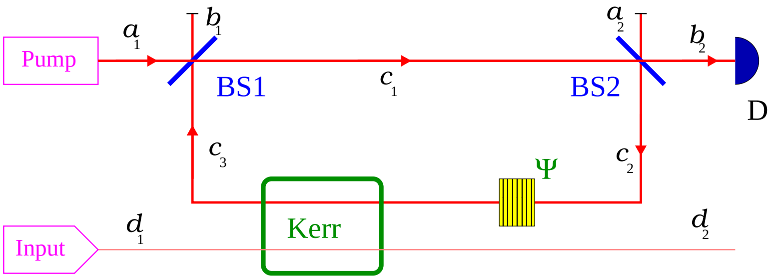

Figure 2.11: Sketch of the experimental setup for the measurement of the photon number distribution of unknown quantum states in mode d_1, using a coherent pump. The scheme is based on a conditional ON-OFF photodetector D, a non linear Cross–Kerr medium and a phase shifter ψ. The cavity input radiation modes are labelled a, the output modes b, the cavity modes c and the signal mode d. The quantum efficiency of the photodetector is not a crucial parameter, as it only affects the number of input states needed for the reconstruction and not its quality.

the input–output relations which characterize the components of the scheme are

$$\begin{aligned}
&\text{BS1: } \begin{cases} c_1 &= \sqrt{\tau}a_1 + \sqrt{1-\tau}c_3 \\ b_1 &= -\sqrt{1-\tau}a_1 + \sqrt{\tau}c_3 \end{cases} , \\
&\text{BS2: } \begin{cases} c_2 &= \sqrt{\tau}a_2 + \sqrt{1-\tau}c_1 \\ b_2 &= -\sqrt{1-\tau}a_2 + \sqrt{\tau}c_1 \end{cases} , \\
&\text{Kerr and Phase shift: } c_3 = c_2 \ \exp\left[-i(\chi t d_1^\dagger d_1 - \psi)\right] ,
\end{aligned} \tag{2.49}$$

where τ is the transmissivity of the two beam splitters, χt is the Kerr susceptibility times by the interaction time, and ψ is the phase shift imposed to the cavity field mode by the phase shifter. From Eqs. (2.49) the output modes $b_{1,2}$ of the cavity can be expressed as a function of the input cavity and signal mode as

$$\begin{cases} b_1 &= \kappa(\varphi)a_1 + e^{i\varphi}\sigma(\varphi)a_2 \\ b_2 &= \sigma(\varphi)a_1 + \kappa(\varphi)a_2 \end{cases} , \text{ with } \begin{cases} \kappa(\varphi) &\overset{\text{def}}{=} \frac{\sqrt{1-\tau}(e^{i\varphi}-1)}{1-(1-\tau)e^{i\varphi}} \\ \sigma(\varphi) &\overset{\text{def}}{=} \frac{\tau}{1-(1-\tau)e^{i\varphi}} \end{cases} , \tag{2.50}$$

where $\varphi \overset{\text{def}}{=} -\chi t d_1^\dagger d_1 + \psi$ is the overall phase shift due to the Kerr medium and the phase shifter. Notice that the coupling with the signal mode is contained in the dependence of φ on the signal input mode d_1.

From the Heisenberg evolution of the modes (2.50), one obtains the state $|\Psi_{out}\rangle$ in the cavity output modes (before the measurement) by using the creation operators $b_{1,2}^\dagger$ and by expressing the input state $|\Psi_{in}\rangle$ on a Fock basis of the input modes $a_{1,2}$:

$$|\Psi_{in}\rangle = \sum_{n,m=0}^{\infty} c_{nm} \frac{(a_1^\dagger)^n (a_2^\dagger)^m}{\sqrt{n!m!}} |0\rangle|0\rangle \longrightarrow |\Psi_{out}\rangle = \sum_{n,m=0}^{\infty} c_{nm} \frac{(b_1^\dagger)^n (b_2^\dagger)^m}{\sqrt{n!m!}} |0\rangle|0\rangle . \tag{2.51}$$

Consider the overall input state ϱ_{in} composed by a coherent state in mode a_1, vacuum in a_2 and arbitrary state in d_1 (which will be described by the density matrix $\nu_{ss'}$ in the Fock basis), *i.e.*

$$\varrho_{in} = |\alpha\rangle_{a_1 a_1}\langle\alpha| \otimes |0\rangle_{a_2 a_2}\langle 0| \otimes \sum_{s,s'=0}^{\infty} \nu_{ss'} |s\rangle_{d_1 d_1}\langle s'| \,. \tag{2.52}$$

Through Eq. (2.51) we obtain the output state (before detection by detector D) on the modes $b_{1,2}$ and d_2 as

$$\varrho_{bd} = |\alpha\kappa(\varphi)\rangle_{b_1 b_1}\langle\alpha\kappa(\varphi)| \otimes |\alpha e^{i\varphi}\sigma(\varphi)\rangle_{b_2 b_2}\langle\alpha e^{i\varphi}\sigma(\varphi)| \otimes \sum_{s,s'=0}^{\infty} \nu_{ss'}|s\rangle_{d_1 d_1}\langle s'| =$$

$$= \sum_{s,s'=0}^{\infty} \nu_{ss'} \times$$

$$|\alpha\kappa(\varphi_s)\rangle_{b_1 b_1}\langle\alpha\kappa(\varphi_{s'})| \otimes |\alpha e^{i\varphi}\sigma(\varphi_s)\rangle_{b_2 b_2}\langle\alpha e^{i\varphi}\sigma(\varphi_{s'})| \otimes |s\rangle_{d_2 d_2}\langle s'|, \tag{2.53}$$

where $\varphi_s \overset{\text{def}}{=} -\chi t s + \psi$, s in $\mathbb{N}$. After tracing out mode b_1, the state ϱ_{bd} becomes

$$\varrho'_{bd} = \textstyle\sum_{ss'} \quad \nu_{ss'} e^{-\frac{|\alpha|^2}{2}\left[|\kappa(\varphi_s)|^2 + |\kappa(\varphi_{s'})|^2 - 2\kappa(\varphi_s)\kappa^*(\varphi_{s'})\right]} \times \tag{2.54}$$
$$|\sigma(\varphi_s)\alpha e^{i\varphi}\rangle_{b_2 b_2}\langle\sigma(\varphi_{s'})\alpha e^{i\varphi}| \otimes |s\rangle_{d_2 d_2}\langle s'| \,,$$

The state (2.54) now undergoes a reduction at detector D. An ON-OFF photodetector, with quantum efficiency η is described by the two value probability operator measure (POM)

$$\Pi_{\mathsf{OFF}} = \sum_{k=0}^{\infty}(1-\eta)^k |k\rangle\langle k| \;;\; \Pi_{\mathsf{ON}} = 1 - \Pi_{\mathsf{OFF}} \,, \tag{2.55}$$

which is obtained from the Mandel-Kelley-Kleiner formula [38]. The final state after the reduction in mode b_2, in the case of a successful (ON) photodetection is given by

$$\varrho_{out} = \frac{\mathrm{Tr}_{b_2}[\Pi_{\mathsf{ON}}\varrho_{bd}]}{\mathrm{Tr}[\Pi_{\mathsf{ON}}\varrho_{bd}]} \tag{2.56}$$
$$= \frac{e^{-|\alpha|^2}}{\mathcal{N}} \sum_{s,s'=0}^{\infty} \nu_{ss'} \exp\left[|\alpha|^2 \left(\kappa(\varphi_s)\kappa^*(\varphi_{s'}) + \sigma(\varphi_s)\sigma^*(\varphi_{s'})e^{i(\varphi_s - \varphi_{s'})}\right)\right] \times$$
$$\left(1 - e^{-\eta|\alpha|^2\sigma(\varphi_s)\sigma^*(\varphi_{s'})}\right) |s\rangle\langle s'| \,,$$

where $\mathcal{N}$ is a normalization constant. Notice that the phase factors in the exponential in (2.56) do not play any role, as, in the working regime we exploit, these factors tend to one.

In the limit $\tau \to 0$, the effective transmissivity $\sigma(\varphi)$ of the cavity tends to a sum of Kronecker deltas

$$\lim_{\tau\to 0} |\sigma(\varphi_s)| = \left\{ \begin{array}{ll} 1 & \text{for } \varphi_s \overset{\text{def}}{=} -\chi t s + \psi = 2k\pi \quad (k \in \mathbb{Z}) \\ 0 & \text{for } \varphi_s \neq 2k\pi \end{array} \right. = \sum_{k=-\infty}^{\infty} \delta_{s,kl^* + n^*} \,, \tag{2.57}$$

where $l^* = \frac{2\pi}{\chi t}$ is the distance between the peaks, and $n^* = \frac{\psi}{\chi t}$ is the position of the first peak. For the values of l^* and n^* for which the quantity $kl^* + n^*$ is not an integer, there is no contribution to the sum in (2.57). In fig. 2.12 the function $|\sigma(\varphi_s)\sigma^*(\varphi'_s)|$ is plotted *vs.* φ_s and φ'_s.

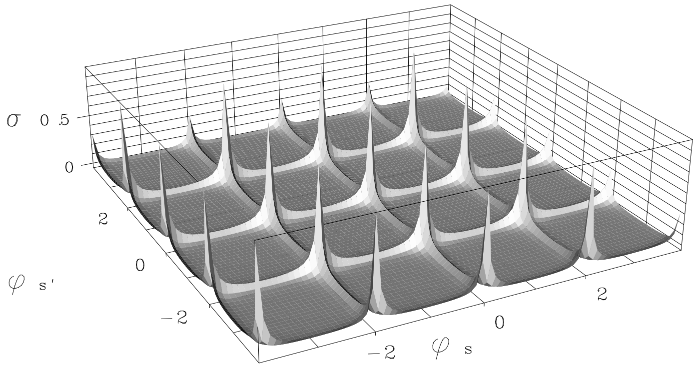

Figure 2.12: Plot of the function $|\sigma(\varphi_s)\sigma^*(\varphi'_s)|$ [φ_s, $\varphi_{s'}$ in π units.], with $\tau = .1$, $n^* = \frac{\psi}{\chi t} = 0$ and $l^* = \frac{2\pi}{\chi t} = 2$. Notice the "fakir chair" structure: the function approaches a sum of delta functions for beam splitter transmissivity $\tau \to 0$.

From Eqs. (2.56) and (2.57) it is clear that for small values of the Kerr susceptibility χt (*i.e.* l^* high enough so that $\nu_{il^*+n^*,jl^*+n^*} \simeq 0$ for both i and j nonzero) and for high pump value $|\alpha| \gg 1$, the output state approaches a Fock state:

$$\lim_{\tau \to 0} \varrho_{out} = |n^*\rangle\langle n^*| \, . \tag{2.58}$$

Notice that the state $|n^*\rangle$ to be synthesized can be controlled by varying the phase ψ. In Fig. 2.13 the photon number distribution of the state (2.56), is given. Notice how the limiting case of Eq. (2.58) is approached.

In order to recover the photon number distribution $p(n)$, the phase ψ must be scanned in order to put the cavity into resonance with the Fock states $|0\rangle$, $|1\rangle$, $\cdots$, $|m\rangle$, up to a certain state m that we assume is the highest excited Fock component of the input state. For each of the values that ψ takes, the measurement procedure described above must be repeated a number N times. The relative frequency of successful photodetection when ψ is tuned on the state $|n\rangle$ gives the probability $p(n)$. In fact, the probability of successful (ON) detection is given by

$$P_{\mathsf{ON}} = \mathrm{Tr}[\Pi_{\mathsf{ON}}\rho_{bd}] = \sum_{k=0}^{\infty} \nu_{kk}(1 - e^{-\eta|\alpha|^2|\sigma(\varphi_s)|^2}) \, , \tag{2.59}$$

and for sufficiently high l^* and $|\alpha| \gg 1$, is proportional to one of the diagonal elements of the input density matrix $P_{\mathsf{ON}} \simeq \nu_{n^*n^*}$. Thus, if an ensemble of identical states is

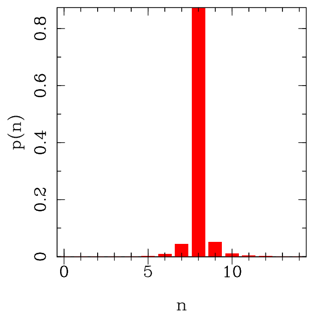

Figure 2.13: Plot of photon number distribution of a synthesized Fock state. The experimental parameters are: $\tau = 0.01$, $\psi = .4$, $\chi t = 0.05$, $\eta = 10\%$ and the two pumps (in modes a_1 and d_1) are in a coherent state with amplitude $\alpha = \beta = 3$. The output state approaches a Fock state $|8\rangle$.

impinged into the device in mode d_1, by tuning the cavity to different values of n^* and measuring the relative frequency of ON photodetections, one can obtain $\nu_{n^*n^*}$. This allows the measurement of the photon number distribution of an arbitrary state, using less experimental data and lower quantum efficiency detectors than in homodyne tomography (which is the currently used experimental procedure for reconstructing the number distribution of arbitrary states). One must be aware however, that the above procedure must be modified in the case of non-ideal photodetection ($\eta < 100\%$), since in this case a better normalization proceeding has to be applied. In fact, $p(n)$ must be evaluated by dividing the number of successful photodetections (when ψ is tuned to $|n\rangle$) by the total number of successful photodetections, for any ψ. Caution must be taken in order to avoid introducing systematic errors: one must be confident that the ψ–scanning on the Fock components $|n\rangle$ is carried out on a range wide enough to cover all Fock components that are excited in the input state. Moreover, we must assume that the statistics of the outcomes does not change, when varying ψ. This last assumption can be dropped by using a chain of Fock filters, the output signal mode of each impinging in the input of the successive, where each one is tuned to a different Fock component, as in Fig. 2.14.

A couple of Monte Carlo simulations for the measurement procedure here given are shown in Fig. 2.15. A minor modification of this same experimental setup allows to reconstruct also the truncated density matrix of the state in the Fock basis. As shown in Ref. [19], the displaced Fock-state probability distribution $p_n(\zeta) = \langle n,\zeta|\varrho|n,\zeta\rangle$, with $|n,\zeta\rangle = e^{\zeta a^\dagger - \zeta^* a}|n\rangle$, can be used to reconstruct the density matrix ϱ by means of a least-squares inversion method. The displacement parameter ζ can be kept constant in modulus, varying only the phase of the local oscillator that realizes the displacement on

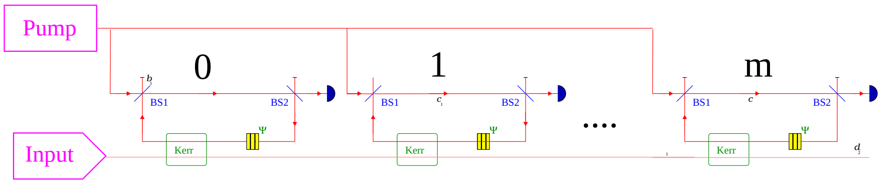

Figure 2.14: Chain of Fock filters that allow to recover the photon number distribution using much less data than the data necessary if using a single cavity. The number of cavities must be equal to the maximum m that is to be measured.

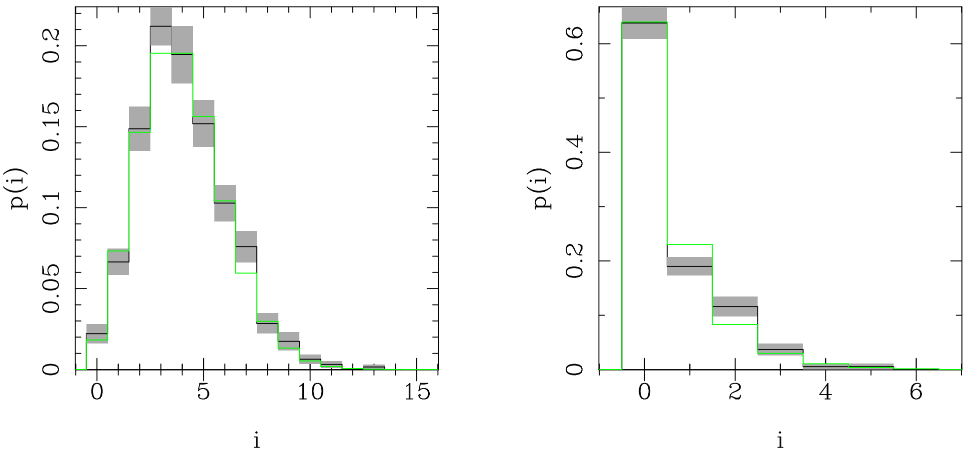

Figure 2.15: Monte Carlo simulation of two photon number measurements using the chain of Fock filters depicted in Fig. 2.14. The parameters for these simulations are: detector quantum efficiency $\eta = 10\%$; beam splitter transmissivity $\tau = 10^{-3}$; Kerr non linearity $\chi t = 10^{-2}$; coherent pump state intensity $|\alpha|^2 = 10$. The state on the left is a coherent state (in the Fock basis: $|\beta\rangle = e^{-(1/2)|\beta|^2} \sum_i \frac{1}{\sqrt{i!}} \beta^i |i\rangle$), with $\beta = 2$. It has been reconstructed with 1000 measurements, divided into 20 statistical blocks, by a chain of 15 Fock filters. The state on the right is a thermal state (in the Fock basis: $|\gamma\rangle = \sqrt{1 - |\gamma|^2} \sum_i \gamma^i |i\rangle$), with $\gamma = 0.6$. Here only 300 measurements, divided into 10 statistical, blocks have been used. A chain of 6 detectors is sufficient. The theoretical distributions have been superimposed to the histograms.

the signal ϱ through a high-transmissivity beam splitter. The distributions $p_n(|\zeta|e^{i\varphi})$ at different phases φ can then be measured with the ring cavity method described above. In Fig. 2.16 we report the result for the reconstruction of a squeezed vacuum state with average photon number $\langle a^\dagger a\rangle = 0.5$ together with the corresponding statistical errors. Notice that the reconstruction of the whole density matrix has been carried out using quantum efficiency as low as $\eta = 20\%$.

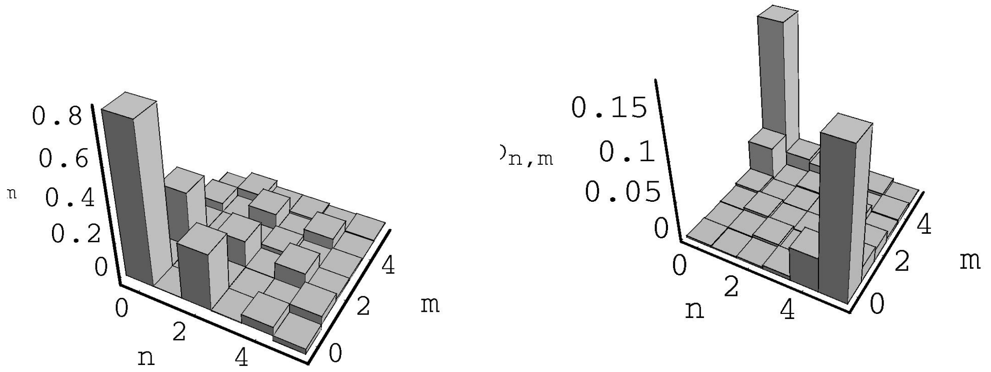

Figure 2.16: Monte Carlo simulation of the reconstruction of a squeezed vacuum state with $\langle a^\dagger a \rangle = 0.5$ average photons. On the left: the real part of the matrix elements. On the right: the corresponding statistical errors. The ring-cavity method has been used to measure the displaced photon number distributions $p_n(\zeta)$, with $|\zeta| = 1.4$ and 25 equally spaced phases $\varphi = \arg \zeta \in [0, 2\pi)$ with 4000 data each. 10 blocks have been used to evaluate the statistical errors. The parameters of the set-up are the following: quantum efficiency $\eta = 20\%$, beam-splitter transmissivity $\tau = 10^{-4}$, Kerr coupling $\chi t = 10^{-1}$.

2.3.2 Other applications

Superposition generation. In order to produce superpositions of selected equally spaced number states, one has to provide higher values for the Kerr nonlinearity χt, or alternatively to provide sufficiently excited input state in mode d_1, so that the input state coefficients $\nu_{il^*+n^*,jl^*+n^*}$ are different from zero for different values of i and j. For example, as shown in Figs. 2.17 and 2.18, starting from a coherent input state with density matrix $\nu_{ss'} = e^{-|\beta|^2} \frac{\beta^s (\beta^*)^{s'}}{\sqrt{s! s'!}}$ it is possible to generate the superposition

$$|\Psi\rangle = \frac{1}{\sqrt{2}} (|n^*\rangle + e^{i\Phi} |n^* + l^*\rangle) \tag{2.60}$$

by choosing $|\beta|^2 = \sqrt[l^*]{\frac{(n^*-l^*)!}{n^*!}}$ and $\arg \beta = \frac{\Phi}{l^*}$. It must be stressed that only superposi-

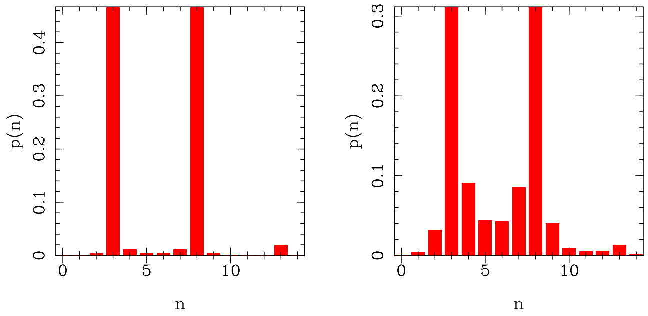

Figure 2.17: Plot of the diagonal of the density matrix ϱ_{out} exiting the device for a coherent input in mode d_1 with modulus $|\beta|^2 = \sqrt[5]{\frac{8!}{3!}}$ and with $l^* = 5$, $n^* = 3$. The parameters are chosen so to have the superposition $\frac{1}{\sqrt{2}}(|3\rangle + |8\rangle)$ in the Fock basis. In the left plot, notice a residual component at the Fock state 13, which results from the term $k = 2$ in the sum (2.57). Here, the quantum efficiency of detector D is $\eta = 10\%$, the modulus of the cavity pump is $\alpha = 8$, the BS transmissivity is $\tau = .06$. In the right plot we used $\tau = .2$, to show the smearing effect of a bad cavity.

tions of the type

$$|\Psi\rangle = \sum_{k=0}^{\infty} c_k |n^* + kl^*\rangle \tag{2.61}$$

may be created, where the coefficients c_k are determined by the state incoming in mode d_1, *i.e.* by the coefficients $\nu_{ss'}$.

Entanglement creation. A modified version of the proposed experiment may also be used for the production of two-mode entangled states. One only has to use two Kerr crystals inside the cavity, as shown in Fig. 2.19. In this case, the total phase shift imposed by the cavity is given by the sum of the effect of each Kerr medium. For identical Kerr crystals $K1$ and $K2$ (*i.e.* $\chi_{K1} \equiv \chi_{K2} \overset{\text{def}}{=} \chi$), one has $l^* = \frac{\pi}{\chi t}$ and $n^* = \frac{\psi}{2\chi t} = n_1^* + n_2^*$, where n_1^* and n_2^* are the eigenvalues of the number states in the modes $d^{(1)}$ and $d^{(2)}$ impinging into each of the Kerr crystals. In this case, Eq. (2.57) becomes

$$\lim_{\tau \to 0} |\sigma(\varphi_s)| = \sum_k \delta_{s,kl^*+n_1^*+n_2^*} \ , \tag{2.62}$$

and the output state (2.58) for $\tau \ll 1$ and $|\alpha| \gg 1$ now reads

$$\varrho_{out} = \sum_{n,k=0}^{n^*} \nu_{nk}^{(1)} \nu_{nk}^{(2)} |n\rangle_{d_2^{(1)}\, d_2^{(1)}}\langle k| \otimes |n^* - n\rangle_{d_2^{(2)}\, d_2^{(2)}}\langle n^* - k| \ , \tag{2.63}$$

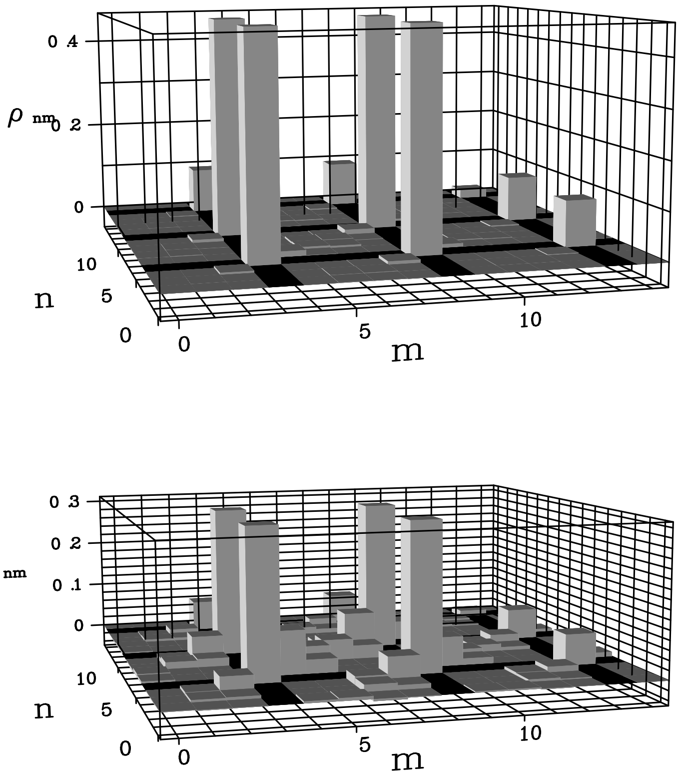

Figure 2.18: Density matrix for the two states given in Fig. 2.17.

that is obtained in the limit of low Kerr nonlinearity $\chi t \ll 1$ (*i.e.* $l^* \gg 1$). For input signal pure states $|\Psi_{in}\rangle = \sum_k \nu_k^{(1)} |k\rangle_{d_1^{(1)}} \otimes \sum_j \nu_j^{(2)} |j\rangle_{d_1^{(2)}}$, one finds

$$|\Psi_{out}\rangle = \sum_{k=0}^{n^*} \nu_k^{(1)} \nu_{n^*-k}^{(2)} |k\rangle_{d_2^{(1)}} |n^* - k\rangle_{d_2^{(2)}} \ . \tag{2.64}$$

It is obvious that any multipartite entanglement between many modes could be synthesized in principle, by increasing the number of Kerr media in the cavity. This method could then be used also to generate Greenberger–Horn–Zeilinger states.

2.3.3 Feasibility

We now analyze the feasibility of the proposed experimental scheme. In Subsect. 2.3.1 we already analyzed the effect of limited detector efficiency $\eta < 100\%$ for the photon distribution measurement scheme. Regarding the effect of detector's D quantum efficiency when the device is used as a Fock state generator, as can be seen from Fig. 2.20, when one lowers the detector's quantum efficiency, the result is actually a purification

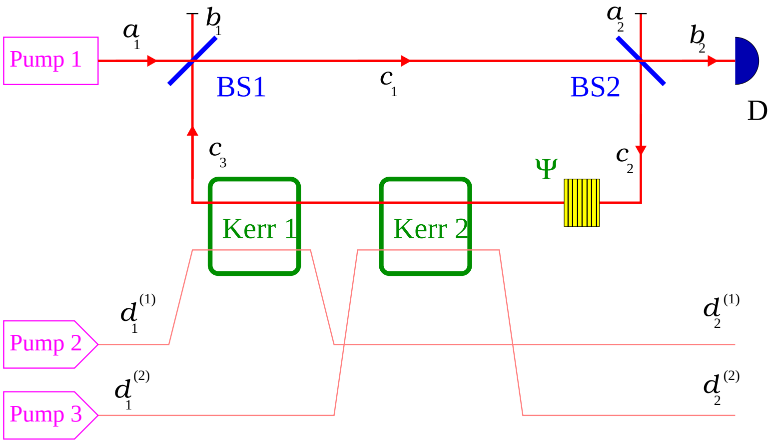

Figure 2.19: Modification of the proposed experimental setup, in order to construct entangled states between the output modes $d_2^{(1)}$ and $d_2^{(2)}$.

of the state. Qualitatively this can be explained by noticing that in Eq. (2.56) the lowering of η contributes to the convergence exploited in Eq. (2.58) to produce the Fock state (or the superpositions). It would seem that one could actually increase the output signal quality by using low efficiency photodetectors. The drawback is given in terms of production rate of the desired Fock states. It is obvious that it is less probable for a non–efficient photodetector to click, so the production rate is drastically decreased. This is also the reason for which, in the case of inefficient detector D, the probability is not the relative frequency of successful photodetections, but it must be normalized on the number of successful photodetections for all values of ψ, as described in Subsect. 2.3.1. In fact, the probability of a successful ON photodetection is given by Eq. (2.59), from which one can see that P_{ON} exponentially decreases with decreasing η, and which for $\tau \to 0$ and $|\alpha| \gg 1$ tends to

$$P_{\text{ON}} \longrightarrow \sum_{k=0}^{\infty} \nu_{kl^*+n^*,kl^*+n^*} \ . \tag{2.65}$$

The quantum efficiency η of the detector in the proposed device is, therefore, not a critical parameter, so that ordinary photodetectors may be used in the experimental setup. Using low efficiency photodetection does not reduce the quality of the output states, but only it affects their production rate.

The actual feasibility of the proposed experimental setup relies on the availability of good ring cavities, suitable Kerr nonlinearities, and ordinary photodetection. The cavity couples to the outside modes through small transmissivity beam splitters $\tau \simeq 0.1 \div 0.01\%$. The Kerr nonlinearities that are needed are of the order of $\chi t \simeq 0.01$ for the creation of number states and of the order of $\chi t \simeq 0.1$ for obtaining superpo-

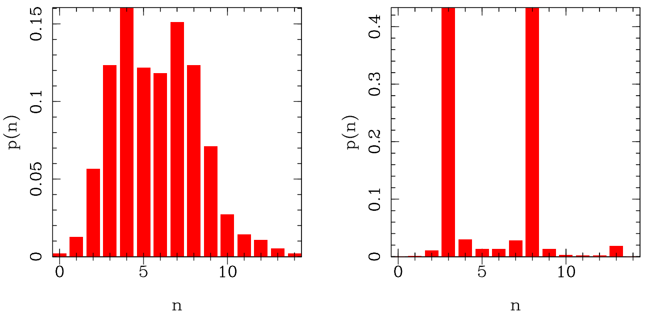

Figure 2.20: Plots for the same parameters as for the right figure 2.17 (*i.e.* $|\beta|^2 = \sqrt[5]{\frac{8!}{3!}}$, $l^* = 5$, $n^* = 3$, $\alpha = 8$ and $\tau = .2$). On the left $\eta = 100\%$, while on the right $\eta = 1\%$. This shows how lowering the detector's quantum efficiency enhances the quality of the state. The cost is paid in terms of a lower production rate: the probability (2.59) of obtaining the state depicted on the left is $P_{\mathsf{ON}} \simeq 0.789$, while on the right $P_{\mathsf{ON}} \simeq 0.106$.

sitions. Photodetection with quantum efficiency as low as $\eta = 1\%$ has been shown to be effective. The output state must be controlled by varying the phase shift ψ which can be varied, in ordinary experimental setups, in steps of the order of $\frac{\pi}{500}$ [50]. To our knowledge, the experiment for the generation of Fock states or two mode entangled states should be feasible with laboratory technology now available. The creation of Fock state superposition may ask for Kerr nonlinearities which are not yet available in the optical domain, though recent results [47, 48] indicate that giant non-linear shifts of the order of 0.1 radiant per photon may be obtained through electromagnetically induced transparency.

2.3.4 Conclusions

In conclusion we have proposed an optical device capable of measuring the photon number probability of unknown quantum states and of creating optical Fock states, selected superposition of Fock states, and two mode entangled states in traveling wave modes. The experimental setup is composed of a high-Q ring cavity coupled with the signal mode through a cross-Kerr medium and an ON-OFF photodetection. A successful photodetection reduces the signal mode to a predetermined output state. We have shown that imperfect photodetection does not affect the quality of the output states. By counting the number of successful photodetections when the cavity is set into resonance with the Fock components of the input state, one may recover the input state photon number probability. Compared to conventional homodyne tomography (the only efficient known method for the photon distribution measurement), this scheme allows the same measurement with less data and with detectors far less efficient, as is evident from the Monte Carlo simulations that were shown in this section. The applications for such a device in the modern “Quantum technology” are numerous and span through many of the fields of advanced quantum optics research.

Chapter 3

Homodyne tomography: proposed experiments

3.1 Introduction

Optical homodyne tomography, which has been derived in Sect. 2.1 from the general formulas of Sect. 1.2, allows numerous experiments. In this chapter a number of such experiments, which I contributed to propose, are outlined. Each of these are not "brute force" applications of the theory previously outlined, but the homodyne tomography technique has to be appropriately modified so to adapt to the particular experimental setups and to obtain the results we need. Monte Carlo simulations will be used to illustrate the feasibility of the proposed experimental setups. Here a brief outline of the chapter is given.

In Sect. 3.2 (see [46]) we propose a setup for obtaining the Hamiltonian operator (for unitary devices) or the Liouvillian superoperator (for devices interacting with the environment) of an arbitrary phase-insensitive optical device. This, obviously, allows a complete characterization of the device, at least in the optical domain that is explored. In Sect. 3.3 (see [51]) an experiment for the generation and detection of optical Schrödinger cats is proposed. The experimental setup is based on the one proposed in [52], which would not be feasible with the technology now available. Our proposal, which in addition to homodyne tomography uses a novel deconvolution procedure, makes it possible to reconstruct cat states that are produced with heavy noise from inefficient photodetectors. Homodyne tomography can also be used in fundamental tests of quantum theory, such as the test of the state reduction mechanism I describe in Sect. 3.4, or the test of Bell's inequalities, which I describe in Sect. 3.5. For the state reduction test, (see [53]), one can take advantage of the fact that in the optical domain a multitude of completely different detection schemes (direct detection, heterodyne detection, homodyne detection) are available. We compare the "experimental" state reduced from each of such measurement schemes with the state we would expect theoretically from the reduction postulate. Regarding the tomographic test of Bell's inequalities (see [54]), the tomographic setup is here modified into a "self homodyne" scheme in order to obtain a Bell experiment based on the spatially correlated photon state which may be obtained through parametric down conversion. In Sect. 3.6 a feasibility study is presented for the analysis of the experimental data for an homodyne measurement which is being presently carried out in Prof. De Martini's group in Roma University.

In conclusion, in this chapter a series of practical applications of the theory of the optical homodyne tomography technique presented in Chap. 1 will be described in the form of proposals for experimental setups. In all cases some numerical computer simulations will be given to illustrate the proposals and to show their actual feasibility.

3.2 Hamiltonian reconstruction

In this section we show [46, 55, 56] how optical homodyne tomography, described in Sect. 2.1, can be used to determine the Hamiltonian of an optical phase-insensitive device that evolves the quantum state of radiation. In the case of non–unitary device (as is the case for open quantum systems, *i.e.* systems interacting with an environment reservoir) the Liouvillian superoperator that evolves the density matrix of the radiation is obtained. Previous theoretical proposals to give a complete characterization of quantum processes have been made in Refs. [57]. There, the methods are restricted to systems with finite dimensional Hilbert space, and the method does not lead to an explicit reconstruction of the Liouvillian. In this section we show how this goal can be achieved in practice, by presenting a simple experimental setup that measures the Liouvillian of a phase-insensitive optical device.

3.2.1 Experimental setup

The main idea for reconstructing the Liouvillian of a quantum device is sketched in Fig. 3.1. One should impinge the device with a known input state ρ_{in} from an (over)complete set, determine the state ρ_{out} at the output, and finally compare ρ_{in} to ρ_{out}. For an optical device the determination of the output state is made possible by the homodyne tomography technique. Regarding the generation of the set of input states $\{\rho_{in}\}$, an experimental method is suggested later in this section. The evolution of the state from ρ_{in} to ρ_{out} is governed by the Green (super)operator $\mathcal{G}$

$$\rho_{out} = \mathcal{G}\rho_{in} \ , \tag{3.1}$$

where $\mathcal{G}$ has actually a four-index matrix representation, and on the Fock basis $\{|n\rangle\}$ one has $\langle n|\rho_{out}|m\rangle = \sum_{h,k=0}^{\infty} G_{nm}^{hk}\langle h|\rho_{in}|k\rangle$. For a device that is homogeneous along the

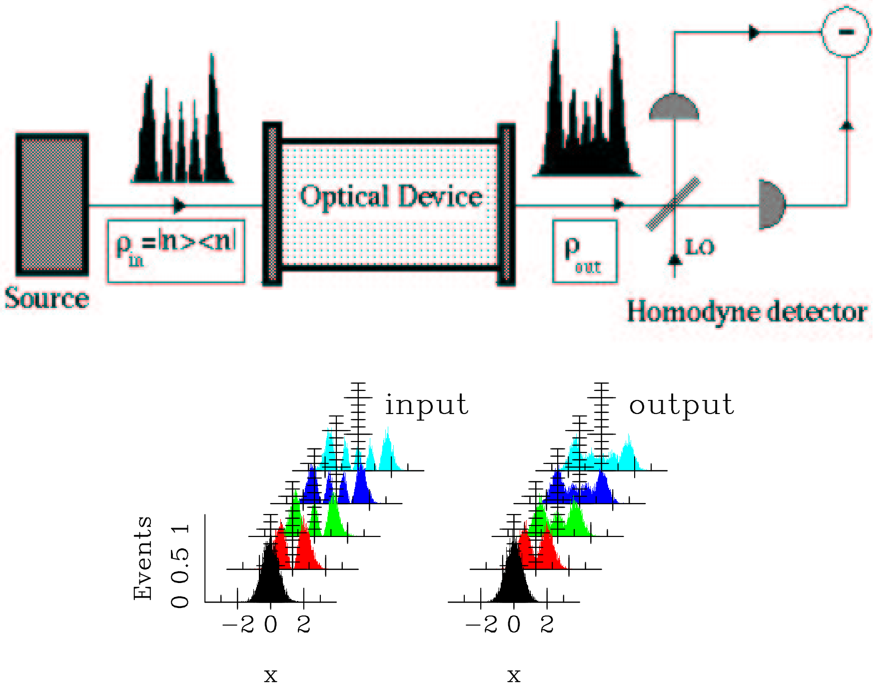

Figure 3.1: Sketch of the method for measuring the Liouvillian of an optical device. A known input state ρ_{in} is impinged into the device, and quantum tomography of the output state is performed using a homodyne detector. By scanning an (over)complete set of states ρ_{in} at the input and comparing them with their respective output states, it is possible to reconstruct the Liouvillian of the device. The histograms of homodyne data, here given for the sake of illustration, correspond to a device that consists of an empty cavity, and with the input states as number states $\rho_{in} = |n\rangle\langle n|$.

direction of light propagation the Green superoperator can be written as the exponential of a constant Liouville superoperator $\mathcal{L}$ as follows

$$\mathcal{G} = \exp(\mathcal{L}\tau) \; , \tag{3.2}$$

where τ is the propagation time (*i.e.* the device length). The Liouvillian $\mathcal{L}$ gives the evolution of the state through an infinitesimal slab of the device media according to the master equation $\dot{\rho} = \mathcal{L}\rho$. We restrict our attention to the case of a perfectly phase-insensitive device: as it will be clear from the following, the case of phase-sensitive device is much more complicated. A phase-insensitive device is a device that leaves dephased states as dephased, as in the case of a traveling wave laser amplifier. A dephased state is diagonal in the photon-number representation, with density matrix of the form $\rho = \sum_{n=0}^{\infty} r_n \, |n\rangle\langle n|$, where $\{|n\rangle\}$ denotes the complete set of eigenvectors of the photon-number operator $a^\dagger a$ of the field mode with annihilation operator a. For the evolution of dephased states it is sufficient to determine the sector of the Green superoperator that evolves dephased states, *i.e.* the two-index Fock matrix

$$G_{nm} = \langle n|\, \mathcal{G}\Big[\, |m\rangle\langle m| \,\Big]\, |n\rangle \; . \tag{3.3}$$

The Liouvillian L_{nm} is then obtained as the matrix-logarithm of G_{nm} [58, 59].

The experimental reconstruction of L_{nm} could be performed by impinging a number state $\rho_{in} = |n\rangle\langle n|$ on the device, and then making the homodyne tomography of the output state. In this fashion, the number probability distribution $r_k(n)$ of the output coincides with the n-th row of the Green matrix G_{nm}, and by varying n one would reconstruct the whole matrix. Since producing number states is experimentally difficult, one would try to use coherent states instead. In this way matrix elements of the form $\langle\psi|\, \mathcal{G}[\, |\alpha\rangle\langle\alpha|\,]\, |\psi'\rangle$ would be obtained, with $|\alpha\rangle$ denoting the scanning coherent input state, and $|\psi\rangle$ and $|\psi'\rangle$ being a couple of vectors of the tomographically reconstructed matrix representation. Unfortunately, the relation between G_{nm} and $\langle n|\, \mathcal{G}[\, |\alpha\rangle\langle\alpha|\,]\, |n\rangle$ is highly singular, involving the P-function of $|m\rangle\langle m|$, and hence the matrix G_{nm} cannot be obtained in this way starting from experimental data, which is always affected by statistical errors. On the other hand, the Fock representation has a privileged role, because here the Liouvillian matrix has a transparent meaning in terms of creation and annihilation operators. How to overcome the problem of generating input Fock number-states? A solution could be to employ the "optical Fock filter", which was described in Sect. 2.3 and is capable of producing Fock states and some selected superposition of Fock states. This apparatus, though, is experimentally rather challenging, and the analysis of the imperfections in the produced states is *a priori* difficult. On the other hand, the Fock filter may become useful for the analysis of phase–sensitive devices since it is the only apparatus, to my knowledge, capable of producing the selected superpositions of Fock states one would need for the characterization of such devices. However, through the Fock filter only some portions of the Green superoperator may be accessible, since it is not capable of producing all the necessary superpositions — such as *e.g.* $\frac{1}{\sqrt{2}}(|n\rangle + |n+1\rangle)$ with arbitrary n. Moreover, the extension of the theory presented in this section to the experimental characterization of phase–sensitive devices is also complicated by the non–trivial issue of numerically calculating the logarithm of a four index matrix.

In the following we will use a much simpler apparatus, which can produce the desired input states and whose imperfections can be taken into account so that the errors that it introduces can be deconvolved. In fact, for the purpose of analyzing phase–insensitive devices, it is sufficient to generate number states with random n as far as n is known. This leads us to devise the setup depicted in Fig. 3.2. A non degenerate optical parametric amplifier (NOPA) with a strong classical pump down-converts the vacuum into a pair of twin beams. The twin beams are used as a random-n

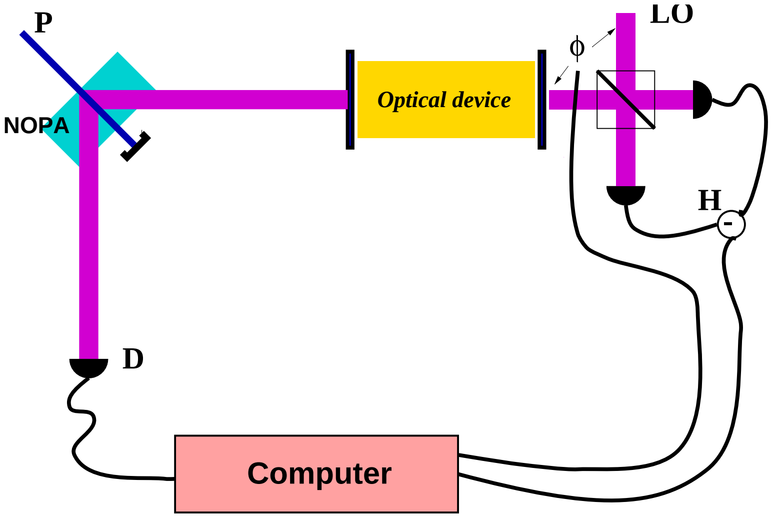

Figure 3.2: Experimental setup, including the apparatus used to generate the input number states $\rho_{in} = |n\rangle\langle n|$ needed for the tomographical reconstruction of the Liouvillian of an optical device. A random-n Fock state $|n\rangle$ for the input beam is achieved by performing photodetection at D on the other twin beam, n being the measured number of photons. A non degenerate optical parametric amplifier (NOPA) with vacuum input is used to produce the twin beams. For non 100% quantum efficiency photodetection at D, an error compensating procedure is proposed —see Eq. (3.6).

Fock state generator by measuring the number of photons on one beam (detector D in Fig. 3.2) while impinging the other beam on the optical device. For quantum efficiency $\eta_D = 100\%$ at detector D, the photodetection would reduce the twin-beam state $|\mathrm{TB}\rangle \propto \sum_{n=0}^{\infty} \xi^n |n, n\rangle$ into a random-n state $|n\rangle$ at the input of the optical device, with thermal probability distribution $w_n = |\xi|^{2n}\left(1 - |\xi|^2\right)$, where n is the measurement outcome at D. The tomographically reconstructed number probability $\langle k|\ \mathcal{G}[\,|n\rangle\langle n|\,]\ |k\rangle$ of the output state already would provide the nth row G_{kn} of the Green matrix. On the other hand, for $\eta_D < 1$, a mixed state ρ_n will actually enter the device instead of $|n\rangle\langle n|$, as a result of the state reduction at D (we already remembered in Sects. 2.1 and 2.3 that an inefficient photodetector is equivalent to a perfect detector preceded by a beam splitter). The outcome n probability distribution then becomes

$$p_n = (1 - |\xi|^2)\frac{(\eta_D|\xi|^2)^n}{[(\eta_D - 1)|\xi|^2 + 1]^{n+1}}\ , \tag{3.4}$$

as will be consistently derived in Sect. 3.6. One can easily show that the tomographically reconstructed output number probability $r_k(n) \equiv \langle k|\mathcal{G}[\rho_n]|k\rangle$ is related to the

Green matrix through the identity

$$r_k(n) \;=\; [(\eta_D-1)|\xi|^2+1]^{n+1}\sum_{m=0}^{\infty}\binom{m+n}{n}[|\xi|^2(1-\eta_D)]^m G_{k,m+n}\;. \qquad (3.5)$$

The relation (3.5) can be inverted as follows

$$G_{kl} \;=\; \frac{1}{[(\eta_D-1)|\xi|^2+1]^{l+1}}\sum_{n=0}^{\infty}\binom{n+l}{l}\left[\frac{(\eta_D-1)|\xi|^2}{(\eta_D-1)|\xi|^2+1}\right]^n r_k(n+l)\;. \qquad (3.6)$$

In fact, consider the Bernoulli series

$$f_n=\sum_{j=0}^{\infty}\binom{n+j}{n}\eta^n(1-\eta)^j\,g_{n+j}\;, \qquad (3.7)$$

where η is a parameter and f_n and g_n are arbitrary operators. We can prove that the following inversion

$$g_n=\sum_{k=0}^{\infty}\binom{n+k}{n}\eta^{-n}\left(1-\frac{1}{\eta}\right)^k f_{n+k} \qquad (3.8)$$

holds in any case, apart considerations of convergence of (3.8) depending on the nature of f_n and of g_k. By substituting Eq. (3.7) into Eq. (3.8) one obtains

$$\begin{aligned}
&\sum_{k=0}^{\infty}\binom{n+k}{n}\eta^{-n}(1-\frac{1}{\eta})^k\sum_{j=0}^{\infty}\binom{n+k+j}{n+k}\eta^{n+k}(1-\eta)^j g_{n+j+k}\\
&=\;\sum_{k=0}^{\infty}\sum_{j=k}^{\infty}\binom{n+k}{n}\binom{n+j}{n+k}(\eta-1)^k(1-\eta)^{j-k}g_{n+j}\\
&=\;\sum_{j=0}^{\infty}\sum_{k=0}^{j}\binom{n+k}{n}\binom{n+j}{n+k}(\eta-1)^k(1-\eta)^{j-k}g_{n+j}\\
&=\;\sum_{j=0}^{\infty}\sum_{k=0}^{j}\binom{n+j}{n}\binom{j}{k}(-1)^k(1-\eta)^j g_{n+j}\\
&=\;\sum_{j=0}^{\infty}\binom{n+j}{n}\delta_{j0}(1-\eta)^j g_{n+j}=g_n\;, \qquad (3.9)
\end{aligned}$$

where the formula $\sum_{k=0}^{j}\binom{j}{k}(-1)^k=\delta_{j0}$ has been used. Notice that this inversion method is completely general and can be used for the reconstruction of any set of states g_n conditioned by an inefficient photodetection which produces the mixed states f_n. In fact, a similar deconvolution procedure will be also used in Sects. 3.3 and 3.6 for the reconstruction of Schrödinger cat states and for the measurement of twin beam states respectively.

Eq. (3.6) is our algorithm to reconstruct the Green matrix G_{kl} from the collection of all tomographically measured number probabilities $r_k(n)$ for different outcomes n (in practice the sum in Eq. (3.6) is truncated at some maximum n). Notice the interplay of the gain ξ and the quantum efficiency η_D in determining the probability p_n on one hand, and in producing the statistical errors in the reconstructed Green matrix on the other hand. For decreasing quantum efficiency $\eta_D \to 0$, larger values of n can be made more probable by increasing the gain of the NOPA as $\xi \to 1^-$. However, at the same time, convergence of the sum in Eq. (3.6) becomes slower, and statistical errors of matrix elements G_{kl} increase as result of tomographic errors on $r_k(n)$. Hence, the effect of quantum efficiency η_D, which reduces the size of the viewable matrix G_{kl}, can be partially compensated by increasing the gain of the NOPA, however at expense of statistical errors for G_{kl}. For the tomographic measurement, by increasing the number of experimental data and using η_H-dependent pattern functions, introduced in Sect. 1.1.3 as Eqs. (1.19) and (1.20), can compensate the effect of low quantum efficiency $\eta_H < 1$, which, anyhow, must be above the threshold $\eta_H = 50\%$ (for the reconstruction in the Fock basis). On the other hand, for quantum efficiency η_D at detector D there is not such a threshold, as one can see from the convergence and error-propagation analysis of Eq. (3.6), which will be carried out in Sect. 3.6.

The proposed state-reduction scheme—based on twin beams from a NOPA—is not a new one, and, for example, a similar setup has been proposed to generate Schrödinger-cat states with the experimental setup which will be described in Sect. 3.3. As such state-reduction is the core of our measurement method, we want to examine it at work in a realistic situation[1]. Typically the NOPA can be pumped by the second harmonic of a Q-switched mode-locked Nd:YAG laser, with the output twin beams pulsed at a repetition rate of 80 MHz, and with a 7ps pulse duration. Thus, the twin beam mode with annihilator a at the input of the optical device is actually a wideband mode, with frequency centered around 532nm, and width of 140 GHz (the inverse of the pulse time-length). The same Nd:YAG laser beam is used for the local oscillator (LO) of the homodyne detector H. In this way the LO has the same central frequency and the same time-envelope of the beam at the input of the optical device. The integration time at photodetector D can be set to 1 ns, which is greater than the pulse width and shorter than the distance between pulses. In this way each pulse is completely annihilated by the detector D during the integration time, and, correspondingly, the homodyne measurement is made with the LO matched on the same pulse shape of the signal twin beam, which means that the measurement is performed on the right wideband mode after reduction by detector D. Moreover, the detector D and the optical device can be geometrically placed in such a way that, within a narrow solid angle, the direction of

---

[1] We acknowledge useful discussions with Prof. Tito Arecchi of INO, Firenze, on the experimental setup.

the respective input k-vectors are the same relative to the k-vector of the NOPA pump, so that state reduction at D affects only radiation at the twin k at the input of the device, so that the state-reduced modes at D and at the device are perfectly matched. From the above scenario it follows that the mode with annihilator a at the input of the optical device is actually a wideband mode, and hence we measure the effective Liouvillian over a 140 GHz bandwidth centered around 532nm. Then, it is clear that all measurements for different random inputs can be considered as independent only if the (atomic) relaxation times in the optical devices are shorter than the pulse-repetition period.

3.2.2 Examples of reconstructions

Now we show the results from some Monte-Carlo simulated experiments to see our method at work, and estimate the number of measurements needed and the reliability of the reconstruction of G_{kl}.

The simplest phase insensitive device is the phase-insensitive linear amplifier (PIA), with Liouvillian $\mathcal{L}$

$$\mathcal{L} = 2\Big\{A\mathcal{D}[a^\dagger] + B\mathcal{D}[a]\Big\} \ , \tag{3.10}$$

where the Lindblad superoperator is defined as

$$\mathcal{D}[\theta]\rho \overset{\text{def}}{=} \theta\rho\theta^\dagger - 1/2(\theta^\dagger\theta\rho + \rho\theta^\dagger\theta) \tag{3.11}$$

for any complex operator θ. For $A = 0$, Eq. (3.10) describes an empty cavity. The Liouvillian matrix has the form

$$\begin{aligned} L_{nm} &\overset{\text{def}}{=} \langle n|\mathcal{L}\Big[|m\rangle\langle m|\Big]|n\rangle = \qquad (3.12)\\ &2\Big\{A(m+1)[\delta_{nm+1} - \delta_{nm}] + Bm[\delta_{nm-1} - \delta_{nm}]\Big\} \quad , \end{aligned}$$

where δ_{ik} denotes the Kroneker delta. Notice that L_{nm} is tridiagonal, the upper diagonal corresponding to the one-photon absorption $a\rho a^\dagger$ of the loss term $\mathcal{D}[a]$, the lower diagonal corresponding to the one-photon emission $a^\dagger\rho a$ of the gain term $\mathcal{D}[a^\dagger]$, and the main diagonal containing the anticommutators coming from both terms. In Fig 3.3a we show a typical result of a Monte Carlo experiment of the tomographic reconstruction of the Liouvillian (3.12). We used quantum efficiency $\eta_D = 80\%$ at the conditioning detector D and $\eta_H = 85\%$ at the homodyne detector H. One can see that the details of the matrix are well recovered, and the truncation of the Hilbert space dimension does not affect the reconstruction. In Fig. 3.4 the three main diagonals of the matrix are plotted with their statistical errors against the theoretical value, showing a very good agreement. The statistical errors are of the same size of those of the tomographically reconstructed output probabilities. Notice that the number of data $10^{11} \div 10^{12}$ needed for this experiment could be collected in a reasonable time with a repetition rate of 80 MHz. In Fig. 3.3b we present a simulated experiment using the value $\eta_D = 30\%$ of quantum efficiency (which is a typical value of η for conventional single-photon resolving detectors), however for the reconstruction of a smaller matrix 5×5. Notice that only the photodetector D is required to be linear single-photon resolving, whereas the homodyne detector takes advantage of amplification from the LO, and hence can use high efficiency detectors (the value $\eta_H = 85\%$ here used has been widely surpassed in the real-life tomographic experiments, as in Ref. [21]).

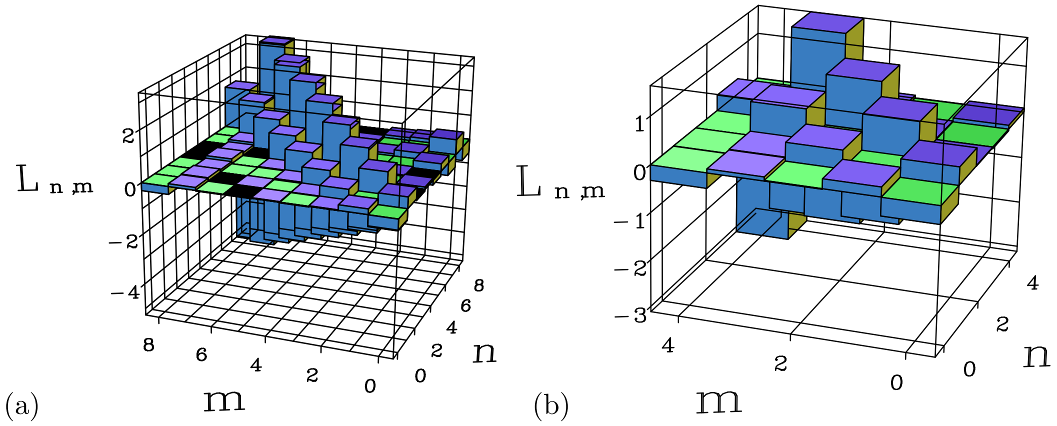

Figure 3.3: Monte Carlo simulation of the reconstruction, by means of the proposed experimental setup, of a linear phase insensitive laser amplifier whose Liouvillian L_{nm} is given in Eq. (3.12). Here $A = 0.194$ and $B = 9.45 \cdot 10^{-3}$. The reconstruction is performed by using 2 statistical blocks of 10^6 homodyne data for each of the output states. Homodyne quantum efficiency is $\eta_H = 85\%$. In Fig. (a) a conditioning detector D with efficiency $\eta_D = 80\%$ has been used. Here the NOPA gain is $\xi = 0.6$, hence a total of $2.7 \cdot 10^{11}$ homodyne data are needed in order to obtain the 10^6 data per output state we actually used in the reconstruction. In Fig. (b) $\eta_D = 30\%$ has been used, with a NOPA gain of $\xi = 0.4$. Hence a total of $9.9 \cdot 10^{11}$ total experimental data are needed.

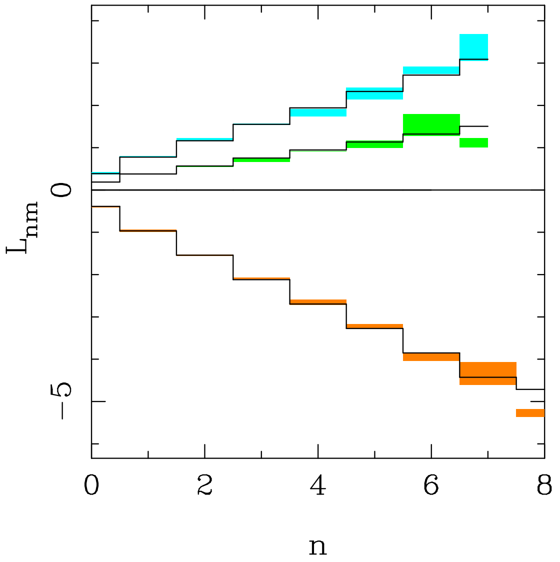

Figure 3.4: The three main diagonals of the Liouvillian L_{nm} of Fig. 3.3a are given with their statistical error bars. The solid line is the theoretical value from Eq. (3.12).

As another example, we simulated the experimental tomography of the effective Liouvillian of a one-atom traveling-wave laser amplifier. In Fig. 3.5 the theoretical Liouvillian matrix is plotted, as obtained from a long-run quantum jump simulation [60] of the one-atom-laser master equation [61, 62]. In the quantum jump simulation, the number of "histories", which have to be used, must be high enough so that the statistical fluctuations inherent in such calculation method become inappreciable. The laser's master equation is obtained by joining the rotating wave approximation Jaynes-Cummings Hamiltonian with the Liouvillian of an empty cavity and with the canonical Bloch single atom Liouvillian. The result (see [63, 64, 65]) is given by

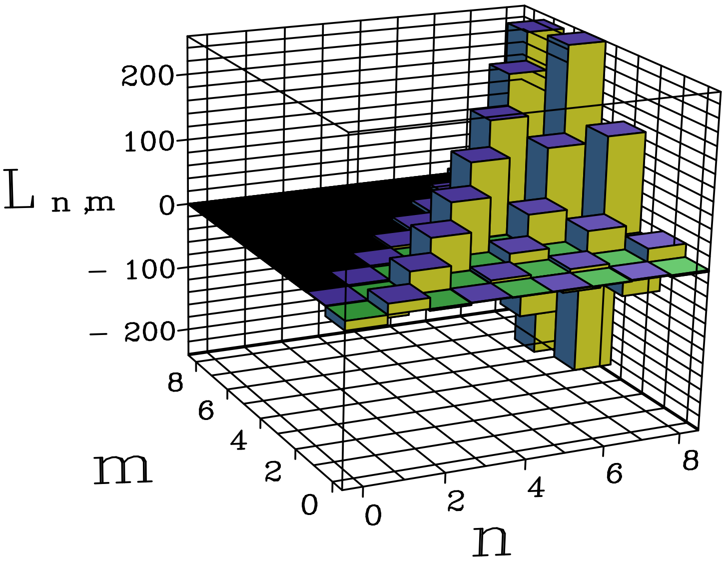

Figure 3.5: Theoretical Liouvillian for a one-atom laser, obtained by solving numerically the master equation (3.13). The parameters for this laser are $C \overset{\text{def}}{=} \frac{g^2}{\gamma\gamma_\perp} = 12$; $n_s \overset{\text{def}}{=} \frac{\gamma_\parallel\gamma_\perp}{4g^2} = 7$; $\sigma_0 = 1$; $f = \frac{\gamma_\parallel}{2\gamma_\perp} = 1$; $\gamma = 1$; $t_* = .0115$.

$$\dot\rho = \Big\{ \tfrac{\gamma_\parallel}{2}(1+\sigma_0)\mathcal{D}[\sigma_+] + \tfrac{\gamma_\parallel}{2}(1-\sigma_0)\mathcal{D}[\sigma_-] + \\ \tfrac{1}{4}\left(\gamma_\perp - \tfrac{\gamma_\parallel}{2}\right)\mathcal{D}[\sigma_z] + \gamma\mathcal{D}[a]\Big\}\rho + g[\sigma_+ a - \sigma_- a^\dagger, \rho] \tag{3.13}$$

where g is the electrical-dipole coupling, $\gamma_\parallel$ and $\gamma_\perp$ are the decay rates of population inversion and atomic polarization respectively, γ is the cavity decay rate, σ_0 is the unsaturated inversion ($-1 \leqslant \sigma_0 \leqslant 1$), ρ now denotes the joint atom-radiation density matrix, and $\sigma_{\pm z}$ are the Pauli matrices

$$\sigma_+ \overset{\text{def}}{=} \begin{pmatrix} 0 & 1 \\ 0 & 0 \end{pmatrix}, \quad \sigma_- \overset{\text{def}}{=} \begin{pmatrix} 0 & 0 \\ 1 & 0 \end{pmatrix}, \quad \sigma_z \overset{\text{def}}{=} \begin{pmatrix} 1 & 0 \\ 0 & -1 \end{pmatrix}. \tag{3.14}$$

In the quantum jump simulation, the atom is traced out at a time $t_* \gg \gamma_{\parallel,\perp}^{-1}$. In Fig.

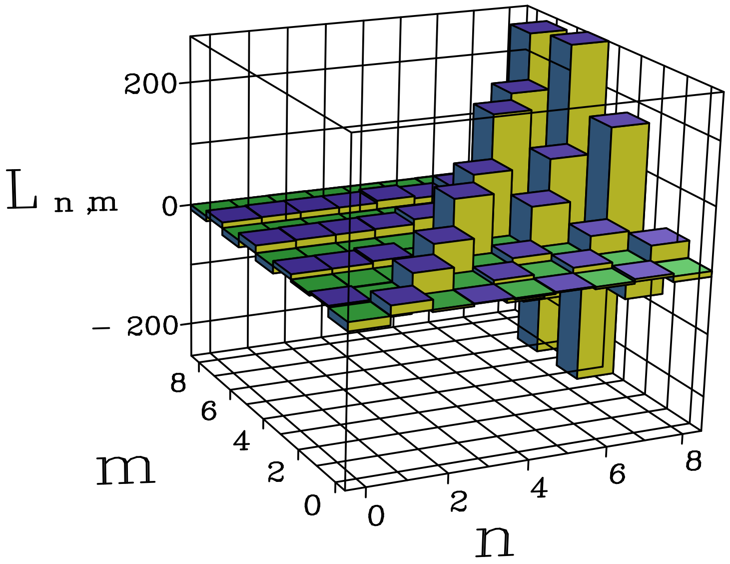

Figure 3.6: Monte Carlo simulated experiment for the reconstruction of the laser theoretical Liouvillian in Fig. 3.5. Here $\eta_D = 80\%$, $\eta_H = 85\%$, and $\xi = .65$. A set of $8 \cdot 10^7$ homodyne data have been used of a total of $3.7 \cdot 10^{11}$ measurements with random photon number at detector D.

3.6 a Monte Carlo simulated tomographic experiment is shown for the measurement of the Liouvillian of Fig. 3.5 (the output homodyne probabilities are simulated starting from the quantum jump Green matrix). An analogous simulated experiment is given in Fig. 3.7 for the limiting case of perfect photodetection: here only the statistical errors deriving from the tomographic reconstruction procedure are present. One can see how the method allows a detailed reconstruction of L_{nm}, including not only one-photon processes on the three main diagonals, but also multiphoton-absorptions on the upper triangular part.

As a final example for the method, we give the simulation of the Liouvillian reconstruction of a two photon phase insensitive amplifier, which is analogous to the PIA defined in Eq. (3.10). Its Liouvillian is

$$\mathcal{L} = A\mathcal{D}[a^\dagger] + B\mathcal{D}[a] + C\mathcal{D}[a^2] + D\mathcal{D}[(a^\dagger)^2] \,, \tag{3.15}$$

where a is the annihilation operator for the field mode, B and C are the one photon and two photon absorption coefficients respectively, and A and D are the one and two photon creation coefficients. The Liouvillian matrix L_{nm} is, in this case

$$L_{nm} = A(m+1)[\delta_{nm+1} - \delta_{nm}] + Bm[\delta_{nm-1} - \delta_{nm}] +$$

$$Cm(m+1)[\delta_{nm-2}-\delta_{nm}]+D(m+2)(m+1)[\delta_{nm+2}-\delta_{nm}] \quad . \tag{3.16}$$

The plot of the theoretical Liouvillian and the reconstructed one, given also here in the limiting cases of perfect photodetection (*i.e.* $\eta_D = \eta_H = 100\%$), are given in Fig. 3.8.

In conclusion, we have seen that it is possible to experimentally reconstruct the Liouvillian of an arbitrary quantum optical phase-insensitive device, using homodyne tomography in a scheme based on parametric down conversion from a NOPA. We have shown the feasibility of the reconstruction with an experimental setup that uses standard technology devices. The problem of low efficiency at the single-photon resolving detector D—the major obstacle for the experiment—has been solved by implementing a compensation algorithm that makes the reconstruction of 5×5 Liouville matrix possible even for $\eta_D = 30\%$, and with a number of data that can be collected in a reasonable time of experimental run.

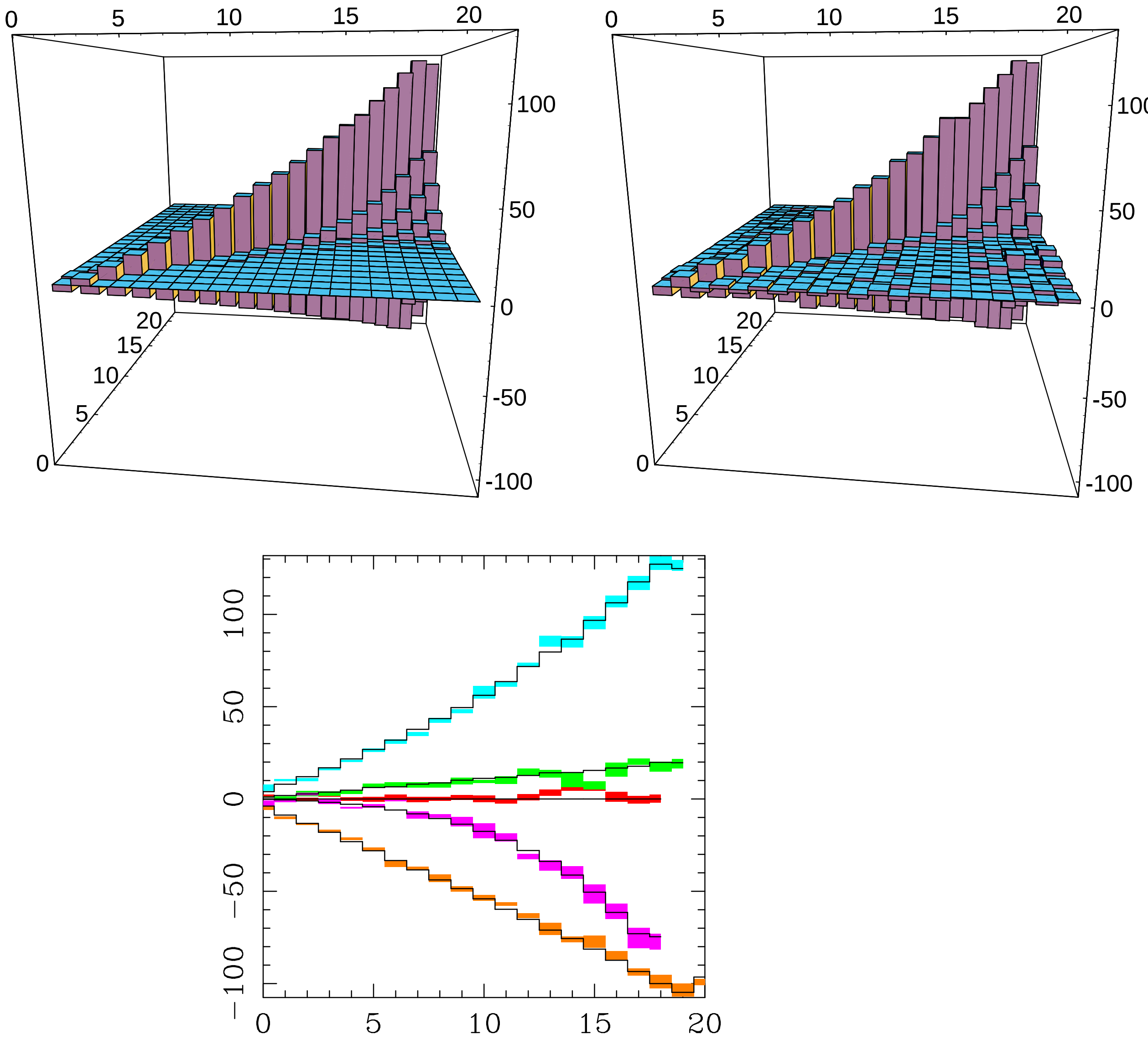

Figure 3.7: On the upper left a theoretical Liouvillian for a one-atom laser, obtained by solving the master equation (3.13) by the quantum-jump method. The parameters for this laser are $C \overset{\mathrm{def}}{=} \frac{g^2}{\gamma\gamma_\perp} = 20$; $n_s \overset{\mathrm{def}}{=} \frac{\gamma_\parallel\gamma_\perp}{4g^2} = .5$; $\sigma_0 = 1$; $f = \frac{\gamma_\parallel}{2\gamma_\perp} = 1$; $\gamma = 1$. On the upper right a Monte Carlo simulated experiment for the reconstruction of the laser Liouvillian. In the reconstruction $\eta_D = 100\%$, $\eta_H = 100\%$ (hence only the statistical errors from the tomographic technique are here appreciable), and five statistical blocks of 4000 homodyne data for each output state have been used. In the lower graph some of the non-zero diagonals of the laser Liouvillian are plotted with the error bars. The full line is the theoretical Liouvillian coming from the quantum jump numerical solution.

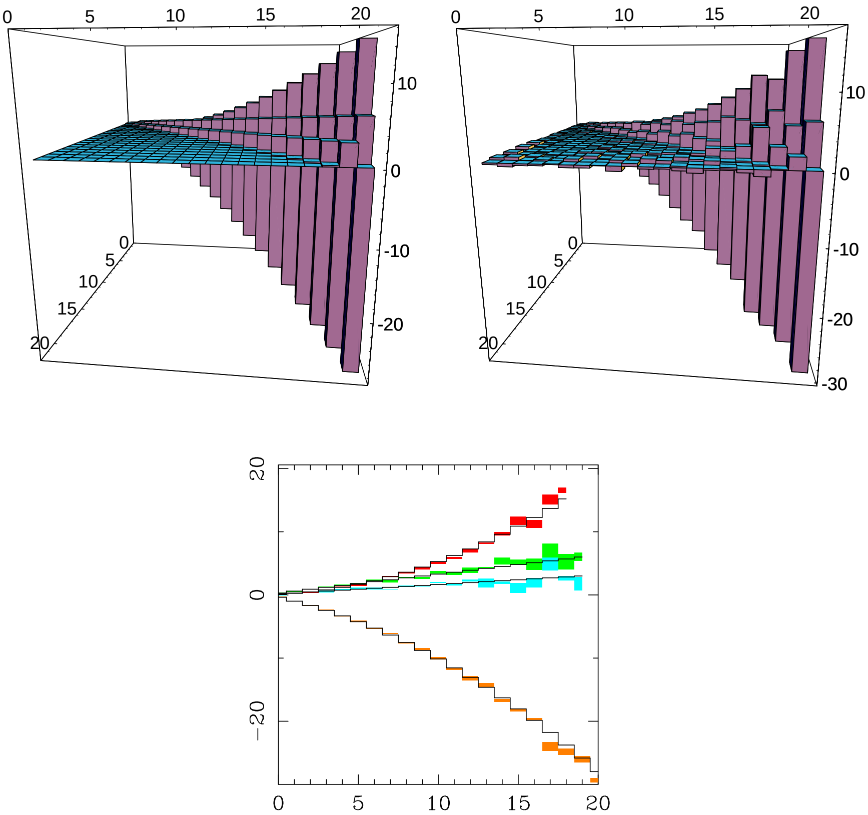

Figure 3.8: The upper left graph shows the theoretical matrix L_{nm} plotted *versus* m and n from Eq. (3.16). The parameters of the two photon phase insensitive amplifier are $A = 0.3$; $B = 0.15$; $C = 5 \cdot 10^{-4}$; $D = 4 \cdot 10^{-2}$. On the upper right the result of a Monte Carlo simulation of the measurement of the same Liouvillian is given. The reconstruction of L_{nm} is simulated by using only 15000 homodyne measurements divided into 3 statistical blocks of data for each input state. In the lower graph the four non–zero diagonals of the reconstructed Liouvillian matrix L_{nm} are plotted with the statistical error bars. The dark line is the theoretical value from Eq. (3.16). Notice that, as for the previous figures, this experiment is in the limiting case of perfect photodetection at homodyne and at the conditional photodetector. In practical cases it will be very difficult to reconstruct matrices with these dimensions.

3.3 Generation and detection of Schrödinger cat states

In this section we show[2] [51] the feasibility of a tomographic reconstruction of the "Schrödinger-cat states" generated according to the scheme proposed by S. Song, C. M. Caves and B. Yurke (SCY) in [52]. Here also we use the deconvolution technique that was presented in Sect. 3.2, which tolerates realistic values for quantum efficiency at photodetectors. The measurement can be achieved with a standard experimental setup.

Some experiments have been performed to detect Schrödinger cat states in atomic systems [66]. For radiation, the scheme to detect cat states proposed by SCY was not supported by a feasibility study for a real experiment, concerning in particular the main issue of the quantum efficiency of the detectors which washes out the fringes visibility. In this section a concrete experimental setup for this scheme is proposed by requiring the detection of the output field by means of homodyne tomography and by making use of the quantum efficiency compensating method which was presented in Sect. 3.2 for the deconvolution of the noise introduced by an inefficient conditioning photodetector. This allows a good reconstruction of the Wigner function of the Schrödinger cat and the recovery of the visibility of the experiment, even with quantum efficiency $\eta_d = 30\%$ at the readout photodetector, and $\eta_h = 80\%$ at the homodyne detector. Our proposal to reconstruct the Wigner function allows to appreciate the detailed structure of the state rather than just seeing the oscillations in a single quadrature probability distribution. To our knowledge, this is the first method for detecting the density operator of Schrödinger cat states for free radiation, feasible with current technology.

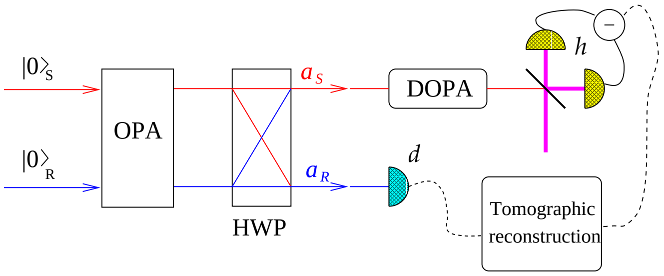

Figure 3.9: Experimental scheme for generation and tomographic detection of Schrödinger cats. The two detectors, homodyne and conditioned-photomultiplier, are indicated with the letters h and d respectively. [(D)OPA: (degenerate) optical parametric amplifier; HWP: half wave plate used as polarization mixer.]

---

[2] This work has been supported by the PRA–CAT97 of the INFM. We also thank Prof. T. F. Arecchi for illuminating discussions on the experimental setup. Prof. Arecchi and his group in Firenze are currently performing a similar experiment, also based on [52].

Let us first briefly review the experimental scheme for generating Schrödinger cat states proposed in Ref.[52] (similar setups were later proposed in Refs.[67]). The main idea, sketched in Fig 3.9, consists in feeding two orthogonally polarized modes of radiation, called "signal" and "readout", both initially in the vacuum state, into a parametric amplifier followed by a half-wave plate. The parametric amplifier generates a correlated state of the two modes and the half wave plate rotates the polarization directions by an angle θ. The global state of the two modes at the output of this setup is given by

$$|\psi\rangle = T(\theta)V(r)|0\rangle|0\rangle = \sum_{j=0}^{\infty}\sum_{m=-j}^{j} B_{j,m}|j-m\rangle|j+m\rangle \ , \tag{3.17}$$

where $V(r) = \exp[r(a_S a_R - a_S^\dagger a_R^\dagger)]$ describes the action of the parametric amplifier (a_S and a_R being the annihilation operators for the signal and readout mode respectively), $T(\theta) = \exp[\theta(a_S a_R^\dagger - a_S^\dagger a_R)]$ describes the polarization rotator and the coefficients $B_{j,m}$ are given by

$$\begin{aligned} B_{j,m} = & \quad \frac{(-\tan\theta)^m(-\tanh r)^j}{\cosh r}\sqrt{\frac{(j+m)!}{(j-m)!}} \\ & \times \sum_{k=max(0,-m)}^{j} \frac{(j+k)!}{k!(j-k)!(m+k)!}(-\sin^2\theta)^k \ . \end{aligned} \tag{3.18}$$

The rotation angle θ and the gain parameter r are related by the back-action-evading condition [68] as $\sin 2\theta = \tanh r$. The following step of the scheme consists in detecting the number of photons at the readout mode. As a consequence of this measurement, given n_r photons detected at the readout, the signal mode is reduced to the state

$$|\psi_{S,n_r}\rangle = \left\{ \begin{array}{lr} \frac{1}{P(n_r)}\sum_{j=0}^{\infty} B_{j+\frac{n_r}{2},j-\frac{n_r}{2}}|2j\rangle & n_r \text{ even} \\ \frac{1}{P(n_r)}\sum_{j=0}^{\infty} B_{j+\frac{n_r+1}{2},j-\frac{n_r-1}{2}}|2j+1\rangle & n_r \text{ odd} \end{array} \right. , \tag{3.19}$$

where $P(k)$ is the probability of detecting k readout photons with a perfect photodetector, namely

$$P(k) = 2^k\frac{(2k-1)!!}{(2k)!!}\frac{(\sinh r)^{2k}}{(2\sinh^2 r+1)^{k+1/2}} \ . \tag{3.20}$$

In the scheme of Ref. [52], after detection of the readout mode, the signal mode enters a degenerate parametric amplifier with gain parameter r_s, described by the evolution operator $S(r_s) = \exp[\frac{1}{2}r_s(a_S^2 - a_S^{\dagger 2})]$, which increases the distance of the two components of the superposition in the complex plane without changing the oscillating behavior of the number probability distribution. The final state of the signal is then described by the following quadrature probability distribution of obtaining $X_S(\phi)$ as the result of the measurement of the quadrature x_ϕ if the conditioning photodetector measured n_r photons, *i.e.*

$$P(X_S(\phi)|n_r) = \frac{(2\mathrm{Re}\lambda/\pi)^{1/2}}{(2n_r-1)!!\sigma^{n_r/2}}e^{-2\mathrm{Re}\lambda X_S^2(\phi)}\left|H_{n_r}(\sqrt{\lambda}X_S(\phi))\right|^2 \ , \tag{3.21}$$

where H_n denotes the Hermite polynomial,

$$\lambda \overset{\text{def}}{=} \frac{1}{\cos\phi(e^{-2r_s}\cosh 2r\cos\phi + i\sin\phi)} \ , \tag{3.22}$$

and

$$\sigma \overset{\text{def}}{=} 1 + \tan^2\phi \, \frac{e^{2r_s}}{\cosh 2r} \ . \tag{3.23}$$

Let us now consider the effect of non unit quantum efficiency η_d at the readout photodetector. As has been already frequently remembered, according to the Mandel-Kelley-Kleiner formula [38], a detector with non unit quantum efficiency is equivalent to a perfect photodetector preceded by a beam splitter with transmissivity η_d. Then, one can see that, when n_r photons are detected at the readout, the signal mode is left in the following statistical mixture of Schrödinger cat states

$$\rho_{S,n_r} = \frac{1}{P_{\eta_d}(n_r)} \sum_{k=n_r}^{\infty} \begin{pmatrix} k \\ n_r \end{pmatrix} \eta_d^{n_r}(1-\eta_d)^{k-n_r} P(k) |\tilde{\psi}_{S,k}\rangle\langle\tilde{\psi}_{S,k}| \ , \tag{3.24}$$

where

$$|\tilde{\psi}_{S,k}\rangle = S(r_s)|\psi_{S,k}\rangle \tag{3.25}$$

is the conditional Schrödinger cat state at the signal mode (3.19) evolved by the degenerate parametric amplifier, and $P_{\eta_d}(k)$ is the probability of detecting k readout photons with quantum efficiency η_d, *i.e.* the Bernoulli convolution of the probability (3.20). In Fig. 3.11 we plot a Monte Carlo tomographic reconstruction of the Wigner function of the statistical mixture (3.24) corresponding to an experiment with $\eta_d = 30\%$, $\eta_h = 80\%$, $r = r_s = 0.4$ and $n_r = 2$. This reconstruction must be compared to the theoretical Wigner function that corresponds to the cat state (3.25) which is plotted in Fig. 3.10. As expected, the effect of non unit quantum efficiency is to smooth out the oscillations in the complex plane, which are the typical signature of quantum interference. Therefore, the resulting state is more similar to a classical mixture of coherent states rather than a Schrödinger cat. The degradation effects on the cat due to non unit η_d can be seen also in Fig. 3.12, where the tomographic reconstructed number probability, obtained from the same simulation, is plotted: the probability still exhibits a non-monotonic behavior, but the even terms no longer vanish. In Fig. 3.13 we report a simulation of the quadrature probability distribution at $\phi = 0$, which would be seen following the original proposal [52], with the corresponding theoretical curve. Here also it is possible to note a complete wash out of the fringe visibility.

In order to compensate these dramatic effects of the quantum efficiencies we would find in a real experiment, we may use the same Bernoulli inversion technique that was presented and derived in Sect. 3.2. The main idea consists in the inversion of formula

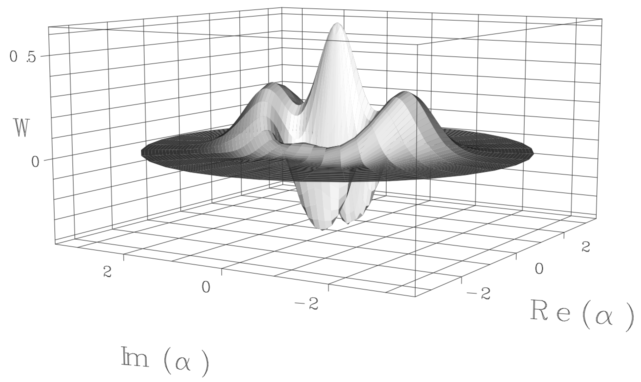

Figure 3.10: Theoretical Wigner function of the Schrödinger cat state (3.25), with parameters $r = r_s = 0.4$ and $n_r = 2$.

(3.24). In fact, one can see that Eq. (3.24) is of the form (3.7) and hence an inversion of the type (3.8) can be obtained. This is achieved by shifting the index k in the series at the right hand side of (3.24), and the formula can be inverted as follows

$$|\tilde{\psi}_{S,k}\rangle\langle\tilde{\psi}_{S,k}| = P(k)^{-1}\eta_d^{-k}\sum_{j=0}^{\infty}\left(\begin{array}{c} k+j \\ k \end{array}\right)\left(1-\frac{1}{\eta_d}\right)^{j}\rho_{S,k+j}P_{\eta_d}(k+j)\ , \tag{3.26}$$

as one can check *a posteriori* by substituting expression (3.26) into Eq. (3.24). Hence, a generic k-th Schrödinger cat component of the signal mode can be reconstructed by measuring all the signal states corresponding to different readout numbers of photons (larger or equal to k), and weighting each event according to Eq. (3.26). In this way we have the additional advantage of using all data with $n_r \geqslant k$ and not just those with $n_r = k$ as in the plain detection in Fig. 3.11. Moreover, by processing the homodyne data according to Eq. (3.26) we can reconstruct the whole family of Schrödinger cats $|\tilde{\psi}_{S,k}\rangle$ for different k's at the same time. In Fig. 3.14 we show a tomographic reconstruction of the same Schrödinger cat component of Fig. 3.11, with the same values of the experimental parameters, but using the reconstruction procedure based on the inversion (3.26). As we can see, all the oscillations in the Wigner function are properly recovered, and the destructive effects of low quantum efficiencies are defeated. Notice that unlike other compensation methods based on the inverse Bernoulli transformation [69], where the convergence radius of the procedure is for $\eta > 50\%$, the present method works also for very low values of the quantum efficiency. In our case convergence of the series (3.26) below the threshold $\eta_d = 50\%$ is due to the additional decaying factor $P_{\eta_d}(k+j)$. An analysis of convergence (see Sect. 3.6) of the series of errors as in Ref. [70] shows that there is no lower-bound for η_d if $r \leqslant \frac{1}{2}\ln(2+\sqrt{3}) \simeq 0.658$. Notice that the series convergence is slower for increasing r, which corresponds to more

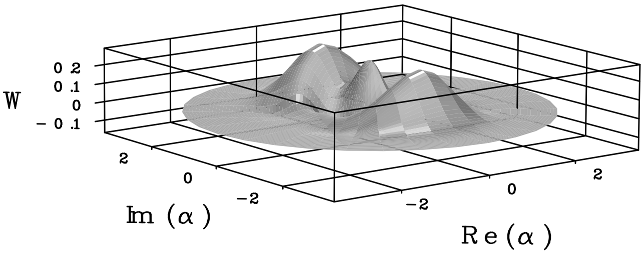

Figure 3.11: Monte Carlo tomographic reconstruction of the Wigner function of the state in Eq. (3.24), with the same parameters as in Fig. 3.10 (*i.e.* $r = r_s = 0.4$ and $n_r = 2$). The detectors quantum efficiencies are $\eta_d = 30\%$ and $\eta_h = 80\%$. Data are collected for 70 different homodyne phases and $4 \cdot 10^5$ simulated data are used for each phase.

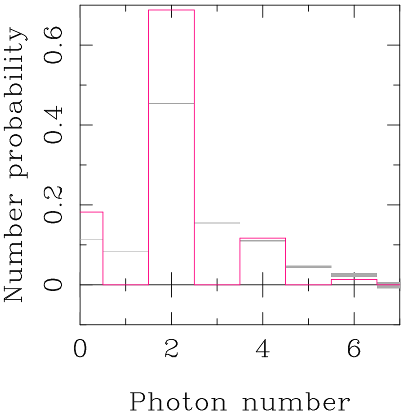

Figure 3.12: Monte Carlo tomographic reconstruction of the probability distribution for the same state and same simulated data of Fig. 3.11. The simulated values with the corresponding statistical error bars are superimposed to the theoretical values (solid line). Notice how the reconstructed photon number distribution is ruined by the effect of the detector's quantum efficiency.

excited (macroscopic) Schrödinger cats. This implies that the more macroscopic the cat is, the higher η_d must be in order to have a good reconstruction. In Fig. 3.15 we plot the number probability for the same parameters of Fig. 3.14: the simulated experimental results with corresponding error bars are superimposed to the theoretical value. As we can see, the tomographic reconstruction is very precise and the oscillations

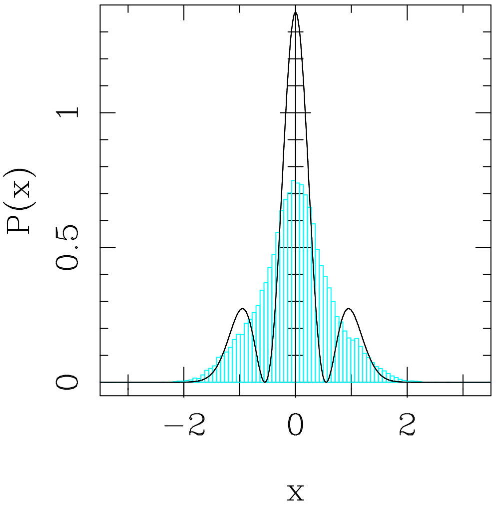

Figure 3.13: Monte Carlo tomographic simulation of the quadrature probability at $\phi = 0$ for the same state of Fig. 3.11. The histogram contains 20000 simulated data, while the solid curve is the theoretical distribution. This is how the output of SCY's proposal [52] would look like if their experiment was carried out with inefficient photodetectors.

of the probability are perfectly resolved. In Fig. 3.16 we finally report the quadrature probability distribution for $\phi = 0$ superimposed to the theoretical curve. The visibility is totally recovered, in contrast to the result in Fig. 3.13, which would have been obtained according to the original proposal of Ref. [52].

Let us now discuss in more detail the experimental feasibility of the scheme. The experimental setup is analogous to the one proposed in Sect. 3.2, since, up to the conditioning photodetector d, the two setups are similar. All the devices needed in the experiment are available with the current technology. The parametric amplification can be realized for example by an ordinary KPT crystal pumped with the second harmonic of a mode locked Nd:Yag pulsed laser working at 80 MHz with 7 ps pulses [71]. The major problem encountered to detect Schrödinger cats in conditional measurement schemes is the cat's notorious fragility to any kind of losses and inefficiencies. The novelty of the present proposal is that using the reconstruction method based on Eq. (3.26) low values of η_d can be tolerated, and hence ordinary linear avalanche photodiodes with $\eta_d \sim 30\%$ can be used. On the other hand, the tomographic apparatus needed to detect the Schrödinger cat at the signal mode is based on homodyne detection, with the possibility of using high–efficiency photodetectors, because single-photon resolution is no longer needed due to the amplification from the local oscillator (LO). Moreover, the LO comes from the same laser source of the classical pump of the OPA, in order to achieve time matching of modes. In addition, since there is no fluctuating phase in the whole

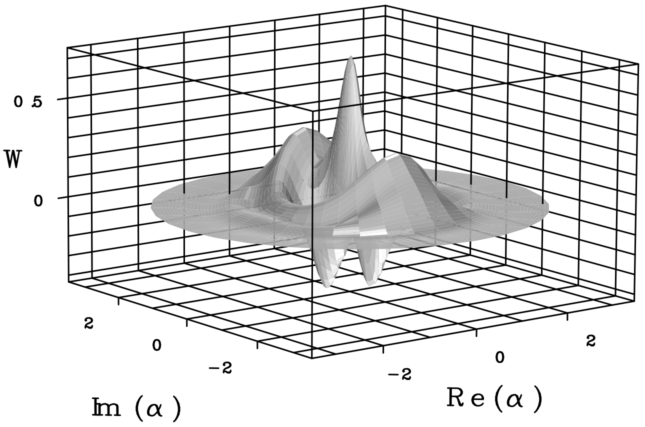

Figure 3.14: Monte Carlo simulated reconstruction of the Wigner function of the state $|\tilde{\psi}_{S,2}\rangle$ with $\eta_d = 30\%$, $\eta_h = 80\%$, $r = r_s = 0.4$, using the reconstruction algorithm (3.26). The same number of simulated data as in Fig. 3.11 is used. Notice that the reconstructed Wigner function is almost indistinguishable from the theoretical, shown in Fig. 3.10.

optical setup, neither in the second harmonic generation stage nor in the homodyne detection, the LO is also perfectly phase matched with the pump. The resulting setup is very stable and can take measurements for long periods of time at a rate that might reach 10^8 data/sec at the readout photodetector. The tomographic reconstructions presented in this section were obtained with $2.8 \cdot 10^7$ experimental data. In these examples the probability of detecting less than two photons at the readout photodetector is ~ 0.9967. Therefore, taking into account that only the fraction $3.3 \cdot 10^{-3}$ of experimental data collected at the readout is useful for the Schrödinger cat reconstruction, we can easily see that the whole set of data can be collected in a few minutes. Notice that increasing k, which corresponds to a more excited cat, the number of useful data decreases, and the reconstruction becomes slower. For example, to reconstruct the cat component with $k = 4$ only $2 \cdot 10^{-5}$ of the experimental data are useful, for $k = 5$ we can use only the fraction $1.7 \cdot 10^{-6}$ of data, and so on. In order to enhance the data rate, the parametric amplification parameter r must be increased. Moreover, to reconstruct more excited cat components, higher index density matrix elements are needed for the Wigner function, and the effect of statistical errors from tomography becomes more dramatic [72], with the consequence that more data are needed to reach a prescribed accuracy. For these reasons, the more excited the cat is, the longer the experiment and the more difficult the state is to detect. Finally, it has been suggested [73] that by lowering the gain r some (non tomographic) homodyne visibility could be detected for high η_h ($> 90\%$) and for η_d as low as 30%, even without our reconstruction algorithm.

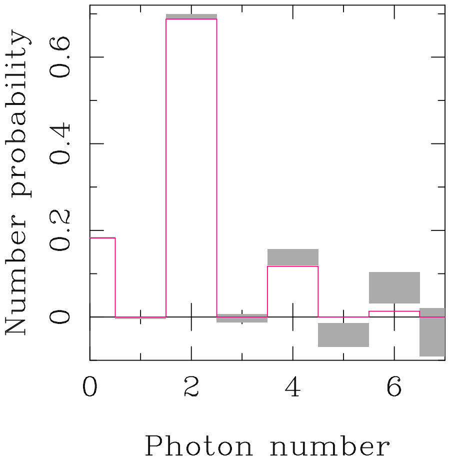

Figure 3.15: Photon number probability of the cat $|\tilde{\psi}_{S,2}\rangle$ using the reconstruction algorithm (3.26), with the same parameters as in Fig. 3.14. The simulated values with the corresponding statistical error bars are superimposed to the theoretical values (solid line).

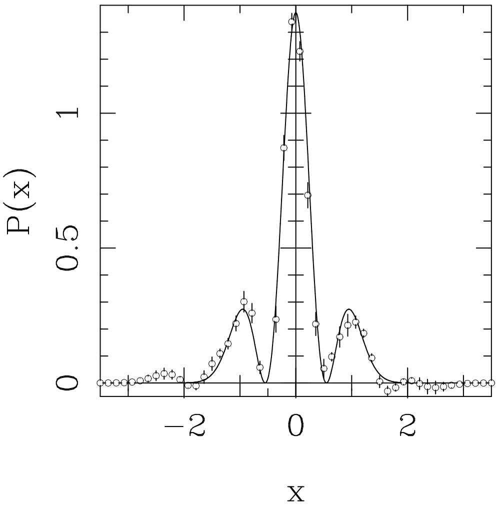

Figure 3.16: Quadrature probability distribution at zero phase of the cat state $|\tilde{\psi}_{S,2}\rangle$, with the same parameters as in Fig. 3.14. The simulated values with the corresponding statistical error bars are superimposed to the theoretical curve (solid line).

However, by lowering the gain the data acquisition rate is greatly reduced, whereas our method works also with high gains.

In conclusion, we have shown the feasibility of a tomographic reconstruction of a Schrödinger cat in an experimental scheme which is practical in a laboratory using standard technology devices. The problem of low efficiencies at the single-photon resolving detector, which was regarded as the major obstacle for experiments of this kind [52], has been solved by the implementation of a suitable data processing technique. The whole density matrix of the cat, and hence all its characteristics (such as the photon number probability, the quadrature distribution and the Wigner function), can be measured in this way, whereas the plain homodyne detection proposed in the original scheme of Ref. [52] would not have provided visible probability oscillations with the available low-efficiency single-photon-resolving detectors.

3.4 Homodyne test of the State reduction postulate

In this section, we present[3] an experiment for testing quantum state reduction as described in [53]. The state reduction rule is tested using optical homodyne tomography to measure directly the fidelity between the reduced experimental state and the state we would obtain theoretically by applying the customary state reduction rule.

In quantum mechanics the state reduction (SR) is still a very discussed rule. The so–called "projection postulate" was introduced by von Neumann [74] to explain the results from the Compton-Simons experiment, and it was generalized by Lüders [75] for measurements of observables with degenerate spectrum. The consistency of the derivation of the SR rule and its validity for generic measurements have been analyzed with some criticism [76]. In a very general context, the SR rule was derived in a physically consistent way from the Schrödinger equation for the composite system of object and measuring apparatus [77, 78]. An experiment for testing quantum SR is therefore a very interesting matter. Such a test in general is *not* equivalent to a test of the repeatability hypothesis since the latter holds only for measurements of observables that are described by self-adjoint operators with discrete spectrum. For example, joint measurements like the Arthurs-Kelly one [79] are not repeatable, as the reduced states are coherent states, which are not orthogonal.

Quantum optics offers a possibility of testing the SR, because several observables can be chosen to perform different measurements on a fixed system. For instance, one can decide to perform either homodyne or heterodyne detection, or photon-number detection. To our knowledge this is a unique opportunity. In fact in other quantum systems, such as particle physics or spin state analysis, the measurements are mostly quasi-classical and restricted to only a few observables. In addition, as we have seen already, tomography is a powerful tool for measuring the density operator of the radiation field through optical homodyne tomography, whereas its applications to other

---

[3] This work has been supported in part by the PRA–CAT97 of the INFM.

quantum systems are sporadic and not yet well assessed.

A scheme for testing the SR could be based on tomographic measurements of the radiation density matrix after non-demolition measurements. However, such a scheme would reduce the number of observables that are available for the test, since one would have to find a way to perform measurements in a non-demolitive manner. Instead, one can take advantage of the correlations between the twin beams produced by a non-degenerate optical parametric amplifier (NOPA), in which case one can test the SR even for demolitive-type measurements. Indeed, if a measurement is performed on one of the twin beams, the SR can be tested by homodyne tomography on the other beam.

Our scheme for the SR test is given in Fig. 3.17 (for the experimental setup see Subsec. 3.4.3). Different kinds of measurements can be performed on beam 1: in Subsect. 3.4.1 we show in detail the SR for heterodyne detection as well as photon-number detection, but any other kind of detection (such as homodyne or phase detection by heterodyne) could be considered.

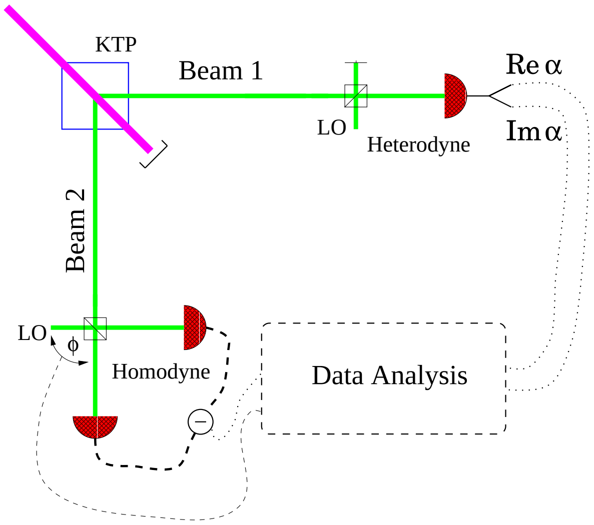

Figure 3.17: Schematic of the proposed scheme for testing the SR for heterodyne detection. A NOPA generates a pair of twin beams (1 and 2). After heterodyning beam 1, the reduced state of beam 2 is analyzed by homodyne tomography, which is conditioned by the heterodyne outcome. In place of the heterodyne detector one can put any other kind of detector for testing the SR on different observables. In this section we also consider the case of direct photodetection.

In this thesis the radiation state of the twin beams produced by a NOPA with vacuum input has been used in practically all of the proposed setups. It can be written as

$$|\xi\rangle = V(r)|0\rangle|0\rangle = (1-|\xi|^2)^{1/2}\sum_{n=0}^{\infty}\xi^n|n\rangle|n\rangle \,, \tag{3.27}$$

where $V(r) = \exp[r(a_1^\dagger a_2^\dagger - a_1 a_2)]$ (for real r) describes the action of the parametric amplifier having a gain parameter $\xi = \tanh(r)$. The subscripts 1 and 2 refer to operators of beams 1 and 2.

3.4.1 Physical analysis for heterodyne and direct detections

Before calculating the SR, we briefly recall the concept of Probability Operator-Valued Measure (POVM). For a system described by a density operator ρ, the probability $p(\lambda)\mathrm{d}\lambda$ that the outcome of a quantum measurement of an observable is in the interval $[\lambda, \lambda + \mathrm{d}\lambda)$ is given by Born's rule $p(\lambda)\mathrm{d}\lambda = \mathrm{Tr}[\rho\, P_\lambda \mathrm{d}\lambda]$, where $P_\lambda \mathrm{d}\lambda$ is the POVM pertaining to the measurement (such that $P_\lambda \geqslant 0$ and $\int \mathrm{d}\lambda\, P_\lambda = \mathbb{1}$). For an exact measurement of an observable, which is described by a self-adjoint operator, P_λ is just the projector over the eigenvector corresponding to the outcome λ. In the case of the photon number $a^\dagger a$ the spectrum is discrete and the POVM is $P_m = |m\rangle\langle m|$ for integer eigenvalue m. For the Arthurs-Kelly joint measurement of the position and momentum (corresponding to a joint measurement of the two quadratures of the field) we have [37] $P_\alpha = \pi^{-1}|\alpha\rangle\langle\alpha|$, where $|\alpha\rangle$, $\alpha \in C$, is a coherent state, *i.e.* $a_1|\alpha\rangle = \alpha|\alpha\rangle$.

Now let us analyze the SR for our scheme. When on beam 1 we perform a measurement described by P_λ, the reduced normalized state of beam 2 is

$$\rho(\lambda) = \frac{\mathrm{Tr}_1[|\xi\rangle\langle\xi|(P_\lambda \otimes \mathbb{1})]}{\mathrm{Tr}_{1,2}[|\xi\rangle\langle\xi|(P_\lambda \otimes \mathbb{1})]} = \frac{\Xi P_\lambda^* \Xi^\dagger}{p(\lambda)} \,, \tag{3.28}$$

where $\Xi = (1-|\xi|^2)^{1/2}\xi^{a^\dagger a}$, and $p(\lambda) = \mathrm{Tr}_{1,2}[\Xi P_\lambda^* \Xi^\dagger]$ is the probability density of the measurement outcome λ. In the limit of infinite gain ($\xi \to 1$) $\rho(\lambda) \propto P_\lambda^*$; for example, for heterodyne detection with outcome α, we have $\rho(\alpha) = |\alpha^*\rangle\langle\alpha^*|$.

If the readout detector on beam 1 has quantum efficiency η_r, then according to the SR rule [76] the state in beam 2 is

$$\rho^{\eta_r}(\lambda) = \frac{\Xi(P_\lambda^{\eta_r})^* \Xi^\dagger}{p^{\eta_r}(\lambda)} \,, \tag{3.29}$$

where $p^{\eta_r}(\lambda) = \mathrm{Tr}_{1,2}[\Xi(P_\lambda^{\eta_r})^*\Xi^\dagger]$, and $P_\lambda^{\eta_r}$ is the POVM for measurement with a non-unit quantum efficiency. For heterodyne detection one has [37]

$$P_\alpha^{\eta_r} = \frac{1}{\pi}\int \frac{\mathrm{d}^2 z}{\pi\Delta_{\eta_r}^2}\, e^{-\frac{|z-\alpha|^2}{\Delta_r^2}}\, |z\rangle\langle z| \,, \tag{3.30}$$

where $\Delta_{\eta_r}^2 = (1-\eta_r)/\eta_r$, and η_r is the overall quantum efficiency of the heterodyne detector. For direct photodetection the ideal POVM $P_m = |m\rangle\langle m|$ is modified to [37]

$$P_m^{\eta_r} = \sum_{j=m}^{\infty}\begin{pmatrix} j \\ m \end{pmatrix}\eta_r^m(1-\eta_r)^{j-m}|j\rangle\langle j| \,, \tag{3.31}$$

which, as usually, is obtained by considering an inefficient photodetector as a perfect photodetector preceded by a beam splitter of transmissivity η.

The experimental test proposed in this section consists of performing conditional homodyne tomography on beam 2, given the outcome λ of the measurement on beam 1. Actually, through homodyne tomography we can directly measure the "fidelity of the test"

$$F(\lambda) = \mathrm{Tr}[\rho^{\eta_r}(\lambda)\,\rho_{\mathrm{meas}}(\lambda)]\,, \tag{3.32}$$

where $\rho^{\eta_r}(\lambda)$ is the theoretically expected state in Eq. (3.29), and $\rho_{\mathrm{meas}}(\lambda)$ is the experimentally measured state of beam 2. Notice that in Eq. (3.32) we use the term fidelity even if $F(\lambda)$ is a proper fidelity when at least one of the two states is pure, which occurs in the limit of unit quantum efficiency η_r. In the following we evaluate the theoretical value of the fidelity $F(\lambda)$ and compare it with the simulation of the tomographically measured value.

The fidelity (3.32) can be directly measured by homodyne tomography with use of the kernel function for the operator $\rho^{\eta_r}(\lambda)$, as it can be done for the expectation value of any (generally complex) operator of the field mode (see Chap. 1 and Sect. 2.1). In fact, for a generic operator O, the expectation value $\langle O\rangle$ can be measured by averaging the kernel function $K_{\eta_h}[O](x,\phi)$, defined in Eq. (1.20), over the homodyne data, namely,

$$\langle O\rangle = \int_0^{\pi}\frac{\mathrm{d}\phi}{\pi}\int_{-\infty}^{+\infty}\mathrm{d}x\,p_{\eta_h}(x,\phi)K_{\eta_h}[O](x,\phi)\,, \tag{3.33}$$

where η_h is the overall quantum efficiency of the homodyne detector, and $p_{\eta_h}(x,\phi)$ is the probability distribution of obtaining the result x when measuring the quadrature x_ϕ with a homodyne detector with quantum efficiency η_h. In Sect. 2.1.3 the homodyne tomography kernel function for a generic operator O is derived, with the following result for trace–class operators

$$K_{\eta_h}[O](x,\phi) = \int_0^{+\infty}\mathrm{d}k\,k\,e^{\frac{1-\eta_h}{8\eta_h}k^2}\,\mathrm{Tr}\{O\cos[k(x-x_\phi)]\}\,, \tag{3.34}$$

which can be obtained immediately from the deconvolved estimator (2.17). Thus, $F(\lambda)$ is obtained from an average of the form

$$F(\lambda) = \int_0^{\pi}\frac{\mathrm{d}\phi}{\pi}\int_{-\infty}^{+\infty}\mathrm{d}x\,p_{\eta_h}(x,\phi;\lambda)K_{\eta_h}[\rho^{\eta_r}(\lambda)](x,\phi)\,, \tag{3.35}$$

where $p_{\eta_h}(x,\phi;\lambda)$ is the conditional homodyne probability distribution for outcome λ at the readout detector.

For heterodyne detection of beam 1 with outcome $\alpha\in\mathbb{C}$, the reduced state of beam 2 according to the SR rule is given by the displaced thermal state

$$\rho^{\eta_r}(\alpha) = \eta_\xi D(\gamma)(1-\eta_\xi)^{a^\dagger a}D^\dagger(\gamma)\,, \tag{3.36}$$

where

$$\eta_\xi = 1 + (\eta_r - 1)|\xi|^2\,, \qquad \gamma = \frac{\xi \eta_r}{\eta_\xi}\alpha^*\,, \tag{3.37}$$

and $D(\gamma) = \exp(\gamma a^\dagger - \gamma^* a)$ is the usual displacement operator. The kernel function for measuring $F(\alpha)$ is easily calculated from Eqs. (3.34–3.37). One has

$$K_{\eta_h}[\rho^{\eta_r}(\alpha)](x,\phi) = \frac{2\eta_h\eta_\xi}{2\eta_h - \eta_\xi}\Phi\left(1, \frac{1}{2}; -\frac{2\eta_h\eta_\xi}{2\eta_h - \eta_\xi}(x - \gamma_\phi)^2\right)\,, \tag{3.38}$$

where $\gamma_\phi = \mathrm{Re}(\gamma e^{-i\phi})$, and $\Phi(a, b; z)$ denotes the customary confluent hypergeometric function of argument z. The kernel in Eq. (3.38) is bounded for $\eta_h > \frac{1}{2}\eta_\xi$, *i.e.* for the fidelity measurement, one needs to satisfy the following bound on the quantum efficiencies:

$$\eta_h > \frac{1}{2}\left[1 + |\xi|^2(\eta_r - 1)\right]\,. \tag{3.39}$$

As one can see from Eq. (3.39), for $\eta_h > 0.5$ the fidelity can be measured for any value of η_r and any gain parameter ξ of the NOPA. We recall that the condition $\eta_h > 0.5$ is required for the measurement of the density matrix of a radiation state [70]. However, in a direct measurement of the fidelity the measurement of the density matrix is bypassed and we see from Eq. (3.39) that the bound $\eta_h = 0.5$ can be lowered.

The tomographically measured fidelity $F(\alpha)$ in Eq. (3.35) with $\rho^{\eta_r}(\alpha)$ as given in Eq. (3.36) must be compared with the theoretical value

$$F_{\mathrm{th}}(\alpha) = \eta_\xi/(2 - \eta_\xi)\,. \tag{3.40}$$

Notice that $F_{\mathrm{th}}(\alpha)$ does not depend on α: therefore in the following it will be simply denoted by F_{th}.

Now we analyze the SR for direct photodetection of beam 1. For an outcome n at the readout photodetector, the reduced state of beam 2 is given by

$$\rho^{\eta_r}(n) = \eta_\xi\left(\frac{\eta_\xi}{1 - \eta_\xi}\right)^n \begin{pmatrix} a^\dagger a \\ n \end{pmatrix} (1 - \eta_\xi)^{a^\dagger a}\,. \tag{3.41}$$

The pattern function for the corresponding fidelity measurement is

$$K_{\eta_h}[\rho^{\eta_r}(n)](x,\phi) = \frac{\eta_\xi \partial_z^n}{n!}\bigg|_{z=0} \frac{2\eta_h\eta_\xi}{2\eta_h - \eta_\xi + z}\Phi\left(1, \frac{1}{2}; -\frac{2\eta_h(\eta_\xi - z)}{2\eta_h - \eta_\xi + z}x^2\right)\,. \tag{3.42}$$

We see that the same bound, Eq. (3.39), on the quantum efficiencies holds true also for direct photodetection. In this case, the tomographically-measured fidelity $F(n)$ must be compared with the following theoretical value:

$$F_{\mathrm{th}}(n) = \eta_\xi^{2+2n} F\left(2n + 1, 2n + 1; 1; (1 - \eta_\xi)^2\right)\,, \tag{3.43}$$

where $F(a, b; c; z)$ denotes the customary hypergeometric function of argument z.

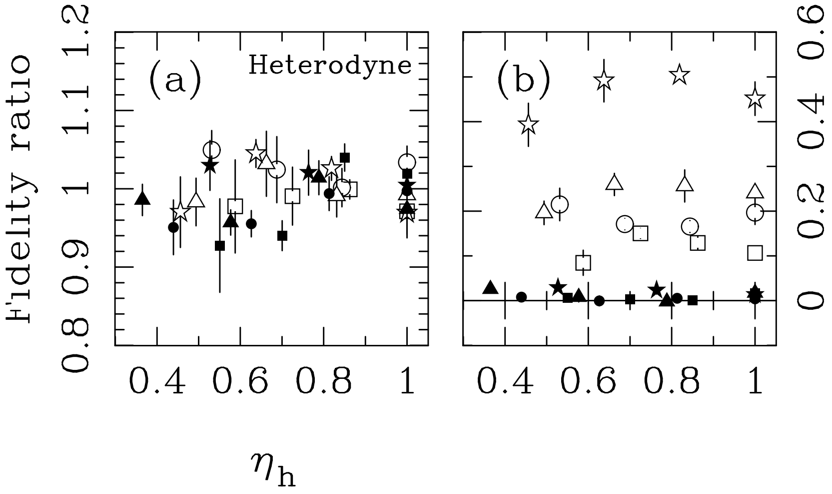

Figure 3.18: Fidelity ratio $\bar{F}/F_{\mathrm{th}}$ (see text) for heterodyne detection with quantum efficiency $\eta_r = 0.8$, 0.5, 0.3, and 0.1 (squares, circles, triangles, and stars, respectively). The open (solid) points are for $\overline{n} = 1$ ($\overline{n} = 100$) thermal photons per beam. The number of data used in each case is 2080 (4 blocks of 20 data samples for 26 settings of the phase ϕ).

3.4.2 Simulated experiments

In Fig. 3.18 we report results of the tomographically measured fidelity for heterodyne detection on beam 1. The numerical results are obtained by simulating the quadrature probability distribution pertaining to the reduced state (3.36), and averaging the kernel functions in Eq. (3.38). The simulation is performed according to the SR hypothesis, thus the homodyne probability distribution in Eq. (3.35) corresponds to state (3.36). Notice that for heterodyne detection the measurement spectrum is continuous and the probability $p^{\eta_r}(\alpha)\mathrm{d}\alpha$ of outcome α is infinitesimal. Therefore, we present the average value $\bar{F}$ of the fidelity $F(\alpha)$ over $p^{\eta_r}(\alpha)$. Results for various values of the quantum efficiencies η_r and η_h are reported along with two different values of the NOPA gain parameter ξ (given in terms of the number of thermal photons per beam $\overline{n} = |\xi|^2/(1-|\xi|^2)$). One can clearly see that a decisive test can be performed with samples of a few thousand measurements only. The error in the measurement, denoted by the vertical error bars, is rather insensitive to both quantum efficiencies and the NOPA gain in the considered range of values.

In Fig. 3.19 the tomographically measured fidelity is reported when direct photodetection is performed on beam 1. Here the simulation is achieved analogously to the previous case, but now using Eqs. (3.41) and (3.42). Results for various outcomes n are given with different values of η_h and $\overline{n}$. Again, the test can be performed with samples

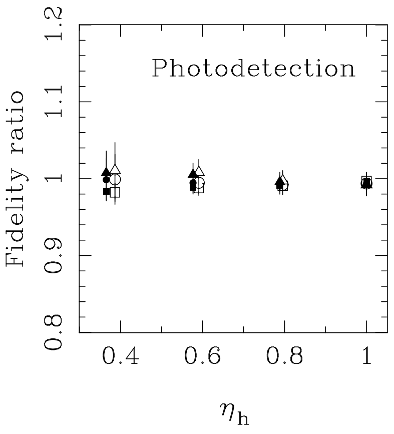

Figure 3.19: Fidelity ratio $F(n)/F_{\mathrm{th}}(n)$ (see text) for direct detection with quantum efficiency $\eta_r = 0.3$, resulting in outcomes $n = 0, 1$, and 2 at the photodetector (squares, circles, and triangles, respectively). The thermal photons per beam are $\overline{n} = 10$ (open points) and $\overline{n} = 100$ (solid points). In each case 10^4 data are used and the error bars are obtained by dividing the data into 10 blocks.

of a few thousand measurements only; the resulting error in the measurement is rather insensitive to the values of the experimental parameters.

3.4.3 Actual experiment

The actual experiment is in progress in Prem Kumar's group at Northwestern University in Chicago, and no real results are yet available. In our lab the NOPA consists of a type-II phase-matched KTP crystal that is pumped by the second harmonic of a Q-switched and mode-locked Nd:YAG laser. Previously, such a NOPA was employed, with parametric gains > 10 ($|\xi|^2 > 0.9$), to generate highly quantum-correlated twin beams of light at 1064 nm [80]. By appropriately choosing the input quantum state, a similar setup was then used to demonstrate the production of squeezed-vacuum state with a high degree (5.8 ± 0.2 dB) of squeezing [81]. In the present context, the twin beams, which are easily separable because of their orthogonal polarizations resulting from type-II phase matching, can be separately detected; beam 2 with a homodyne detector for detecting the reduced quantum state and beam 1 with either a heterodyne detector or a photon-counting detector. We have recently reported preliminary results of double homodyne measurements [82], which were performed to reconstruct the joint photon-number density matrix of the twin-beam state [83]. The main challenge in the present experiment is the achievement of high degrees of overlap (mode-matching efficiency) between the down-converted and the LO modes. Such overlap is non-trivial in pulsed, traveling-wave experiments owing to the distortion of the down-converted modes that is caused by the spatio-temporally Gaussian profile of the pump beam. With suitable choice of LOs, however, we have previously obtained $\eta_h > 0.70$ [84], an adequate value for the present experiment (cf. Figs. 3.18 and 3.19).

3.4.4 Conclusions

In conclusion, we have presented an experiment to test the rule of state reduction upon quantum measurements. Our goal is achieved by changing the kind of measurement performed on one beam of a pair of twin beams. The reduced state of the other beam, which depends on the kind of measurement performed, is then experimentally observed through a measurement of the fidelity between the theoretically expected reduced state and the experimental state. The fidelity is measured directly by optical homodyne tomography, within the validity bounds of quantum efficiency at the various detectors. We decided to present the test of SR in terms of the fidelity for illustrative purposes. However, the same test can be performed by tomographic reconstruction of the whole density matrix of the reduced state, without any modification in the schematic of the experiment.

3.5 Test of Bell's inequalities

In this section we present[4] [54, 85] a homodyne detection scheme to verify Bell's inequality on correlated optical beams at the output of a non-degenerate parametric amplifier. Our approach is based on tomographic measurement of the joint detection probabilities, which allows high quantum efficiency at detectors. The conventional homodyne scheme (see Sect. 2.1) is abandoned for a self-homodyne scheme which simplifies the experimental setup.

In 1935 Einstein, Podolsky and Rosen (EPR) [86] proved the incompatibility among three hypotheses: 1) quantum mechanics is correct; 2) quantum mechanics is complete; 3) the following criterion of local reality holds: "If, without in any way disturbing a system, we can predict with certainty [...] the value of a physical quantity, then there exists an element of physical reality corresponding to this quantity." The paper opened a long and as yet unsettled debate about which one of the three hypotheses should be discarded. While Einstein suggested to abandon the completeness of quantum mechanics, Bohr [87] refused the criterion of reality. The most important step forward in this debate was Bell's theorem of 1964 [88], which proved that there is an intrinsic incompatibility between the assumptions 1) and 3), namely the correctness of quantum mechanics and Einstein's "criterion of reality". In Bell's approach, a source produces a pair of correlated particles, which travel along opposite directions and impinge into two

---

[4] This work also has been supported by the PRA–CAT97 of the INFM.

detectors. The two detectors measure two dichotomic observables $A(\alpha)$ and $B(\beta)$ respectively, α and β denoting experimental parameters which can be varied over different trials, typically the polarization/spin angle of detection at each apparatus. Assuming that each measurement outcome is determined by the experimental parameters α and β and by an "element of reality" or "hidden variable" λ (which cannot be known to the observer), Bell proved an inequality which holds for any theory that satisfies Einstein's "criterion of reality", while it is violated by quantum mechanics. Such a fundamental inequality, which allows an experimental discrimination between local hidden–variable theories and quantum mechanics, has been the focus of interest in a number of experimental works [89]. Unfortunately, Bell's proof is based on two conditions which are difficult to achieve experimentally. The first is the feasibility of an experimental configuration yielding perfect correlation; the second is the possibility of approaching an ideal measurement, which itself does not add randomness to the outcome. Since 1969, attention was focused on improving the correlation of the source on one hand, and, on the other, on deriving more general inequalities that take into account detection quantum efficiency or circumvent the problem, however, at the cost of introducing supplementary hypotheses (see Refs. [90]), as the well known "fair sampling" assumption. Anyhow it was clear also to the authors of the same Refs. [90] that these assumptions are questionable, and, as a matter of fact, it was proved [91] that in all performed experimental checks the results can be reproduced in the context of Einstein's assumptions if quantum efficiency of detectors is less than 82.3%.

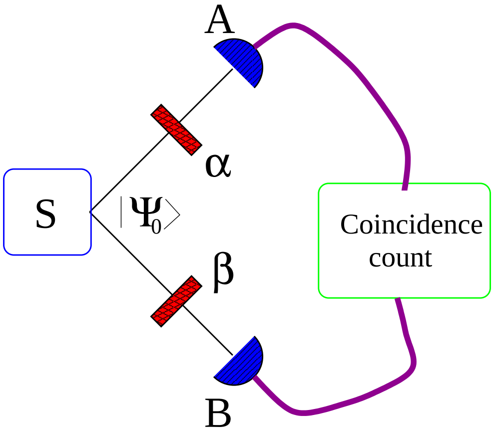

Figure 3.20: Typical experiment for the test of Bell's inequalities using photons. The source S emits polarization–correlated photons (indicated by state $|\Psi_0\rangle$), that are filtered by the polarizers with angles α and β. The detectors A and B measure the presence or absence of photons. This highly idealized experiment would work only with high–efficiency single photon resolving detectors and lossless polarizers.

In a typical idealized experiment, shown in Fig. 3.20, the source emits a pair of polarization correlated photons and two detectors (A and B) separately check the presence of the two photons after polarizing filters at angles α and β, respectively. Alternatively, one can use four photodetectors with polarizing beam splitters in front, with the advantage of checking through coincidence counts that photons come in pairs. Denote by $p_{\alpha,\beta}$ the joint probability of finding one photon at each detector with polarization angle α and β, respectively, and denote by $\bar{\alpha}$ and $\bar{\beta}$ the polarization angles orthogonal to α and β. The correlation function between photon polarization and detector clicks is then given by

$$C(\alpha,\beta)=p_{\alpha,\beta}+p_{\bar{\alpha},\bar{\beta}}-p_{\bar{\alpha},\beta}-p_{\alpha,\bar{\beta}}\ , \tag{3.44}$$

which will be $C(\alpha,\beta)=1$ if photons in A and B have always polarization both parallel or both orthogonal to α and β respectively, and $C(\alpha,\beta)=-1$ if one of them has polarization always orthogonal to its polarizer, while the other one always parallel.

Bell's inequality [88] will now be briefly derived following [92]. In the realistic local hidden variables hypothesis, each detector click can only be determined by the local polarizer orientation and by a set of variables λ "hidden" to the observer. Hence, the correlation function $C(\alpha,\beta)$ must be an average, with an unknown weight function $w(\lambda)$, of the type

$$C(\alpha,\beta)=\int d\lambda\ w(\lambda)A(\alpha,\lambda)B(\beta,\lambda)\ , \tag{3.45}$$

where $A(\alpha,\lambda)=+1$ and $A(\alpha,\lambda)=-1$ indicate respectively a "click" and a "no click" event in detector A, and analogously for B. Notice that from the locality hypothesis it follows that the value of A must be independent of β, and from the reality hypothesis it follows that A has a determined value for any value of α (even if α is different from the one the observer is using in the experimental run). By using (3.45), we can write

$$\begin{aligned}|C(\alpha,\beta)-C(\alpha,\beta')|&=\left|\int d\lambda\ w(\lambda)A(\alpha,\lambda)\left(B(\beta,\lambda)-B(\beta',\lambda)\right)\right|\\ \leqslant\int d\lambda\ w(\lambda)\left|A\left(B(\beta,\lambda)-B(\beta',\lambda)\right)\right|&=\int d\lambda\ w(\lambda)\left|\left(B(\beta,\lambda)-B(\beta',\lambda)\right)\right|,\end{aligned} \tag{3.46}$$

and analogously

$$|C(\alpha',\beta)+C(\alpha',\beta')|\leqslant\int d\lambda\ w(\lambda)\left|\left(B(\beta,\lambda)+B(\beta',\lambda)\right)\right|. \tag{3.47}$$

Finally, since $\int d\lambda\ w(\lambda)=1$ and $B(\beta,\lambda)=\pm1$ for any β and λ, we obtain Bell's inequality from the sum of (3.46) and (3.47)

$$\Gamma(\alpha,\beta,\alpha',\beta')\overset{\text{def}}{=}|C(\alpha,\beta)-C(\alpha,\beta')|+|C(\alpha',\beta')+C(\alpha',\beta)|\leqslant 2\ . \tag{3.48}$$

It is well known that, with an appropriate choice of angles, quantum mechanics predicts that $\Gamma(0, \frac{3}{8}\pi, \frac{\pi}{4}, \frac{\pi}{8}) = 2\sqrt{2}$. Thus, from Bell's inequality it is possible to experimentally discriminate between Quantum Mechanics and local realistic theories. This is a typical example of experiment capable of discriminating between two concurrent theories, by falsifying one of the two: such experiments play a decisive role in epistemology.

In this section we propose a new kind of test for Bell's inequality based on quantum homodyne tomography. In our setup the photodetectors are replaced by homodyne detectors, which along with the tomographic technique can be regarded as a black box for measuring the joint probabilities $p_{\alpha,\beta}$. Since all quantum correlations are recovered, it is not even necessary to use the polarization filters (that were labelled α and β in Fig. 3.20). It has been objected that in this case there is no "actually performed" photodetections as in the ideal experiment, outlined previously. With homodyne tomography one infers the violation of the inequality which would occur if one had hypothetical high efficiency photodetectors starting from the homodyne data. However, in practice one only needs the photon number distributions $p_{\alpha,\beta}$, in order to verify the violation and homodyne tomography can measure these directly, without having to collect any single–photon–event statistics. Another objection which has been raised is that the tomography technique relies heavily on the correctness of Quantum Mechanics, and that an experiment that could bring to its falsification should not be based on it. We do not think that this objection can be overcome, but it should be noted that almost all Bell inequality violation experiments carried out so far are based on photon detection correlation and hence also rely on the correctness of Quantum Mechanics at least as far as the quantization of radiation modes is involved. In fact, both EPR's and Bell's argument deal with particles and associated spins. The homodyne reconstruction must be considered, just like the direct photodetection, like a "black box" which outputs the needed data[5]. The main advantage of the tomographic test is that it allows using linear photodiodes with quantum efficiency η higher than 90% [22]. On the other hand, the method works effectively even with η as low as 70%, without the need of a "fair sampling" assumption, since all data are collected in a single experimental run and no supplementary "normalization runs" are needed. With respect to the customary homodyne technique, which in the present case would need many beam splitters and local oscillators (LO) that are coherent each other, the setup is greatly simplified by using the recent self-homodyne technique [23]. Another advantage of self-homodyning is the more efficient signal-LO mode-matching, with improved overall quantum efficiency.

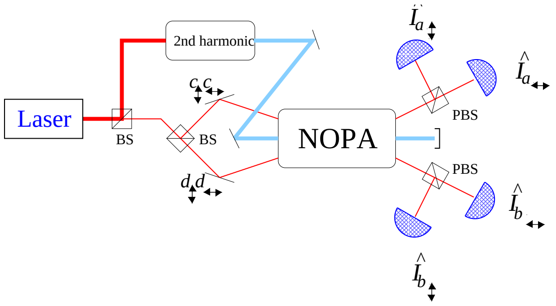

Figure 3.21: Experimental setup for the tomographic test of Bell's inequality. PBS and BS denote 'polarizing beam splitter' and 'conventional 50–50 beam splitter' respectively. Input radiation modes $c_\updownarrow$, $c_\leftrightarrow$, $d_\updownarrow$, $d_\leftrightarrow$ (at laser frequency ω_0) are in a coherent state, while modes $a_\updownarrow$, $b_\leftrightarrow$, $a_\leftrightarrow$ and $b_\updownarrow$, whose spectrum is composed the two frequency components at $\omega_0 + \Omega$ and $\omega_0 - \Omega$ (Ω in the radiofrequency regime) are in the vacuum state. At the output of the non-degenerate parametric amplifier (NOPA) the four photocurrents I at radiofrequency Ω are measured, yielding the value of quadratures of the field modes $a_\updownarrow$, $b_\leftrightarrow$, $a_\leftrightarrow$ and $b_\updownarrow$. The outcome quadratures are then used to reconstruct the probabilities of interest through quantum tomography.

3.5.1 Experimental apparatus

We will now describe the self–homodyne experimental setup, described in Fig. 3.21. The apparatus for generating the correlated beams is a $\chi^{(2)}$ nonlinear crystal, cut for Type-II phase–matching, acting as a non-degenerate optical parametric amplifier (NOPA). The NOPA is injected with excited coherent states (see Fig. 3.21) in modes $c_\leftrightarrow, c_\updownarrow, d_\leftrightarrow, d_\updownarrow$ all with equal intensities and at the same frequency ω_0, c and d denoting mode operators for the two different wave-vector directions, and $\updownarrow$ and $\leftrightarrow$ representing vertical and horizontal polarization, respectively. The NOPA is pumped at the second harmonic $2\omega_0$. At the output of the amplifier four photodetectors separately measure the intensities $I_{a_\updownarrow}$, $I_{b_\leftrightarrow}$, $I_{a_\leftrightarrow}$, $I_{b_\updownarrow}$ of the mutual orthogonal polarization components of the fields propagating at different wave vectors. A narrow band of the photocurrent is selected, centered around frequency $\Omega \ll \omega_0$ (typically ω_0 is optical/infrared, whereas Ω is a radio frequency). In the process of direct detection, the central modes $c_{\updownarrow,\leftrightarrow}$ and $d_{\updownarrow,\leftrightarrow}$ beat with $\omega_0 \pm \Omega$ sidebands, thus playing the role of the LO of homodyne detectors. The four photocurrents $I_{a_\updownarrow}$, $I_{b_\leftrightarrow}$, $I_{a_\leftrightarrow}$, $I_{b_\updownarrow}$ yield the value of the quadratures

---

[5] The substantial difference is that, using homodyne tomography, there are no classical time–like separated events (as, for example, detector clicks) whose correlations cannot be explained in a classical local-hidden-variables framework.

of the four modes [23]

$$a_\pi = \frac{1}{\sqrt{2}}\Big(a_\pi(+)+a_\pi(-)\Big)\ ;\quad b_\pi = \frac{1}{\sqrt{2}}\Big(b_\pi(+)+b_\pi(-)\Big)\ ,\quad \pi=\{\leftrightarrow,\updownarrow\} \tag{3.49}$$

where $a_\pi(\pm)$ and $b_\pi(\pm)$ denote the sideband modes at frequency $\omega_0 \pm \Omega$, which are in the vacuum state at the input of the NOPA. Thus, modes a and b have a spectrum with two frequency components at $\omega_0+\Omega$ and $\omega_0-\Omega$. In the quadrature x_ϕ, defined in (1.9), the phase ϕ is the relative phase between the signal and the LO. The value of the quadratures is used as input data for the tomographic measurement of the correlation function $C(\alpha,\beta)$. The direction of polarizers (α,β) in the experimental setup does not need to be varied over different trials, because, as we will show in the following, such direction can be changed tomographically, *i.e.* at the data analysis stage.

3.5.2 Analysis of the setup

We will now enter into details on the state at the output of the NOPA and on the tomographic detection. In terms of the field modes in Eq. (3.49) the spontaneous down-conversion at the NOPA is described by the unitary evolution operator

$$U(\xi)=\exp\left[\xi\left(a^\dagger_\updownarrow b^\dagger_\leftrightarrow + e^{i\varphi}a^\dagger_\leftrightarrow b^\dagger_\updownarrow\right) - \text{h. c.}\right]\ , \tag{3.50}$$

where $\xi = \chi^{(2)}\gamma L/c$ is a rescaled interaction time written in terms of the nonlinear susceptibility $\chi^{(2)}$ of the medium, the crystal length L, the pump amplitude γ and the speed c of light in the medium, whereas φ represents the relative phase between the orthogonal polarization components of the pump field. The state at the output of the NOPA, for vacuum input, then writes as follows

$$|\psi\rangle \;=\; (1-|\Lambda|^2)\sum_{n=0}^{\infty}\sum_{m=0}^{\infty}\Lambda^{n+m}e^{i\varphi m}|n,n,m,m\rangle \equiv |\psi_{1,2}\rangle\otimes|\psi_{3,4}\rangle\ , \tag{3.51}$$

where $\Lambda = (\xi/|\xi|)\ \tanh|\xi|$ and $|i,l,m,n\rangle$ represents the common eigenvector of the number operators of modes $a_\updownarrow$, $b_\leftrightarrow$, $a_\leftrightarrow$, $b_\updownarrow$, with eigenvalues i,l,m and n, respectively. The four-mode state vector in Eq. (3.51) factorizes into a couple of twin beams $|\psi_{1,2}\rangle$ and $|\psi_{3,4}\rangle$, each one entangling a couple of spatially divergent modes ($a_\updownarrow$, $b_\leftrightarrow$ and $a_\leftrightarrow$, $b_\updownarrow$, respectively).

Notice that conventional experiments, concerning a two-photon polarization-entangled state generated by spontaneous down-conversion, consider a four-mode entangled state which corresponds to keeping only the first-order terms of the sums in Eq. (3.51), and to ignoring the vacuum component, as only intensity correlations are usually measured. Here, on the contrary, we measure the joint probabilities on the state (3.51) to test Bell's inequality through homodyne tomography, which yields the value of $\Gamma(\alpha,\beta,\alpha',\beta')$ in Eq. (3.48). As a matter of fact, as shown in Chap. 1, the tomographic technique is a kind of universal detector, which can measure any observable

O of the field. As is evident from the tomography theorem given in page 29, for factorized many-mode operators $O = O_1 \otimes O_2 \otimes \cdots \otimes O_n$ the pattern function that is to be averaged is just the product of those corresponding to each single-mode operator $O_1, \cdots, O_n$ labelled by variables $(x_1, \phi_1), \cdots, (x_n, \phi_n)$. By linearity the pattern function is extended to generic many-mode operators.

Now we consider which observables are involved in testing Bell's inequality (3.48). Let us denote by $p_{\alpha,\beta}(i, l, m, n)$ the probability of having i, l, m, n photons in modes $a_\updownarrow, b_\leftrightarrow, a_\leftrightarrow, b_\updownarrow$ for the "rotated" state

$$|\psi\rangle_{\alpha,\beta} \equiv U_{1,3}(\alpha) U_{2,4}(\beta) |\psi\rangle \ , \tag{3.52}$$

$U_{1,3}(\alpha)$ and $U_{2,4}(\beta)$ being the unitary operators which describe a polarization rotation

$$U_{1,3}(\alpha) = \exp\left[\alpha\left(a^\dagger_\updownarrow a_\leftrightarrow - a_\updownarrow a^\dagger_\leftrightarrow\right)\right] \ , \tag{3.53}$$

$$U_{2,4}(\beta) = \exp\left[\beta\left(b^\dagger_\updownarrow b_\leftrightarrow - b_\updownarrow b^\dagger_\leftrightarrow\right)\right] \ . \tag{3.54}$$

The probabilities in Eq. (3.44) can be written as $p_{\alpha,\beta}=p_{\alpha,\beta}(1,1)$, $p_{\bar{\alpha},\bar{\beta}}=p_{\alpha,\beta}(0,0)$, $p_{\bar{\alpha},\beta}=p_{\alpha,\beta}(0,1)$, and $p_{\alpha,\bar{\beta}}=p_{\alpha,\beta}(1,0)$, with

$$p_{\alpha,\beta}(n,m) = \frac{p_{\alpha,\beta}(n, 1-m, 1-n, m)}{P(1,1)} \ , \tag{3.55}$$

and $\{n, m = 0, 1\}$. The denominator $P(1,1)$ in Eq. (3.55) represents the absolute probability of having at the output of the NOPA one photon in modes $a_\updownarrow, a_\leftrightarrow$ and one photon in modes $b_\updownarrow, b_\leftrightarrow$, independently on the polarization, namely

$$P(1,1) = \sum_{n=0,1} \sum_{m=0,1} p_{\alpha,\beta}(n, 1-m, 1-n, m) \ . \tag{3.56}$$

Notice that our procedure does not need a fair sampling assumption, since we measure in only one run, both the numerator and the denominator of Eq. (3.55), namely we do not have to collect auxiliary data to normalize probabilities. On the other hand, since we can exploit quantum efficiencies as high as $\eta = 90\%$ or more, and the tomographic pattern functions already take into account η, we do not need supplementary hypothesis for it.

The observables that correspond to probabilities $p_{\alpha,\beta}(i, l, m, n)$ in Eqs. (3.55) and (3.56) are the projectors

$$\begin{aligned} &|\, i, l, m, n\rangle_{\alpha,\beta} \ \ {}_{\alpha,\beta}\langle\, i, l, m, n| \\ &= U^\dagger_{1,3}(\alpha)\, U^\dagger_{2,4}(\beta)\, |\, i, l, m, n\rangle\langle\, i, l, m, n|\, U_{2,4}(\beta)\, U_{1,3}(\alpha) \ . \end{aligned} \tag{3.57}$$

After a straightforward calculation using Eqs. (3.55), (3.56) and (3.57), one obtains that $P(1,1)$ is measured through the following average $\mathcal{AV}$ of homodyne data

$$P(1,1) = \mathcal{AV}\left\{\left(K^1_1\, K^3_0 + K^1_0\, K^3_1\right)\left(K^2_1\, K^4_0 + K^2_0\, K^4_1\right)\right\} \ , \tag{3.58}$$

where K^j_n denotes the diagonal ($n = 0, 1$) tomographic kernel function for mode j, namely

$$K^j_n \equiv \langle n|K_\eta(x - x_{\phi_j})|n\rangle \; . \tag{3.59}$$

The probabilities in the numerator of Eq. (3.55) are given by the average of a lengthy expression, which depends on both the diagonal terms (3.59) and the following off-diagonal terms

$$K^j_+ \equiv \langle 0|K_\eta(x - x_{\phi_j})|1\rangle \; , \quad K^j_- \equiv \langle 1|K_\eta(x - x_{\phi_j})|0\rangle = (K^j_+)^* \; . \tag{3.60}$$

Here we report the final expression for $C(\alpha, \beta)$ of Eq. (3.44)

$$\begin{aligned} C(\alpha,\beta) = \mathcal{AV}\Big\{ & [\cos(2\alpha)\left(K^1_1 K^3_0 - K^1_0 K^3_1\right) + \sin(2\alpha)\left(K^1_+ K^3_- + K^1_- K^3_+\right)] \\ & \times[\cos(2\beta)\left(K^2_0 K^4_1 - K^2_1 K^4_0\right) + \sin(2\beta)\left(K^2_+ K^4_- + K^2_- K^4_+\right)]\Big\}/P(1,1) \, . \end{aligned} \tag{3.61}$$

Caution must be taken in the estimation of the statistical error, because $C(\alpha, \beta)$—and thus $\Gamma(\alpha, \beta, \alpha', \beta')$ in Eq. (3.48)—are non linear averages (they are ratios of averages). The error bar is obtained from the variance calculated using some statistical data computed via a Monte Carlo simulation, starting from the estimated distribution of the experimental data (which, since we give a simulation of the experiment, is also simulated). Refer to Sect. 1.2.4 for the description of the procedure to evaluate error bars starting from poor statistics, as we have here where the tomographic means converge very slowly. In fact, since the nonlinearity of Γ introduces a systematic error which is vanishingly small for increasingly larger sets of data, the estimated mean value of Γ should be obtained from the full set of data, instead of averaging the mean value of blocks.

3.5.3 Monte Carlo Simulations

We now present some numerical results obtained from Monte–Carlo simulations of the proposed experiment.

For the simulation we use the theoretical homodyne probability pertaining to the state $|\psi\rangle$ in Eq. (3.51) which, for each factor $|\psi_{i,j}\rangle$, is given by

$$p_\eta(x_i, x_j; \phi_i, \phi_j) = \frac{2\exp\left[-\frac{(x_i+x_j)^2}{d^2_{z_{ij}}+4\Delta^2_\eta} - \frac{(x_i-x_j)^2}{d^2_{-z_{ij}}+4\Delta^2_\eta}\right]}{\pi\sqrt{(d^2_{z_{ij}} + 4\Delta^2_\eta)(d^2_{-z_{ij}} + 4\Delta^2_\eta)}} \; , \tag{3.62}$$

where x_i ($i = 1, 2, 3, 4$) is the outcome of the homodyne measurement for quadrature of the i-th mode at phase ϕ_i, and

$$z_{ij} = e^{-i(\phi_i+\phi_j)}\Lambda \; , \qquad d^2_{\pm z_{ij}} = \frac{|1 \pm z_{ij}|^2}{1 - |z_{ij}|^2} \; . \qquad \Delta^2_\eta = \frac{1-\eta}{4\eta} \; . \tag{3.63}$$

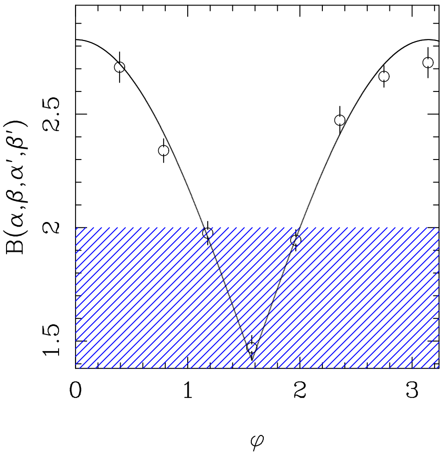

Figure 3.22: Plot of $\Gamma(\alpha,\beta,\alpha',\beta')$ *vs.* the phase φ in the state of Eq. (3.51) for a simulated experiment. The shaded area represents the classical region for Γ, while the curve represents the QM prediction. The parameters of the simulation are: $\alpha = 0$; $\beta = \frac{3}{8}\pi$; $\alpha' = \frac{\pi}{4}$; $\beta' = \frac{\pi}{8}$; quantum efficiency $\eta = 85\%$; $\Lambda = .5$ (see Eq. (3.51)). A total number of 10^6 homodyne data (divided into 20 statistical blocks) has been used.

In Fig. 3.22 we present the simulation results for Γ in Eq. (3.48) *vs* the phase φ in the state of Eq. (3.51). The full line represents the value of Γ in Eq. (3.48) with the quantum theoretical value $C(\alpha,\beta)$ given by

$$C(\alpha,\beta) = \cos\varphi \sin 2\alpha \sin 2\beta - \cos 2\alpha \cos 2\beta \; . \tag{3.64}$$

Quantum efficiency $\eta = 85\%$ has been used, nonetheless notice that for $\varphi = 2\pi$ (corresponding to a maximum violation with respect to the classical bound 2), the obtained value is over 10 σ distant from the bound. By increasing the number of homodyne data, it is possible to obtain good results also for lower quantum efficiency. In fact, by increasing the number of data to $8 \cdot 10^8$, a value of $\Gamma(0, \frac{3}{8}\pi, \frac{\pi}{4}, \frac{\pi}{8}) = 2.834 \pm 0.268$ has been obtained for $\Lambda = .5$, $\varphi = 2\pi$, and η as low as 65%. This result is to be compared with the quantum theoretical value of $2\sqrt{2} \simeq 2.828$.

In Fig. 3.23 the results of the measurement of Γ, for different simulated experiments using the same number of data, are presented for different detector efficiencies η. Notice how the error bars decrease *vs* η.

3.5.4 Conclusions

In conclusion in this section we have proposed a test of Bell's inequality, based on self–homodyne tomography. We have presented the objections that were raised upon the presentation of such a device. The rather simple experimental apparatus is mainly com-

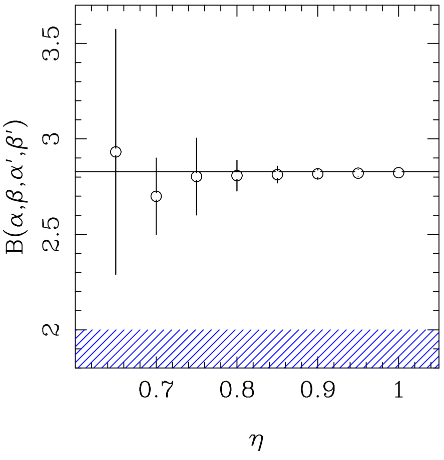

Figure 3.23: Plot of $\Gamma(\alpha,\beta,\alpha',\beta')$ *vs.* the quantum efficiency of the detectors for a series of simulated experiments. The shaded area represents the classical region for Γ, while the horizontal line is the QM prediction $2\sqrt{2}$. The parameters of the simulations are: $\alpha = 0$; $\beta = \frac{3}{8}\pi$; $\alpha' = \frac{\pi}{4}$; $\beta' = \frac{\pi}{8}$; $\varphi = \pi$; $\Lambda = .5$. A total number of $6 \cdot 10^7$ homodyne data (in 20 statistical blocks) has been used for each simulation.

posed of a NOPA medium and four photodiodes. The experimental data are collected through a self–homodyne scheme and processed by quantum tomography. No supplementary hypotheses, such as the 'fair sampling' assumption, are introduced, quantum efficiencies η as high as 90% are currently available, and, anyway, η as low as 70% is tolerated for $10^6 \div 10^7$ experimental data. We have presented some numerical results based on Monte–Carlo simulations that confirm the feasibility of the experiment, showing violations of Bell's inequality for over 10 σ with detector quantum efficiency $\eta = 85\%$.

3.6 Tomography of the Fock state

In this section we present [93] a feasibility study for an experiment which is currently being carried out by Prof. De Martini and his group at Roma "La Sapienza" University. I acknowledge useful discussions with Prof. De Martini and his students. Two experiments for the generation and tomographic detection of radiation Fock states are analyzed. The two experimental setups differ at the conditional photodetector. In the first case a nonlinear high efficiency photodetector is used, it is hence impossible to determine the number of impinging photons. In the second case a linear single photon resolving detector is needed, however with low efficiency η. The reconstruction method which was presented in Sect. 3.3 can thus be adapted to this second scheme, in order to compensate the quantum efficiency of the conditional detector.

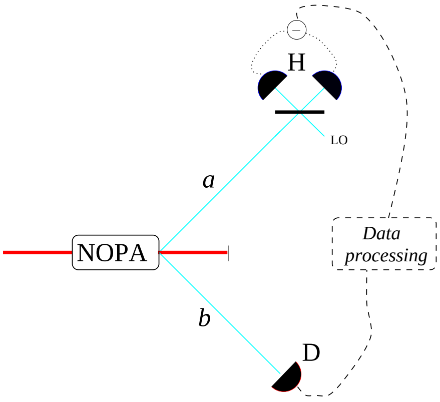

Figure 3.24: Experimental scheme for the generation and detection of Fock states. Modes a and b exit a non degenerate optical parametric amplifier (NOPA). Mode a is reduced to a number state by the conditional photodetector D, while mode a is fed into the homodyne detector H.

3.6.1 Scheme for generating and detecting Fock states

The scheme for generating Fock states we consider in this section is shown in Fig. 3.24. It is again based on the state reduction of the twin-beam state exiting a non degenerate optical amplifier (NOPA). The NOPA is described by the interaction Hamiltonian

$$H = -ir(a^\dagger b^\dagger - ab) \ , \qquad (3.65)$$

where a and b represent the two output modes, and r is the gain parameter. As already pointed out in Sect. 3.4, the output state for vacuum NOPA input is given by Eq. (3.27), *i.e.*

$$|\Psi\rangle = (1-|\xi|^2)^{1/2} \sum_{n=0}^{\infty} \xi^n |n\rangle_a |n\rangle_b \ , \qquad (3.66)$$

where $\xi = -\tanh r$. A conditional photodetector D is placed at mode b to measure the number of photons. As a consequence of this measurement, in the ideal case of a perfect photodetector D (*i.e.* with unit quantum efficiency $\eta_D = 100\%$), mode a is left in the Fock state $|m\rangle$, where m is the result at D. On the other hand, the realistic process of inefficient photodetection ($\eta_D < 100\%$) can be described (in the Mandel, Kelley, Kleiner approach [38]) as a perfect ($\eta = 100\%$) detector preceded by a beam splitter (BS) with transmissivity η_D. The action of the BS on the state $|\Psi\rangle$ is given by

$$e^{-\xi}(|\Psi\rangle\langle\Psi|) = (1-|\xi|^2) \sum_{m,n=0}^{\infty} \xi^n \xi^{*m} |n\rangle_{aa}\langle m| \otimes e^{-\xi}(|n\rangle_{bb}\langle m|) \ , \qquad (3.67)$$

where the BS superoperator $e^{-\xi}$ acts as follows

$$\begin{aligned} e^{-\xi}(|n\rangle_{bb}\langle m|) &= \eta_D^{1/2(n+m)} \sum_{p=0}^{min(n,m)} \begin{pmatrix} n \\ p \end{pmatrix}^{1/2} \begin{pmatrix} m \\ p \end{pmatrix}^{1/2} \\ &\quad \times (\eta_D^{-1} - 1)^p |n-p\rangle_{bb}\langle m-p| \ . \end{aligned} \tag{3.68}$$

Assuming that we detect n photons at mode b, the reduced state at mode a is given by

$$\rho_n = \frac{1}{p_n} \mathrm{Tr}_b \left[\mathbb{1}_a \otimes |n\rangle_{bb}\langle n| e^{-\xi} \left(|\Psi\rangle\langle\Psi| \right) \right] \ . \tag{3.69}$$

and

$$p_n = \mathrm{Tr}_{ab} \left[\mathbb{1}_a \otimes |n\rangle_{bb}\langle n| e^{-\xi} \left(|\Psi\rangle\langle\Psi| \right) \right] = \frac{N^n}{(N+1)^{n+1}} \tag{3.70}$$

(with $N = \eta_D|\xi|^2/(1-|\xi|^2)$) is the probability of detecting n photons. The state in mode a is thus given by the following mixture of Fock states

$$\rho_n = \frac{1}{p_n}(1-|\xi|^2) \sum_{k=n}^{\infty} \begin{pmatrix} k \\ n \end{pmatrix} \eta_D^n (1-\eta_D)^{k-n} |\xi|^{2k} |k\rangle\langle k| \ . \tag{3.71}$$

The density operator of mode a now should be detected by means of homodyne tomography, where each experimental datum (*i.e.* homodyne outcome) is processed separately, and no experimental histograms are useful to reconstruct the density matrix. Thus, it is important to set the boxcar integrator at the output of the system appropriately: no average must be performed on the experimental data.

3.6.2 Nonlinear single photon detection

In this paragraph we analyze the proposed experiment when the photodetector at mode b is a nonlinear single photon detector, namely it can discriminate only between the vacuum and all the other Fock states (*i.e.* between absence and presence of photons). In order to have a definite Fock state as the outcome of the tomographic reconstruction, it is necessary that the probability of having in mode b other Fock states than the one we're interested in, is negligible. If this is not the case, a systematic error is performed, since the corresponding state in mode a is the statistical mixture (3.71). In order to reduce the systematic error one should take a low gain parameter ξ, so that the probability of having more than one photon in each mode is negligible. In this way only the Fock state $|1\rangle$ can be reconstructed. As an example, we show in Fig. 3.26 a simulation of a tomographic reconstruction of the Wigner function and the corresponding photon number probability distribution for the Fock state $|1\rangle$. As we can see, since the value of the gain is very low, the Wigner function is practically indistinguishable from the theoretical one, shown in Fig. 3.25, and the experiment is very successful.

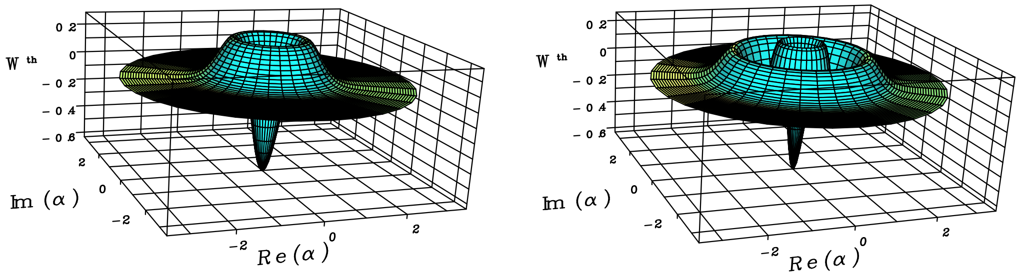

Figure 3.25: Theoretical Wigner function for the Fock state $|1\rangle$ and $|3\rangle$ respectively.

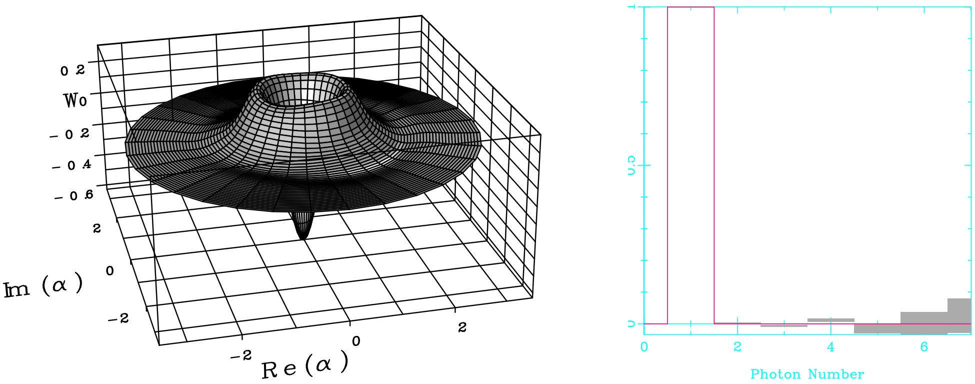

Figure 3.26: Simulation of a tomographic reconstruction of the Wigner function and photon number distribution for the Fock state $|1\rangle$. The parameters for this simulation are $\eta_D = 15\%$, $\eta_h = 75\%$, $\xi = .0036$. 10^5 experimental homodyne data have been used for 100 different phases, from a total of 10^7 data.

In order to reconstruct more excited Fock states, the detection scheme needs to be slightly modified. For example, to reconstruct Fock state $|2\rangle$ it is possible to use a beam splitter in mode b and one detector for each of the beam splitter's output modes, as shown in Fig. 3.27. We know that if both detectors produce a click, a state with more than one photon is present. Of course two (or more) photons may be present even if there is only one click: these cases (half of the events corresponding to the presence of two photons) will be neglected and do not contribute to the reconstruction. It is also important to keep the probability of having more than two photons as small as possible by keeping the gain ξ low, in order to avoid systematic errors. This procedure can, in principle, be generalized: to generate more excited Fock states $|n\rangle$ one can design a cascade of beam splitters and place a photodetector for each mode at the output of this sequence of beam splitters. However for more excited Fock states the systematic error increases, because the parameter ξ must be increased in order to have a non negligible probability of having Fock state $|n\rangle$. This implies that also the probability of having $|n+1\rangle$ is accordingly increased, since the ratio p_{n+1}/p_n is independent of n and is an increasing function of ξ.

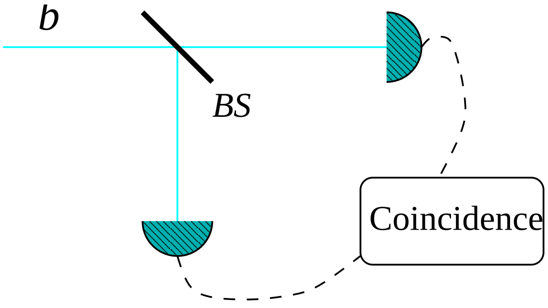

Figure 3.27: Scheme for the generation of the Fock state $|2\rangle$.

3.6.3 Linear single photon resolving detection

We will now analyze the case of a linear single photon resolving detection at mode b, namely a detector D that can discriminate among all Fock states. Notice that linear single photon detectors have, in general, smaller quantum efficiency η_D than nonlinear ones. However, as we will show here, it is more advantageous to use linear detectors, because it is possible to implement the reconstruction technique, which was derived in Sect. 3.2, that allows to compensate the effects of quantum efficiency of the conditioning photodetectors and to avoid systematic errors in the tomographic measurement. As we will see in the following, the method presented here is also more efficient than the previous for the detection of any Fock state because more experimental data can be used for the reconstruction. Moreover, by using this method one can increase the parameter ξ and thus detect also more excited Fock states.

The reconstruction algorithm is based on the inversion of the formula in Eq. (3.71), that rewrites as

$$p_n \rho_n = (1-|\xi|^2) \sum_{k=0}^{\infty} |\xi|^{2(n+k)} B_{nk} \; |k+n\rangle\langle k+n| \; , \tag{3.72}$$

where $B_{nk} = \begin{pmatrix} k+n \\ n \end{pmatrix} \eta_D^n (1-\eta_D)^k$. Thus, using the Bernoulli inversion derived in Eqs. (3.7) — (3.9), we have

$$|k\rangle\langle k| = \frac{1}{(1-|\xi|^2)|\xi|^{2k}} \sum_{n=0}^{\infty} (B^{-1})_{kn} \; p_{n+k} \rho_{n+k} \; , \tag{3.73}$$

with $(B^{-1})_{kn} = \begin{pmatrix} k+n \\ k \end{pmatrix} \left(1 - \frac{1}{\eta_D}\right)^n \eta_D^{-k}$.

In the experiment we propose here, Eq. (3.73) allows to reconstruct the Fock state $|k\rangle\langle k|$ as follows. Each density matrix ρ_{n+k} (corresponding to all photodetection outcomes with result $n+k$ at D) is tomographically reconstructed separately. The results for the different ρ_{n+k}'s are then combined according to Eq. (3.73). Notice that unlike conventional reconstruction techniques (where only the data relative to the Fock state of interest are kept), here all experimental outcomes with detected number of photons larger or equal to k are used, thus increasing the number of available data and the efficiency of the experiment.

Let us now analyze the convergence behavior of the series (3.73). The convergence radius is given by the condition

$$\left|\left(1 - \frac{1}{\eta_D}\right) \frac{N}{N+1}\right| \leqslant 1 \,, \tag{3.74}$$

which gives the following lower bound on the quantum efficiency η_D

$$\eta_D \geqslant \frac{1}{2} \frac{\sinh^2 r - 1}{\sinh^2 r} \,. \tag{3.75}$$

For values of η_D smaller than the above bound the series diverges and the present technique cannot be applied. Notice that for all values of r corresponding to $\sinh^2 r \leqslant 1$, *i.e.* $r \leqslant \frac{1}{2} \ln(3 + 2\sqrt{2})$, there is no lower bound on the quantum efficiency and at least not very excited Fock states can be successfully reconstructed even with very inefficient linear detectors. As we already pointed out in previous sections, unlike other compensation methods based on the inverse Bernoulli transformation [69], where the convergence radius of the procedure is $\eta > 50\%$, the present method works also for lower values of the quantum efficiency. The bound $\eta = 50\%$ is recovered for this method for the limiting case of $r \to \infty$, namely when the probability distribution p_n is flattened and therefore does not contribute to the convergence of the series (3.73).

In Fig. 3.28 we plot a simulated tomographic reconstruction of the Fock state $|3\rangle$ using the proposed reconstruction procedure given in Eq. (3.73). This is to be compared with the corresponding theoretical Wigner function shown in Fig. 3.25. As we can see, no systematic errors are present and the Wigner function is perfectly reconstructed.

A comment on the efficiency of the experimental scheme is now in order: to have an efficient reconstruction of more excited Fock states, *i.e.* to have a larger probability of detecting high numbers of photons at mode b, the gain of the NOPA must be increased. However, the convergence of the series (3.73) becomes slower for increasing r and this implies that η_D must also be increased in order to have a good reconstruction. Nevertheless, the present method still compares favorably with the one described in the previous subsection or with conventional schemes where no quantum efficiency compensation methods are used. As an example of comparison between the different methods,

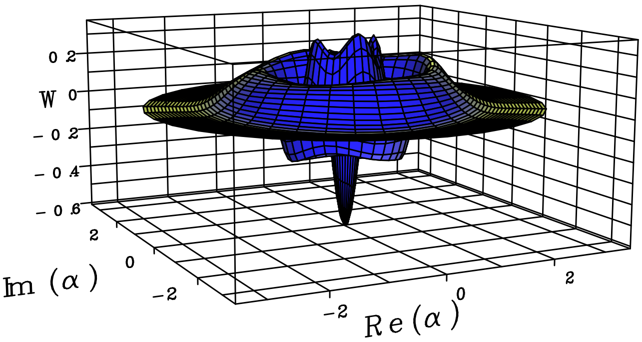

Figure 3.28: Simulation of a tomographic reconstruction of the Wigner function for the Fock state $|3\rangle$. The parameters for this simulation are $\eta_D = 30\%$, $\eta_h = 80\%$, $\xi = .4$. 10^6 experimental homodyne data have been used for 70 different phases, for a total of $7 \cdot 10^7$ data.

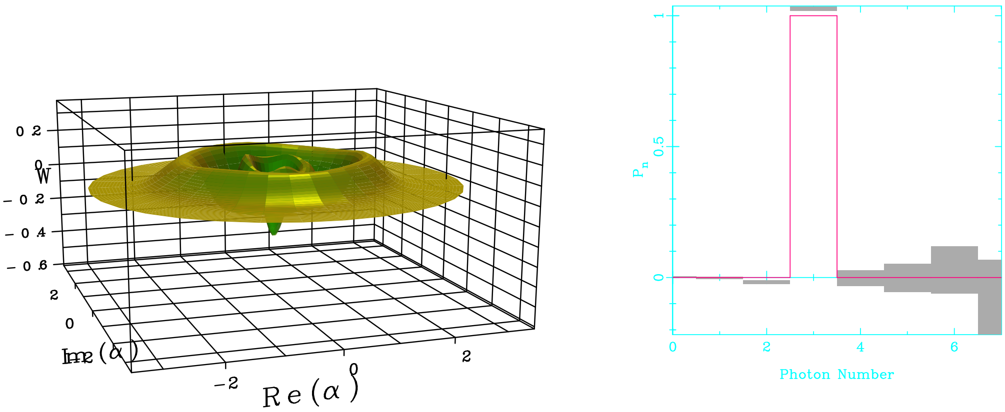

Figure 3.29: Same measurement as in Fig. 3.28, but without the use of the quantum efficiency deconvolution technique. The quantum characteristics of the state are washed out.

consider Fig. 3.29 where the same state measurement of Fig. 3.28 is presented without using the deconvolution technique. Notice how the quantum features of the Wigner function (*i.e.* its negative parts) are washed out.

3.6.4 Conclusions

In conclusion, in this section we presented a feasibility study for a tomographic state reconstruction experiment which was commissioned for an actual experiment, which is currently being carried out in Prof. De Martini's group. The deconvolution method which was presented in Sect. 3.2 has been here thoroughly analyzed and its validity limits (in terms of conditioning photodetector efficiency) derived. By using Monte Carlo simulations, its effects on the reconstructed state have been compared to analogous experiments that do not make use of such a technique.

Chapter 4

Conclusions

Here we give the conclusions and the possible further developments of the tomographic framework that was presented in this thesis.

In this thesis the theory of quantum state reconstruction was analyzed using group theory. The practical mathematical-statistical techniques needed to implement a tomography experiment were also given, along with noise deconvolution and adaptive tomographic techniques. These allow to achieve good tomographic reconstructions even when using data coming from inefficient detectors and lossy devices, and when using little number of data in the reconstruction.

The description of three different state reconstruction procedures was given, namely homodyne, spin and Kerr tomography. Homodyne and Kerr tomography are state reconstruction techniques for the quantized modes of the electromagnetic field. Notice that since the electromagnetic radiation is treated like an harmonic oscillator, the tomographic reconstruction of a quantum harmonic oscillator is achieved with the same formulas: one only has to devise an experimental apparatus to collect the oscillator quadratures. The spin tomography, on the other hand, is used for the state reconstruction of quantum angular momentum (*i.e.* spin) state systems.

The third part of the thesis consists in the presentation and numerical simulation of various experiments based on the homodyne tomography technique. In particular, we presented a scheme for measuring the Hamiltonian operator (or the Liouvillian) of optical devices; a scheme for generating and detecting optical Schrödinger cats; a scheme to test the state reduction postulate and one for the test of Bell's inequalities; a feasibility study for an experiment that is presently being carried out concludes the thesis.

Is there still place for developments of the theoretical framework? Even though from the generality and self-consistence by now reached we are confident that a standing point has been reached, there are hints that suggest that a further generalization is possible. It might be possible, for example, to abandon the group theory formalism. In fact, the group theory is only used as a support for the theorem demonstrations, and, as the analysis of Weigert's state reconstruction method [29] lead to think, the requirement of having an irreducible unitary ray representation of a group to derive the tomographic quorum from, may be a too strong requirement. Presently, the research is directed towards the use of the imprimitivity systems in place of the group structure [26]. The imprimitivity systems may also lead to the tomographic state reconstruction of the relativistic particle, which has not been obtained up to now. Another generalization that needs further investigation is the extensions of the tomographic formulas to the case of discrete tomographic groups that are not subgroups of Lie groups.

Bibliography

[1] G. M. D'Ariano, C. Macchiavello and M. G. A. Paris, Phys. Rev. A **50**, 4298 (1994).

[2] G. M. D'Ariano, U. Leonhardt and H. Paul, Phys. Rev. A **52**, R1801 (1995).

[3] K. Vogel and H. Risken, Phys. Rev. A, **40**, 2847 (1989).

[4] G. M. D'Ariano, in "Quantum Communication, Computing, and Measurement", ed. by O. Hirota, A. S. Holevo and C. M. Caves, Plenum Publishing (New York and London 1997), p. 253.

[5] M. Paini, thesis (1999).

[6] G. M. D'Ariano, L. Maccone, and M. Paini, "Spin tomography", in progress.

[7] G. M. D'Ariano, "Universal Quantum Estimation", submitted to Phys. Rev. Lett.

[8] G. M. D'Ariano, Acta Phys. Slov. **49**, 513 (1999).

[9] G. M. D'Ariano and N. Sterpi, J. Mod. Opt. **44**, 2227 (1997).

[10] G. M. D'Ariano, M. G. A. Paris, Phys. Rev. A **60**, 518 (1999); G. M. D'Ariano, M. G. A. Paris, Acta Phys. Slov. **48**, 191 (1998); G. M. D'Ariano, M. G. A. Paris, Noise reduction in quantum tomography, submitted to J. Opt. B.

[11] G. M. D'Ariano, "Measuring quantum states", in *Quantum Optics and the Spectroscopy of Solids*, ed. by T. Hakioğlu and A.S. Shumovsky, Kluwer Academic Publishers (1997), p. 175.

[12] M. Freyberger, P. Bardroff, C. Leichtle, G. Schrade, and W. Schleich, Phys. World, **10/12**, 41 (1997).

[13] U. Fano, Rev. Mod. Phys. **29**, 74 (1957), Sec. 6.

[14] U. Leonhardt, H. Paul and G. M. D'Ariano, Phys. Rev. A **52**, 4899 (1995).

[15] U. Leonhardt, Phys. Rev. Lett., **74**, 4101 (1995).

[16] D. T. Smithey, M. Beck, M. G. Raymer, and A. Faridani, Phys. Rev. Lett. **70**, 1244 (1993); M. G. Raymer, M. Beck, and D. F. McAlister, Phys. Rev. Lett. **72**,1137 (1994); D. T. Smithey, M. Beck, J. Cooper, and M. G. Raymer, Phys. Rev. A, **48**, 3159 (1993).

[17] H. P. Yuen and J. H. Shapiro, IEEE Trans. Inf. Theory **IT-26**, 78 (1980); H. P. Yuen and V. W. S. Chan, Opt. Lett. **8**, 177 (1983).

[18] T. J. Dunn, I. A. Walmsley, and S. Mukamel, Phys. Rev. Lett. **74**, 884, (1995)

[19] T. Opatrný and D. - G. Welsch, Phys. Rev. A **55**, 1462 (1997).

[20] D. Leibfried, D. M. Meekhof, B. E. King, C. Monroe, W. M. Itano, and D. J. Weinland, Phys. Rev. Lett. **77**, 4281 (1996).

[21] G. Breitenbach, S. Schiller and J. Mlynek, Nature **387**, 471 (1997); S. Schiller, G. Breitenbach, S. F. Pereira, T. Müller, and J. Mlynek, Phys. Rev. Lett. **77**, 2933 (1996). **387**, 471 (1997)

[22] C. Kim and P. Kumar, Phys. Rev. Lett. **73**, 1605 (1994).

[23] G. M. D'Ariano, M. Vasilyev and P. Kumar, Phys. Rev. A **58**, (july 1998) in press.

[24] M. Munroe, D. Boggavarapu, M. E. Anderson, and M. G. Raymer, Phys. Rev. A **52**, R924 (1995).

[25] M. Vasilyev, S.-K. Choi, P. Kumar, and G. M. D'Ariano, (1999) submitted to PRL.

[26] G. Cassinelli, G. M. D'Ariano, and A. Levrero, unpublished.

[27] A. P. Balachandran and C. G. Trahern, *Lectures on group theory for physicists*, Bibliopolis (1984); A. O. Barut and R. Raczka, *Theory of group representations and applications*, World Scientific (1986); H. F. Jones, *Groups, representations and Physiscs*, Adam Hilger (1990), M. Hamermesh, *Group theory and its application to physical problems*, Addison-Wesley publishing co. (1962).

[28] A. O. Barut and R. Raczka, *Theory of group representations and applications*, World Scientific (1986), pg. 68, Eq. (11).

[29] J. P. Amiet and S. Weigert, J. Phys. A: Math. Gen. **32**, L269 (1999); J. P. Amiet and S. Weigert, e-print, quant-ph/9906099.

[30] A. Rotondi, "Probabilità, statistica e analisi dei dati", (1995) unpublished.

[31] A. Rotondi, private communication.

[32] G. M. D'Ariano, in *Quantum Communication, Computing and Measurement II*, P. Kumar, G. M. D'Ariano, and O. Hirota, eds. (Plenum Publishing, New York, 1999), to appear.

[33] G. M. D'Ariano, L. Maccone, M. G. A. Paris and M. F. Sacchi: "State preparation by photon filtering", Fortsch. der Physik, (1999), in press.

[34] G. M. D'Ariano, L. Maccone, M. G. A. Paris and M. F. Sacchi, Acta Phys. Slov. **49**, 659 (1999).

[35] G. M. D'Ariano, L. Maccone, M. G. A. Paris, and M. F. Sacchi, "Optical Fock-state synthetizer" (1999), submitted to Phys. Rev. Lett.

[36] G. M. D'Ariano, L. Maccone, M. G. A. Paris and M. F. Sacchi: "State measurement by photon filtering in a chain of Kerr ring cavities", 1999, submitted to Phys. Lett. A.

[37] G.M. D'Ariano, "Quantum estimation theory and optical detection", in *Quantum Optics and the Spectroscopy of Solids*, ed. by T. Hakioğlu and A.S. Shumovsky, Kluwer Academic Publishers (1997), p. 139.

[38] L. Mandel, Proc. Phys. Soc. **72**,1037 (1958); *ibid.* **74**, 233 (1959); P. L. Kelley and W. H. Kleiner, Phys. Rev. A **30**, 844 (1964).

[39] E. Wigner, "Group theory and its application to the quantum mechanics of atomic spectra", Academic press (1959), formula (15.27), pg. 167.

[40] M. Paini, in progress.

[41] M. Hamermesh, Group theory, Addison-Welsey (1962) chap. 7.

[42] A. Messiah, Quantum Mechanics, North Holland (1961), App. D.

[43] H. P. Yuen and M. Ozawa, Phys. Rev. Lett. **70**, 363 (1993).

[44] I. L. Chuang and Y. Yamamoto, Phys. Rev. A **52**, 3489 (1995).

[45] G. M. D'Ariano, C. Macchiavello, and L. Maccone, "Optical quantum gates", Fortsch. der Physik (1999), in press.

[46] G. M. D'Ariano, L. Maccone, Phys. Rev. Lett. **80**, 5465 (1998).

[47] H. Schmidt and A. Imamoglu, Opt. Lett. **21**, 1936 (1996); H. Schmidt and A. Imamoglu, Opt. Lett. **23**, 1007 (1998).

[48] L. V. Hau, S. E. Harris, Z. Dutton, and C. H. Behroozi, Nature **397**, 594 (1999).

[49] M. Ley and R. Loudon, J. Mod. Opt. **34**, 227 (1987).

[50] O. Haderka, M. Hendrych, private communication.

[51] G. M. D'Ariano, C. Macchiavello, and L. Maccone, Phys. Rev. A **59** 1816 (1999).

[52] S. Song, C.M. Caves and B. Yurke, Phys. Rev. A **41**, R5261 (1990).

[53] G. M. D'Ariano, P. Kumar, C. Macchiavello, L. Maccone, and N. Sterpi, Phys. Rev. Lett **83**, 2490 (1999).

[54] G. M. D'Ariano, A. Garuccio, L. Maccone, and M. F. Sacchi, J. Opt. B, **1**, 576 (1999).

[55] G. M. D'Ariano and L. Maccone, "Quantum Tomography of Optical Devices", in *5th International Conference on Squeezed States and Uncertainty Relations*, ed. by J. Janszky, Y. S. Kim, and V. I. Man'ko, p. 529 (1997).

[56] G. M. D'Ariano and L. Maccone, Fortschr. Phys. **46**, 6 (1998).

[57] J. F. Poyatos, J. I. Cirac, and P. Zoller, Phys. Rev. Lett. **78** 390 (1997); I. L. Chuang and M. A. Nielsen, J. Mod. Opt. **44** 2455 (1997).

[58] L. Dieci, B. Morini, A. Papini, Siam J. Matrix Anal. Appl. Vol. 17 **3**, 570 (1996); L. Dieci, B. Morini, A. Papini, A. Pasquali, submitted to Applied Numerical Mathematics.

[59] A. Papini, private communication.

[60] R. Dum, P. Zoller and H. Ritsch, Phys. Rev. A **45**, 4879 (1992).

[61] L. Maccone, thesis (1996).

[62] G. M. D'Ariano, C. Macchiavello, L. Maccone, Int. J. Mod. Phys. B **11**, 3385 (1997)

[63] L. A. Lugiato, F. Casagrande and L. Pizzuto, Phys. Rev. A **26** 3438 (1982).

[64] Fritz Haake, Maciej Lewenstein, Phys. Rev. A **27** 1013 (1983)

[65] C. Ginzel, M. J. Brigel, U. Martini, B. G. Englert, A. Schenzle, Phys. Rev. A **48**, 732 (1993).

[66] M. Brune *et al.*, Phys. Rev. Lett. **77**, 4887 (1996); J.M. Raimond, M. Brune and S. Haroche, Phys. Rev. Lett. **79**, 1964 (1997).

[67] B. Yurke, W. Schleich and D.F. Walls, Phys. Rev. A **42**, 1703 (1990); D.-G. Welsch, M. Dakna, L. Knoll and T. Opatrný, e-print quant-ph/9708018.

[68] A. La Porta, R.E. Slusher and B. Yurke, Phys. Rev. Lett. **62**, 28 (1989).

[69] T. Kiss, U. Herzog, and U. Leonhardt, Phys. Rev. A **52**, 2433 (1995).

[70] G.M. D'Ariano and C. Macchiavello, Phys. Rev. A **57**, 3131 (1998).

[71] T. F. Arecchi, private communication.

[72] G. M. D'Ariano, C. Macchiavello and N. Sterpi, Quant. Semicl. Opt. **9**, 929 (1997).

[73] A. Montina and T. F. Arecchi, Phys. Rev. A, **58**, 3472 (1998).

[74] J. von Neumann, "Mathematical Foundations of Quantum Mechanics", Princeton University Press, Princeton, N.Y. (1955).

[75] G. Lüders, Ann. Physik **8**, 322 (1951).

[76] See, for example: E. P. Wigner, Am. J. Phys. **31**, 6 (1963); M. Ozawa, preprint Quant-Ph/9802022/; N. Imoto, M. Ueda, and T. Ogawa, Phys. Rev. A **41**, 4127 (1990).

[77] M. Ozawa, private communication.

[78] See M. Ozawa, Ann. Phys. **259**, 121 (1997), and references therein.

[79] E. Arthurs and J. L. Kelly, Jr., Bell System Tech. J. **44** 725 (1965).

[80] O. Aytür and P. Kumar, Phys. Rev. Lett. **65**, 1551 (1990).

[81] C. Kim and P. Kumar, Phys. Rev. Lett. **73** 1605 (1994).

[82] M. Vasilyev, S.-K. Choi, P. Kumar, and G. M. D'Ariano, in *Quantum Communication, Computing and Measurement II*, P. Kumar, G. M. D'Ariano, and O. Hirota, eds. (Plenum Publishing, New York, 1999), to appear.

[83] G. M. D'Ariano, M. Vasilyev, and P. Kumar, Phys. Rev. A **58**, 636 (1998).

[84] O. Aytür and P. Kumar, Opt. Lett. **17**, 529 (1992).

[85] G. M. D'Ariano, L. Maccone, M. F. Sacchi and A. Garuccio: "Homodyning Bell's inequality", in '4th Int. Conf. on Quantum Communication, Measurement, and Computing, Plenum, 1998, in press.

[86] A. Einstein, B. Podolsky and N. Rosen, Phys. Rev. **47**, 777 (1935).

[87] N. Bohr, Phys. Rev. **48**, 696 (1935).

[88] J. S. Bell, Physics **1**, 195 (1964).

[89] J. F. Clauser, Phys. Rev. Lett. **36**, 1223 (1976); A. Aspect, J. Dalibard, and G. Roger, Phys. Rev. Lett. **47**, 460 (1981); A. J. Duncan, W. Perrie, H. J. Beyer and H. Kleinpoppen, in *Fundamental Processes in Atomic Collision Physics*, Plenum, New York, 1985, pg. 555; Z. Y. Ou and L. Mandel, Phys. Rev. Lett. **61**, 50 (1988); C. O. Alley and Y. H. Shih, Phys. Rev. Lett. **61**, 2921 (1988); J. D. Franson, Phys. Rev. Lett. **62**, 2200 (1989); K. Mattle, H. Weinfurter, P. G. Kwiat and A. Zeilinger, Phys. Rev. Lett. **76**, 4656 (1996).

[90] J. F. Clauser, M. A. Horne, A. Shimony, and R. A. Holt, Phys. Rev. Lett. **23**, 880 (1969); J. F. Clauser and M. A. Horne, Phys. Rev. D **10**, 256 (1974); A. Garuccio and V. A. Rapisarda, Nuov. Cim. A **65**, 269 (1981).

[91] L. De Caro and A. Garuccio, Phys.Rev. A **54**, 174 (1996).

[92] L. Mandel, E. Wolf, *Optical coherence and quantum optics*, Cambridge Univ. Press (1995), pg. 649.

[93] G. M. D'Ariano, F. De Martini, G. Di Giuseppe, C. Macchiavello, and L. Maccone, "Quantum tomography of Fock states", unpublished.